

LASER-INDUCED ALIGNMENT AND ORIENTATION:
Photoelectron Angular Distributions from Strong Field
Ionization

PhD Thesis

LOTTE HOLMEGAARD



Department of Chemistry
Aarhus University

March 2010

PREFACE

This thesis has been submitted to the Faculty of Science at Aarhus University, in order to fulfil the requirements for obtaining the PhD degree. The work presented has been carried out at the Department of Chemistry in the years 2007-2010 under the supervision of Prof. Henrik Stapelfeldt.

Acknowledgements

First and foremost, I would like to thank Henrik Stapelfeldt. Henrik is a fantastic supervisor, always encouraging and with an infectious dedication to research.

During my time in the "Femtolab" I have had the pleasure of working with a series of inspiring and talented people. In order of appearance I would like to thank Christer Z. Bisgaard, Simon S. Viftrup and Vinod Kummerappan, who early in my studies played important roles in introducing me to the laboratory, Jens H. Nielsen, Jonas L. Hansen, Iftach Nevo, Jochen Maurer, Line Kalhøj, Sofie L. Kragh, who joined the group. With these people I have spend many hours in the basement and enjoyed scientific and non-scientific discussions during coffee breaks or late nights of data acquisition. I would also like to thank the remaining former and present members of the "Femtolab" for joyful hours at Christmas lunches and canoe trips.

A special thanks goes to Jan Thøgersen. Every laboratory should be so fortunate as to have a "Jan" around to tweak the lasers and answer any question that may arise.

During my time as a PhD student I have also benefitted greatly from the collaboration with the theoretical group of Lars Bojer Madsen from the Lundbeck Foundation Theoretical Center for Quantum System Research, Department

of Physics and Astronomy, Aarhus University. All the calculations involving strong field ionization described in this thesis have been performed by Lars and "his boys". I would like to thank Lars, Thomas, Christian, Christian, Mahmoud and Darko for fruitful discussions and for enhancing my insight into strong field physics.

During the last 2 years I have been so fortunate to be a part of yet another fruitful collaboration and I would like to thank Frank Filsinger, Jochen Küpper and Gerard Meijer from the Fritz-Haber-Institut der Max-Planck-Gesellschaft in Berlin, for joyful hours in the lab and for introduced us to manipulation of molecules with static electric fields.

Finally, I would like to thank my boyfriend, friends and family for support and encouragement during these last 3 years and for providing me with the necessary space to concentrate on research.

Lotte Holmegaard
March 2010

Outline of the Thesis

When I first joined the Femtolab more than 6 years ago the main focus was on establishing and characterizing laser-induced alignment in the adiabatic as well as the nonadiabatic regime, since then the focus has shifted towards applications of aligned and even oriented molecules and laser induced alignment and orientation, although interesting on its own, is being viewed more and more as a tool in further applications.

For that reason this thesis is divided into two parts. In the first part (Chapter 1-7) laser-induced alignment and mixed-field orientation of quantum-state-selected molecules is discussed. In the second part (Chapter 8-12) strongly aligned and oriented molecules are used as targets in molecular frame photoelectron angular distribution experiments from strong field ionization.

Chapter 1 A historically inspired introduction to, and motivation for, controlling the spatial orientation of molecules, is provided.

Chapter 2 In this chapter the main concepts and theory behind laser induced alignment and mixed field orientation is introduced.

Chapter 3 The experimental setup including the optical, vacuum and detection system is described in details.

Chapter 4 It is demonstrated how the inhomogeneous field of an electrostatic beam deflector can be used to select the lowest lying rotational quantum states of a molecule.

Chapter 5 It is shown how laser induced 1-dimensional alignment and mixed-field orientation is strongly enhanced using quantum-state-selected molecules as targets. Alignment and orientation is induced in the adiabatic regime using the combined action of a 10 nanosecond long laser pulse and a weak static electric field. Unprecedented degrees of alignment and strong orientation is achieved.

Chapter 6 The experiments from Chapter 5 are extended and full 3-dimensional alignment and mixed-field orientation is demonstrated.

Chapter 7 Nonadiabatic alignment is briefly discussed and demonstrated for linear molecules.

Chapter 8 An introduction to molecular frame photoelectron angular distributions is provided. Traditional photoelectron spectroscopy is discussed and extended to the strong field regime. The main concepts of strong field ionization are outlined.

- Chapter 9** The first experimental evidence of the photoelectron angular distributions from multiphoton ionization on the molecular alignment of a linear molecule is demonstrated.
- Chapter 10** Photoelectron angular distributions from strong field ionization of 1-dimensionally oriented molecules are measured and pronounced anisotropies are observed that are absent when the measurements are conducted on randomly oriented molecules.
- Chapter 11** Photoelectron angular distributions from strong field ionization of 3-dimensionally oriented molecules are demonstrated. Striking structures appear due to the suppression of electron emission in nodal planes of the fixed electronic orbitals.
- Chapter 12** The angular dependence of the ionization yield on molecular alignment is measured.
- Chapter 13** This final chapter concludes the experimental findings and methods described in this thesis. Future perspectives are outlined, including conformer selection and applications of aligned and oriented molecules.

List of Publications

The work presented in this thesis has lead to the following publications:

- I *Photoelectron angular distributions from strong-field ionization of oriented molecules*
L. Holmegaard, J. L. Hansen, L. Kalhøj, S. L. Kragh, H. Stapelfeldt, F. Filsinger, J. Küpper, G. Meijer, D. Dimitrovski, M Abu-samba, C. P. J. Martiny and L. B. Madsen, accepted for publication in *Nature Physics* (2010)
- II *Laser-induced 3D alignment and orientation of quantum-state-selected molecules*
I. Nevo, L. Holmegaard, J. H. Nielsen, J. L. Hansen, H. Stapelfeldt, F. Filsinger, G. Meijer, and J. Küpper, *Physical Chemistry, Chemical Physics*, **11**, 9912 (2009)
- III *Pure Samples of Individual Conformers: The Separation of Stereoisomers of Complex Molecules Using Electric Fields*
F. Filsinger, J. Küpper, G. Meijer, J. L. Hansen, J. Maurer, J. H. Nielsen, L. Holmegaard, and H. Stapelfeldt, *Angewandte Chemie International Edition*, **48**, 6900 (2009). Selected as VIP (Very Important Paper)
- IV *Quantum-state selection, alignment, and orientation of large molecules using static electric and laser fields*
F. Filsinger, J. Küpper, G. Meijer, L. Holmegaard, J. H. Nielsen, I. Nevo, J. L. Hansen, and H. Stapelfeldt, *The Journal of Chemical Physics*, **131**, 064309 (2009)
- V *Laser-Induced Alignment and Orientation of Quantum-State-Selected Large Molecules*
L. Holmegaard, J. H. Nielsen, I. Nevo, H. Stapelfeldt, F. Filsinger, J. Küpper, and G. Meijer, *Physical Review Letters*, **102**, 023001 (2009)
- VI *Multiphoton electron angular distributions from laser-aligned CS₂ molecules*
V. Kumarappan, L. Holmegaard, C. Martiny, C. B. Madsen, T. K. Kjeldsen, S. S. Viftrup, L. B. Madsen and H. Stapelfeldt, *Physical Review Letters*, **100**, 093006 (2008)

In addition the author participated in the following work:

- VII *Controlling the rotation of asymmetric top molecules by the combination of a long and a short laser pulse*
S. S. Viftrup, V. Kumarappan, L. Holmegaard, C. Z. Bisgaard, H. Stapelfeldt, M. Artamonov, E. Hamilton, and T. Seideman, *Physical Review A*, **79**, 023404 (2009)

- VIII *A combined experimental and theoretical study on realizing and using laser controlled torsion of molecules*
C. B. Madsen, L. B. Madsen, S. S. Viftrup, M. P. Johansson, T. B. Poulsen, L. Holmegaard, V. Kumarappan, K. A. Jørgensen and H. Stapelfeldt, *Journal of Chemical Physics*, **130**, 234310 (2009).
- IX *Manipulating the Torsion of Molecules by Strong Laser Pulses*
C. B. Madsen, L. B. Madsen, S. S. Viftrup, M. P. Johansson, T. B. Poulsen, L. Holmegaard, V. Kumarappan, K. A. Jørgensen and H. Stapelfeldt, *Physical Review Letters*, **102**, 073007 (2009)
- X *Aligning molecules with long or short laser pulses*
V. Kumarappan, S. Viftrup, L. Holmegaard, C. Z. Bisgaard, and H. Stapelfeldt, *Physica Scripta*, **76**, C63-C68 (2007)
- XI *Control of rotational wave-packet dynamics in asymmetric top molecules*
L. Holmegaard, S. S. Viftrup, V. Kumarappan, C. Z. Bisgaard, H. Stapelfeldt, E. Hamilton, and T. Seideman, *Physical Review A. Atomic, Molecular, and Optical Physics*, **75**, 051403(R) (2007)
- XII *Role of rotational temperature in adiabatic molecular alignment*
V. Kumarappan, C. Z. Bisgaard, S. S. Viftrup, L. Holmegaard, and H. Stapelfeldt, *Journal of Chemical Physics*, **125**, 194309 (2006)
- XIII *Characterization of ultraviolet femtosecond pulse propagation in aluminum-coated capillary fibers*
J. Thøgersen, E. S. Y. Madsen, L. Holmegaard, S. K. Jensen, S. R. Keiding, Y. Matsuura and M. Miyagi, *Journal of Applied Physics*, **98**, 033519 (2005)

CONTENTS

Preface	i
Acknowledgements	i
Outline	iii
List of Publications	v
I ALIGNMENT AND ORIENTATION OF QUANTUM-STATE-SELECTED MOLECULES	1
1 Introduction to Alignment and Orientation	3
2 Molecules in Static Electric and Laser Fields	9
2.1 Introduction	9
2.2 Adiabatic Alignment	12
2.3 Mixed-Field Orientation	14
2.4 Nonadiabatic Alignment	16
2.4.1 δ -Kick Model	16
2.4.2 Quantum Mechanical Description	17
2.4.3 Measuring the Degree of Alignment	18
3 Experimental Setup	19
3.1 The Optical Setup	20
3.1.1 Alignment Pulses	22
3.1.2 Probe Pulses	24
3.1.3 Combining and Characterizing the Beams	26

3.2	Vacuum and Detection System	28
3.2.1	The Molecular Beam	29
3.2.2	Electrostatic Beam Deflection	30
3.2.3	The Velocity Map Imaging Spectrometer	31
3.2.4	The Detection System	32
3.2.5	Data Acquisition and Processing	33
3.2.6	Timing	34
4	Electrostatic Deflection of Cold Molecular Beams	35
4.1	Introduction	35
4.2	Experimental	37
4.3	Results and Discussion	38
5	Laser Induced 1D Alignment and Orientation	47
5.1	Introduction	47
5.2	Experimental Setup	48
5.3	Laser-Induced Alignment and Orientation of a Linear Molecules .	49
5.3.1	Deflection of the Molecular Beam	49
5.3.2	Laser-Induced Alignment	49
5.3.3	Mixed-Field Orientation	53
5.4	Laser-Induced Alignment and Orientation of Asymmetric Top Molecules	59
5.4.1	Laser-Induced Alignment	59
5.4.2	Mixed-Field Orientation	62
6	Laser Induced 3D Alignment and Orientation	69
6.1	Introduction	69
6.2	Experimental Setup	70
6.3	Results and Discussion	71
6.3.1	Molecular Beam Deflection	71
6.3.2	1D and 3D Alignment	71
6.3.3	1D and 3D Orientation	81
7	Nonadiabatic Alignment	83
7.1	Introduction	83
7.2	Experimental Setup	84
7.3	Results and Discussion	84
7.3.1	Nonadiabatic Alignment of Carbondisulfide	84
7.3.2	Nonadiabatic Alignment of Carbonylsulfide	87

II PHOTOELECTRON ANGULAR DISTRIBUTIONS FROM ALIGNED AND ORIENTED MOLECULES	89
8 Introduction to Photoelectron Angular Distributions	91
8.1 Traditional Photoelectron Spectroscopy	92
8.2 The Strong Field Approach	95
8.2.1 Ionization	96
8.2.2 Propagation in the Field	98
8.2.3 Rescattering	99
9 Multiphoton Ionization of Laser-Aligned Carbonylsulfide Molecules	101
10 MFPADs from Tunnel Ionization of Carbonylsulfide	111
10.1 Circular Polarized Probe Beam	111
10.1.1 Ionization	116
10.1.2 Propagation in the Field	117
10.2 Linearly Polarized Probe Beam	120
10.2.1 'Simple Woman's Model'	124
10.2.2 Symmetry Considerations	127
11 MFPADs from Tunnel Ionization of Benzonitrile	131
11.1 Symmetry Considerations	135
11.2 Tunnel Model	137
12 Angle Dependent Strong Field Ionization Yields	141
12.1 Introduction	141
12.2 Results and Discussion	142
13 Conclusions and Outlook	147
13.1 Cleaning the Molecular Sample	148
13.1.1 Conformer Selection	148
13.1.2 Isolating Molecules from the Carrier Gas	150
13.2 Alingment and Orientation	151
13.2.1 Nonadiabatic Alignment and Orientation	151
13.2.2 Brute-Force Orientation	152
13.3 Applications of Strongly Aligned or Oriented Molecules	152
13.3.1 Manipulating the Torsion of Molecules	153
14 Summary	157
A The influence of the capacitor plates	161
References	165

Part I

ALIGNMENT AND ORIENTATION OF QUANTUM-STATE-SELECTED MOLECULES

1

INTRODUCTION TO ALIGNMENT AND ORIENTATION

The spatial orientation of a molecule is of crucial importance for its interactions with other molecules, atoms or electromagnetic fields. Motivations for confining molecules in space can be found in many areas of chemistry and physics, ranging from the possibility of studying or controlling a chemical reaction to imaging of a molecular orbital. All with the common denominator that the experimental outcome strongly depends on the orientation of the molecule. In the following a brief introduction to the concepts and development of laser-induced alignment and orientation is provided.

In the gas phase molecules are randomly oriented and rotate unhindered (Fig. 1.1 a)). If a single axis of the molecule is confined with respect to a space-fixed axis the molecule is said to be 1-dimensionally (1D) aligned (Fig. 1.1 b)). For asymmetric top molecules complete rotational confinement requires that all three axes of the molecule are fixed to space-fixed axes, this is termed 3-dimensional (3D) alignment (Fig. 1.1 c)).

An ensemble of gas phase molecules has inversion symmetry even when 3D aligned. If, in addition to 1D or 3D alignment, the molecules have a preferred direction with respect to the space fixed axes, i. e. if the inversion symmetry is broken, they are said to be 1D or 3D oriented (Fig. 1.1 d) and e), respectively).

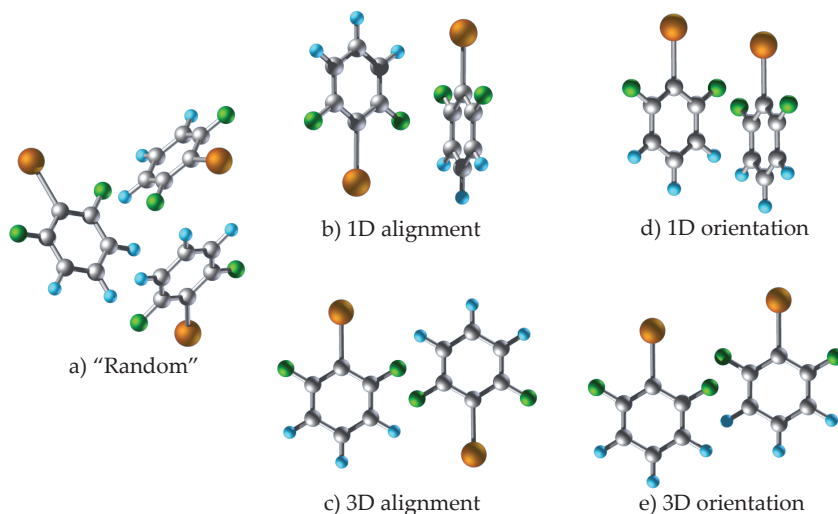


Figure 1.1: Definitions of the different regimes of molecular alignment and orientation. See text for details.

Most gas phase experiments are done under conditions where the molecules are randomly oriented. Orientational averaging then becomes an unavoidable experimental fact of life obscuring measurements of molecular properties and leading to blurring and potential loss of information.

Recently, Albert Stolow provided a very illustrative analogy by referring to the ancient Indian tale of six blind men encountering an elephant [1]. In the tale each man approaches the elephant from different directions and naturally their perception of the elephant strongly disagrees. One finds the squirming trunk, another the swinging tail, a third a leg and so on, they conclude that the elephant is a snake, a rope, a tree and so on. The morale of the story is that reality may be viewed differently depending upon ones perspective or angle of approach. There is a lot of wisdom to be found in this tale, however without dwelling I will restrict myself to say that the same is true for molecules. Molecular properties and dynamics differ depending on from where they are viewed or probed.

The phenomenon is well known in X-ray diffraction of crystals. Similar to gas phase measurements in the molecular versus the laboratory frame is the difference between single-crystal and the random orientation of crystallites in powder X-ray diffraction with the former revealing the greatest details of molecular structure and information.

The desire to control molecular orientation has roots that go fare back in his-

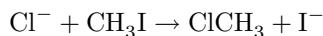


Figure 1.2: There are many versions of the ancient Indian tale. In this Japanese ukiyo-e print by Hanabusa Itchō it is blind monks that investigate the elephant. Each monk experiences something different depending on his angle of approach, and a clear analogy can be made to how measurements of molecular properties depend on the direction from which the molecules are viewed or probed.

tory. More than 30 years ago linear dichroism spectroscopy experiments were performed on aligned samples of molecules [2]. Linear dichroism spectroscopy is the measurement of the difference in absorption of linearly polarized light parallel and perpendicular to an aligned molecule. Molecular orientation, probed by linear dichroism, was obtained using different techniques. One approach was based on stretched polymer films. Adding small molecules to a polymer film either before or after the film is stretched mechanically, causes the absorbed molecules to align their longest axis preferentially along the direction of the stretch. Another technique, called flow orientation, was used to align DNA or long polymers, where the orientation is caused by the viscous drag when the solution is flowed between narrow walls. A common feature for these methods is that they all depended on some kind of external field or intermolecular force present during the experiment.

Historically one of the main motivations for confining molecules in space in the gas phase was investigation of steric effects in bimolecular reactions and the control of the rate of a chemical reaction for different collision geometries. A

classical example is the anion - molecule nucleophilic substitution (S_N2 type) reaction, such as the substitution of iodine with chlorine in methyl iodide:



The reaction rate of this reaction depends strongly on the orientation of methyl iodide relative to the attacking chlorine ion. The probability for the reaction to occur is significantly higher when the chlorine ion attacks methyl iodide along the C-I bond from the methyl end.

The first attempts to control molecular orientation in the 1960's utilized electrostatic fields. Polar molecules were rotationally state-selected and oriented by the electrostatic hexapole technique via the first-order Stark effect, using moderate field strengths [3, 4]. The beauty of the technique is that it allows selection of a single rotational quantum state. The drawback, however, is that it applies to a limited range of species. Suitable molecules are symmetric tops, asymmetric tops with a dipole moment along the A or C axis, linear polyatomic molecules excited in bending vibrations, and diatomics with electronic angular momentum. Molecules selected in a single rotational state, with their angular momentum precessing around the external field are per definition oriented, however the confinement is modest and limited by the selected state.

In the early 90's an alternative approach nicknamed 'Brute-force orientation' was proposed individually by Loesch and Remscheid [5] and later by Friedrich and Herschbach [6]. In this approach a strong homogeneous electrostatic field was applied to create directional hybrids of the field-free rotational states via the second- and higher- order Stark effect. If the interaction energy of the molecule with the field exceeds the rotational energy the molecules will orient. This technique extended the class of oriented molecules beyond those accessible via the hexapole state selection. The requirements for this approach is strongly rotationally cooled molecules with large dipole moments and very strong dc fields.

In parallel, it was realized that the strong electric fields of a focussed non-resonant laser pulse could be used to align molecules much more efficiently than static fields. A rigorous theoretical framework for using infrared non-resonant laser pulses to induce dynamical alignment was developed independently by Friedrich and Herschbach [7] and Seideman [8] in the mid nineties.

Historically, as early as 1976 Zon and Katsnel'son presented a theoretical treatment of a symmetric top molecule in an intense, nonresonant laser field [9]. They presented an analytical solution to the time independent Schrödinger equation, and the effect on the rotational spectrum. However, the implication that this could lead to spatial orientation of the molecules was only sparsely discussed.

The idea of using intense laser fields to induce molecular alignment was addressed in several gas phase studies from the late 80's and throughout the

90's [10, 11]. The speculations were based on observations of ionic fragments, resulting from breakup of laser produced multiple charged molecular ions, ejected with initial velocities primarily aligned along the laser polarization vector. Two possible explanations were offered for the observations, namely geometric alignment and dynamical alignment. In geometrical alignment the ensemble of molecules are not actively aligned, merely a subset of the randomly oriented molecules are selected due to a strong angular dependence on the ionization yield. More interesting is however the proposal of dynamical alignment where, in contrast, alignment is achieved through the interaction of an induced dipole moment and the laser field exerting a torque on the molecules. Later it became clear that the anisotropy in the angular distributions cannot unambiguously be explained by molecular alignment and the strong angular dependence of enhanced multiple ionization [12, 13] has played an important role in the studies.

From the mid nineties the field has developed rapidly. It was realized that the pulse duration of the laser field applied to induce alignment plays a significant role in the alignment dynamics [7, 8]. In the adiabatic regime long pulses compared to the inherent rotational period of the molecules are applied. Molecules are aligned with the laser field present and return to field-free rotor states when the pulse is over again. The first experimental demonstration of adiabatic alignment came from Kim and Felker [14] and was followed by studies by Stapelfeldt and coworkers [15, 16]. The adiabatic regime demonstrated high degrees of alignment.

An especially advantageous feature of laser induced alignment is the possibility of producing aligned molecules under field-free conditions. It was proposed that employing short nonadiabatic laser pulses [8], again short with respect to the rotational period of the molecule, a rotational wave packet would be formed, resulting in time-dependent alignment. The first experimental evidence of transient alignment was demonstrated by Rosca-Pruna and Vrakking [17]. The adiabatic and non-adiabatic regime will be treated in greater details in Chapter 2.

In contrast to the static field techniques laser induced alignment is generally applicable to any molecule, only requiring an anisotropic polarizability tensor. The drawback, however, is that the head versus tail resolution achieved in orientation is lost due to the oscillatory nature of the non-resonant near-infrared laser field.

As molecular alignment became well established both theoretically and experimentally, including 3-dimensional alignment [18–23], attention expanded towards realizing sharp alignment and orientation simultaneously. Friedrich and Herschbach suggested in 1999 to exploit the combined action of a static electric or magnetic field and a laser field to induce molecular orientation through a

pseudo first order Stark effect [24, 25]. In the adiabatic regime this was demonstrated by Sakai and coworkers [26, 27] and Buck *et al.* [28]. Even in the non-adiabatic limit orientation due to the electrostatic field alone can be enhanced by a combined action with a nonresonant laser field [29]. Laser field-free molecular orientation has been demonstrated by Sakai and co-workers using a combination of a dc electric field and a laser pulse with adiabatic turn-on and non-adiabatic turn-off (often referred to as switched laser field) to induce dynamic orientation in OCS molecules [30]. Vrakking and coworkers selected NO molecules in a single quantum state using a hexapole state selector [31] and, subsequently, a combination of a static and femtosecond laser field to induce molecular orientation [32, 33]. A route to both laser and static electric field-free orientation was first suggested by Kanai and Sakai [34], further elaborated in [35] and, recently, Matthias Kling and co-workers reported the first experimental observation of non-adiabatic field-free orientation of a heteronuclear diatomic molecule (CO) induced by an intense two-color (800 and 400 nm) femtosecond laser field [36]. The method relies on an all optical approach and alignment and orientation is induced through the interaction with the polarizability and hyperpolarizability of the molecule. In this way orientation, although very weak, is obtained under completely field-free conditions.

Over the past decade molecular alignment and orientation has grown into an active research area with a broad variety of demonstrated and projected applications in molecular science. It has sparked the emergence of new techniques that in turn have put even higher demands on molecular orientation techniques. Among the applications are areas such as ultrafast optics [37], tomographic reconstruction of molecular orbitals [38], photoelectron angular distributions from fixed-in-space molecules [39–41], high-order harmonic generation [42–45], molecular dynamics, and solution chemistry [46] and new applications such as diffractive imaging at emerging X-ray free-electron lasers such as LCLS at Stanford or XFEL at Hamburg [47–51].

Any application of aligned or oriented molecules will benefit significantly from or simply require a strong degree of orientation. In the recent developments of laser induced alignment and orientation much effort has been made in the direction of field-free alignment and orientation, however, thus far often at the cost of a significant loss in the degree of orientation. In the following chapters it will be demonstrated how unprecedented degrees of alignment and orientation can be obtained from molecules selected in the lowest rotational quantum states after spatially separation in an electrostatic beam deflector.

MOLECULES IN STATIC ELECTRIC AND LASER FIELDS

2.1 Introduction

In this chapter the main concepts and theory behind laser induced alignment [52, 53] and mixed field orientation [24, 25] will be introduced.

Let us first consider the interaction between a molecule and a strong electromagnetic laser field, described by

$$\mathbf{E}(t) = \varepsilon(t) \cos(\omega t) \quad (2.1)$$

where $\varepsilon(t) = E_0 \varepsilon(t) \hat{\mathbf{e}}$, E_0 is the field strength, $\varepsilon(t)$ is the pulse envelope, $\hat{\mathbf{e}}$ is the unit vector in the field polarization direction and ω is the central frequency.

The interaction is well described within the dipole approximation as

$$V_{\text{int}}(t) = -\boldsymbol{\mu} \cdot \mathbf{E}(t) \quad (2.2)$$

where $\boldsymbol{\mu}$ is the electric dipole moment operator of the system, $\boldsymbol{\mu} = e \sum_j \mathbf{r}_j$, where e is the electron charge and \mathbf{r}_j denotes the coordinates of electron j .

In the quantum mechanical approach the wave packet describing the initial state of the molecular ensemble is formally expanded in a complete set of rovibronic eigenstates

$$|\psi(t)\rangle = \sum_{\mathbf{n}} c_{\mathbf{n}}(t) e^{-iE_{\mathbf{n}}t/\hbar} |\mathbf{n}\rangle. \quad (2.3)$$

The rotational dynamics of a molecule during and following the interaction with a laser pulse is evaluated by solving the time-dependent Schrodinger equation

$$i\hbar \frac{\partial}{\partial t} |\psi(t)\rangle = \hat{H} |\psi(t)\rangle, \quad (2.4)$$

Exploiting the orthonormality of the expansion basis set, $\langle \mathbf{m} | \mathbf{n} \rangle = \delta_{\mathbf{m}\mathbf{n}}$ and projecting onto a specific eigenstate $|\mathbf{m}\rangle$ leads to a set of coupled, linear, first order differential equations

$$i\hbar \frac{\partial}{\partial t} c_{\mathbf{n}}(t) = \sum_{\mathbf{n}} c_{\mathbf{n}}(t) e^{-iE_{\mathbf{n}}t/\hbar} V_{nm}(t) \quad (2.5)$$

where $E_{nm} = E_m - E_n$, $V_{nm}(t) = \langle \mathbf{m} | V_{\text{ind}}(t) | \mathbf{n} \rangle$

The effective perturbation can be expanded in a Taylor series

$$V_{nm}(t) = -\boldsymbol{\mu}_{nm} \cdot \mathbf{E}(t) - \frac{1}{2} \mathbf{E}^*(t) \boldsymbol{\alpha}_{nm} \mathbf{E}(t) - \dots, \quad (2.6)$$

The interaction is sometimes referred to as the non-resonant dynamic Stark effect (NRDSE) and the coupling of field-free states via NRDSE can be divided into two regimes [54, 55]. When the field frequency is turned near an electronic resonance the dipole coupling of neighboring eigenstates dominates and the coherent superposition in the field attempts to oscillate at the frequency of the laser pulse. In the other limit neighboring states are coupled through electronic states far off resonance (non-essential states). These states have negligible population and do not participate in the dynamics directly. They mediate the dynamics by Raman coupling the populated states in the presence of the non-resonant laser field.

In the following we will only consider a non-resonant (implying far off resonance) non-ionizing laser pulse, i. e. far detuned from vibronic and electronic transition frequencies. Considering only the ground state dynamics α can to a good approximation be described by the usual static polarizability. In the laboratory frame the interaction potential can now be expressed in terms of the pulse envelopes. Recalling that the electric field oscillates many times within the pulse envelope allows us to reduce the expression in Eq. (2.6) as the term $\cos(\omega t)$ averages to 1/2 over an optical period and the induced potential reduces to

$$V_{\text{ind}}(t) = -\frac{1}{4} \sum_{i,j} \varepsilon_i^*(t) \alpha_{ij} \varepsilon_j(t), \quad (2.7)$$

where $i, j = X, Y, Z$ are the space-fixed coordinates and $\alpha_{i,j}$ is the polarizability tensor component.

Next we consider a polar molecule subjected to a dc electric field. The interaction potential of the permanent dipole moment with the static electric field can be described by

$$V_{\text{stat}} = -\boldsymbol{\mu}_0 \cdot \mathbf{E}_{\text{stat}} \quad (2.8)$$

where $\boldsymbol{\mu}_0$ is the permanent dipole moment.

The total Hamiltonian for a molecule subjected to a static electric and non-resonant laser field now becomes

$$\hat{H} = \hat{H}_0 + V_{\text{eff}} \quad (2.9)$$

where \hat{H}_0 is the field-free hamiltonian and $V_{\text{eff}} = V_{\text{ind}} + V_{\text{stat}}$. Within the rigid-rotor approximation \hat{H}_0 reduces to the rotational Hamiltonian

$$\hat{H}_{\text{rot}} = \frac{\hat{J}_x^2}{2I_{xx}} + \frac{\hat{J}_y^2}{2I_{yy}} + \frac{\hat{J}_z^2}{2I_{zz}}, \quad (2.10)$$

where the operators \hat{J}_i with $i = x, y, z$ represent the total angular momentum of the molecule and I_{ii} are the corresponding principal moments of inertia with respect to the molecular frame.

It is clear that for a molecule with an anisotropic polarizability tensor the interaction between the molecule and the laser depends on the relative orientation between the molecule and the polarization of the laser prior to the interaction. The molecules will experience a net torque pulling the major axis of polarizability towards the polarization axis of the laser, i.e. the molecules will align in the most favorable geometry along the polarization of the laser. In addition, the asymmetric deformation of the interaction potential can lead to orientation of the permanent dipole moment of a polar molecule.

There are different ways of obtaining laser induced alignment and orientation. Using a laser pulse with a slowly evolving pulse envelope, slow in comparison with the rotational period of the molecule, will cause the molecule to follow the instantaneous intensity of the pulse and thus align slowly, reaching the most favorable orientation at the peak of the pulse. The molecule undergoes an adiabatic transition from a field-free state to a state described by both the field and the molecule.

If, on the other hand, a short laser pulse is used, again short compared to the rotational dynamics of the molecule, the molecule experiences a rotational kick in the direction of the polarization of the laser, making the molecules rotate. The interaction is said to be nonadiabatic. From a quantum mechanical point of view the interaction with the laser field creates a coherent superposition of eigenstates through a series of nonresonant Raman transitions, that is,

a rotational wave packet is created, that will de-phase and re-phase creating a time-dependent alignment long after the pulse has been switched off.

A detailed description of the different ways of obtaining alignment and orientation will be presented in the following sections.

2.2 Adiabatic Alignment

The early work on 'brute force orientation' in connection to reactive scattering experiments with molecular beams inspired Friedrich and Herschbach to propose the idea of exchanging the static field with the electric field of a non-resonant laser pulse, triggering the idea of laser induced adiabatic alignment [7, 56]. In the adiabatic limit the turn-on and turn-off times of the alignment pulse are slow compared to the rotational period of the molecule. Upon the slow turn-on of the alignment pulse the adiabatic theorem [57] states that each eigenstate of the field-free Hamiltonian will evolve adiabatically, being carried over to the corresponding eigenstate, called the pendular state, of the complete Hamiltonian representing both the field and the molecule as given in Eq. (2.9). As the laser field is slowly turned off again at the end of the pulse the system returns to the original isotropic field-free eigenstates and no alignment remains.

Quantum mechanical calculations solving the time dependent Schrödinger equation have been carried out on the dynamic alignment of molecules by varying the pulse evolution time [58, 59]. In this way the adiabatic limit was determined. At pulse durations only a few times the rotational period of the molecule, $\tau_{pulse} > T_{rot}$ the interaction was found to be truly adiabatic and pendular states faithfully followed the field.

In case of a linear molecule interacting with a linearly polarized laser field the induced interaction potential reduces to the expression

$$V_{ind}(t) = -\frac{E_0(t)^2}{4} (\Delta\alpha \cos^2 \theta + \alpha_{\perp}), \quad (2.11)$$

where the polarizability anisotropy, $\Delta\alpha = \alpha_{\parallel} - \alpha_{\perp}$, is the difference in polarizability parallel ($\alpha_{\parallel} = \alpha_{zz}$) and perpendicular ($\alpha_{\perp} = \alpha_{xx} = \alpha_{yy}$) to the internuclear axis. For $\alpha_{\parallel} > \alpha_{\perp}$ Eq. (2.12) creates a potential well, where the lowest energies are obtained for $\theta = 0$ and 180° . Since θ is the angle between the internuclear axis and the laboratory fixed axis in which the laser is polarized, it is favorable for the molecule to align its internuclear axis parallel to the polarization of the laser field. Hence, in the presence of the field the molecules librate around the polarization of the axis rather than rotate freely. Since the motion is much similar to an oscillating pendulum, the eigenstates in the presence of the field are termed pendular states. In Fig. 2.1 a, the effective interaction potential

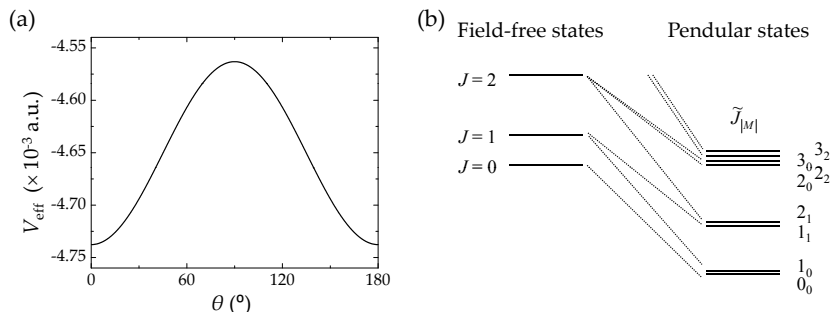


Figure 2.1: a) Effective induced potential for carbonylsulfide (OCS) at a laser intensity of $1 \times 10^{12} \text{ W/cm}^2$. b) Sketch of the lowest lying field-free and pendular states of a linear molecule.

has been plotted for carbonylsulfide (OCS) exposed to a linearly polarized laser field with an intensity of $I_0 = 1 \times 10^{12} \text{ W/cm}^2$.

In the case of a linear molecule only two quantum numbers are required to describe the field-free rotational motion; The angular momentum quantum number J and the magnetic quantum number M . In the case of a linearly polarized laser field the projection M of the angular momentum vector \mathbf{J} onto the laboratory fixed Z -axis is a conserved or "good" quantum number. The pendular states are thus labeled M and \tilde{J} corresponding to the J quantum number of the field-free rotor state that it adiabatically correlates to. A striking feature of adiabatic alignment is that the hybrid pendular states occur as pairs or tunneling doublets, due to the confinement in the double well potential. The spacing of the doublet states corresponds to the tunneling rate between the two parts of the well. In Fig. 2.1 b, the lowest lying field-free and pendular states of a linear molecule molecule are sketched. The pendular states are linear combinations of the field-free rotational states, $|\tilde{J}M\rangle = \sum_J d_{JM} |JM\rangle$, involving either even or odd J 's. Each resulting wave function has definite parity given by $(-1)^J$. As a consequence the each pendular state of a tunneling doublet has opposite parity. From Fig. 2.1 it is clear that each pendular state experiences a different degree of confinement due to its position in the double well. No additional states are being created by the interaction with the laser field, since all the rotational quantum states initially populated are adiabatically transferred to the corresponding pendular states. As a consequence the degree of alignment is determined by the rotational quantum state in which the molecule resides prior to exposure to the alignment field. Consequently, the degree of alignment becomes a function of the rotational temperature of the ensemble of molecules. The dependence is

monotonous with the strongest alignment obtained at the lowest rotational temperatures. Furthermore, since Eq. (2.12) depends on the square of the pulse envelope the interaction follows the intensity profile of the laser pulse. The strongest interaction and hence the strongest alignment is, therefore, found at the peak of the alignment pulse. The higher the peak intensity of the laser field the stronger the confinement of the pendular states in the double well, however limited by the threshold of ionization. It is possible to achieve very high degrees of confinement using adiabatic alignment [60]. One disadvantage of adiabatic alignment is, however, that the laser field is present during the alignment. This may perturb with applications of aligned molecules.

2.3 Mixed-Field Orientation

The theoretical framework for laser induced orientation by the combined action of a static electric and a laser field was likewise proposed by Friedrich and Herschbach in 1999 [24, 25]. In 'brute force orientation' directional hybrid states are created that librate around the static field axis. Orientation achieved in this way requires very strong static fields. The effective potential of a molecule in a combined static electric and laser field is described by Eq. (2.7) and Eq. (2.8). For a linear molecule in a laser field linearly polarized along the axis of a dc electric field this reduces to

$$V_{\text{eff}}(t) = -\frac{E_0(t)^2}{4} (\Delta\alpha \cos^2 \theta + \alpha_{\perp}) - \mu_0 E_{\text{stat}} \cos \theta, \quad (2.12)$$

where θ is the angle between the static field axis (i. e. laser field polarization vector) and the permanent dipole moment axis of the molecule, corresponding to the static field and dipole moment being parallel at $\theta = 0^\circ$ and antiparallel at $\theta = 180^\circ$.

In Fig. 2.2 the effective potential of carbonylsulfide in the presence of a non-resonant laser field (a) and its combination with a static electric field (b) is plotted. Moderately intense dc fields are required to perturb the potential, however, combining the action of a static electric and a non-resonant laser field in the adiabatic regime it is possible to achieve high degrees of orientation even with a weak static field for any polar molecule, linear, symmetric or asymmetric receding in its low-lying rotational states. Orientation achieved in this regime can be ascribed to a pseudo first order Stark effect of the pendular states created by the adiabatic alignment laser field. As described in the previous section the pendular states occur as tunneling doublets of opposite parity in the double well potential. Introducing a static electric field connects the nearly degenerate energy levels and the second order alignment is converted into strong first order orientation through a pseudo first order Stark effect. In a simplistic two-state model

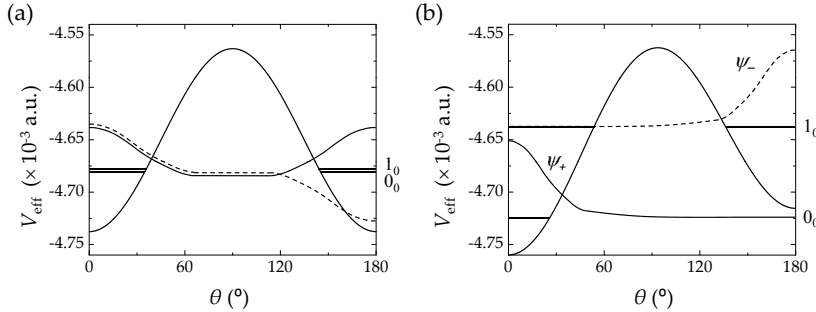


Figure 2.2: Comparison of the effective potential for carbonylsulfide (OCS) resulting from a laser field alone (a) and the combination of a laser field and a static electric field (b). A laser intensity of 1×10^{12} W/cm² and a electric field of 15 kV/cm have been assumed. A sketch of the first tunneling doublet (a) and their splitting, when the static field is included (b) as well as the spheroidal wave functions (a) and linear combination hereof (b), are shown to illustrate the mechanism responsible for mixed field orientation. See text for details.

the interaction with the static field creates linear combinations of the lower $|\tilde{J}M\rangle$ and upper $|\tilde{J} + 1M\rangle$ pendular state of the tunneling doublets, resulting in the wave functions

$$\psi_+ \propto |\tilde{J} + 1M\rangle + |\tilde{J}M\rangle \quad (2.13)$$

$$\psi_- \propto |\tilde{J} + 1M\rangle - |\tilde{J}M\rangle \quad (2.14)$$

The wave functions of the first two pendular states of a linear molecule are sketched in Fig. 2.2 a). Due to the opposite parity of the two pendular states involved in the wave functions the amplitude of the ψ_+ wave function will cancel at $\theta = 180^\circ$ and localize at $\theta = 0^\circ$ (see sketch on Fig. 2.2 b). Likewise the amplitude of the ψ_- wave function will cancel at $\theta = 0^\circ$ and localize at $\theta = 180^\circ$. In other words both ψ_+ and ψ_- represent oriented states. Under typical experimental conditions more than one state is initially populated. Therefore, the net orientation of a molecular sample will be strongly reduced. In practice describing the mechanism behind mixed field orientation is much more complicated. For a detailed description of the theory the reader is referred to [24, 25].

2.4 Nonadiabatic Alignment

If a short laser pulse is used to induce alignment, again short compared to the rotational dynamics of the molecule, the molecule experiences a rotational kick in the direction of the polarization of the laser, making the molecules spin. The interaction is said to be nonadiabatic. In the quantum mechanical description the interaction with the laser field creates a coherent superposition of eigenstates through a series of nonresonant Raman transitions, i.e. a rotational wave packet, that will de-phase and re-phase creating a time-dependent alignment long after the pulse has been switched off. The creation of a rotational wave packet by a short nonresonant kick pulse was considered to induce molecular alignment by Seideman [8], that found substantial rotational excitation under conditions typically used in time-resolved spectroscopy experiments. The dynamics introduced by non-adiabatic alignment is in close resemblance to the rotational recurrences introduced by weak fields in Rotational Coherence Spectroscopy (RCS) [61, 62]. In RCS, a field having its roots in the pioneering work by Lin and coworkers [63, 64], coherent superpositions of rotational states are induced in either the ground or an electronically excited state by irradiation of a sample of molecules with a short pump laser pulse. Subsequently the time-evolution is measured by a delayed probe pulse or a fast photodetector, observing polarized emission as a function of time or by monitoring an observable associated with a transition induced by a delayed probe, respectively. The angular confinement in RCS experiments is modest, however the position of the rotational revivals provide direct information about the rotational constants of the molecule and important spectroscopic information of numerous molecular systems has been gained from RCS experiments [61, 62, 65].

Although a quantum mechanical approach is necessary in order to fully describe and understand nonadiabatic alignment, classical mechanics provides a clear intuitive understanding and has proven to be correct in describing the short time dynamics of non-adiabatic alignment [66–68]. This classical approach is often referred to as the δ -kick model.

2.4.1 δ -Kick Model

In the short pulse limit the laser pulse is much shorter than the rotational period of the molecule. Due to inertia, the molecules do not respond immediately to the alignment pulse, hence the molecular rotation is frozen in the interaction moment with the laser pulse. In classical terms the laser pulse imparts a kick on the molecules, leading them to spin towards the direction of the polarization of the laser field [66, 67].

Consider a classical ensemble of linear rigid rotors, initially in their ground

state and isotropically distributed, interacting with a short electromagnetic pulse through the interaction potential described in Eq. (2.12). The rotors will experience a torque, $\boldsymbol{\tau} = -\mathbf{r} \times \mathbf{F}$, where the force is given by the negative of the gradient of Eq. (2.12) $\mathbf{F} = -\nabla V_{\text{ind}}(t)$. The angular momentum transferred to the rotors can be calculated from

$$J = \int \tau dt = \frac{1}{4} \Delta\alpha \int E_0(t)^2 dt \sin(2\theta_0) \equiv IP \sin(2\theta_0), \quad (2.15)$$

where θ_0 is the initial angle between the rotor and the polarization of the laser pulse, I is the moment of inertia and P is the interaction or kick strength. The magnitude of the angular momentum of a rigid body rotating around a symmetry axis is given by $|J| = I|\dot{\theta}|$, therefore the angular velocity of the molecules depends on their orientation with respect to the polarization of the alignment laser prior to the interaction, as follows

$$\dot{\theta} = -P \sin(2\theta_0). \quad (2.16)$$

It is clear that for rotors initially oriented close to the polarization axis of the laser pulse, i. e. $\theta_0 \sim 0^\circ, 180^\circ$ where $\sin(2\theta_0) \approx 2\theta_0$, the angular velocity becomes proportional to the initial angle. At $t = 1/(2P)$ all these rotors will be aligned along the polarization axis. Molecules initially located at large angles, i. e. close to 90° , will lag behind and not reach confinement at the same time as the rest of the ensemble of molecules. Therefore, no matter how hard the molecules are kicked by the alignment pulse there is a limitation to the degree of alignment.

It is clear that since all the rotors have nonzero angular velocities upon alignment, the ensemble of rotors is only aligned for a short period of time.

2.4.2 Quantum Mechanical Description

To understand the alignment dynamics following irradiation by a short laser pulse it is necessary to solve the time dependent Schrödinger for the total Hamiltonian given in Eq. (2.10). Solving the time dependent Schrödinger equation is not a trivial problem, and cannot be done analytically, but demands a numerical approach. The solution emerges from expanding the unknown initial wave function in an appropriate orthonormal rotational basis

$$|\psi_i(t)\rangle = \sum_{\mathbf{n}} C_{\mathbf{n}}^i(t) |\mathbf{n}\rangle. \quad (2.17)$$

The subscript i denotes the set of initial conditions, including the energy level of the initial state. The choice of rotational basis set $\{|\mathbf{n}\rangle\}$ is a matter of convenience and numerical efficiency and often chosen to be the orthonormal eigenstates of \hat{H}_{rot} .

Substituting Eq. (2.17) into the time-dependent Schrödinger equation and projecting onto a specific eigenstate $|\mathbf{n}'\rangle$ leads to a set of coupled first order differential equations

$$i\hbar \frac{\partial}{\partial t} C_{\mathbf{n}'}^i(t) = C_{\mathbf{n}'}^i(t) E_{\mathbf{n}'} + \sum_{\mathbf{n}} C_{\mathbf{n}}^i(t) \langle \mathbf{n}' | \hat{V}_{ind}(t) | \mathbf{n} \rangle. \quad (2.18)$$

The solution to the set of coupled differential equations determines the form of the wave packet. Once the expansion coefficients are found it is trivial to compute all observables of interest as a function of time.

After the interaction with the laser pulse the molecules rotate free of external fields. The time evolution of the wave packet is found by considering the time evolution of each of the components in the wave packet

$$|\psi_i(t)\rangle = \sum_{\mathbf{n}} C_{\mathbf{n}}^i(t_0) |\mathbf{n}\rangle \cdot e^{iE_{\mathbf{n}}(t-t_0)/\hbar}, \quad (2.19)$$

where t_0 is the time when the molecules are said to be field-free and $E_{\mathbf{n}}$ are the eigen-energies of the stationary Schrödinger equation

2.4.3 Measuring the Degree of Alignment

To quantify the degree and the time-evolution of the alignment the most commonly used observable is the expectation value of $\langle \cos^2 \theta \rangle$

The initial state is a thermal average of states defined by the rotational temperature, T_{rot} , making the thermally averaged expectation value an incoherent sum of expectation values

$$\langle \cos^2 \theta \rangle_T = \sum_i w_i(T_{rot}) \langle \psi_i(t) | \cos^2 \theta | \psi_i(t) \rangle_i, \quad (2.20)$$

where $w_i(T_{rot})$ are normalized weight functions. The population of the initial states is normally assumed to follow the Boltzmann distribution. In that case the probability that a given initial state is populated is given by $w_i(T_{rot}) = Q_{rot}^{-1} e^{-E_i/k_B T_{rot}}$ where $Q_{rot} = \sum_j e^{-E_j/k_B T_{rot}}$ is the rotational partition function. Since the eigenstates are time-dependent the expectation value of $\cos^2 \theta$ likewise becomes time-dependent. Upon the time evolution of the wave packet the different components of the wave packet will come into and out of phase with each other leading to recurrences in the alignment degree at well-defined time delays. These recurrence of the alignment degree are termed rotational revivals.

3

EXPERIMENTAL SETUP

Two types of experiments will be presented in this thesis. In the first experiments molecular alignment and orientation is induced by a combination of a non-resonant, non-ionizing laser field and a static electric field and subsequently characterized. In the second type of experiments photoelectron angular distributions from aligned or oriented molecules are measured. The basic idea behind the experiments is threefold. First, an ensemble of rotationally cold molecules is prepared in a supersonic expansion into vacuum. After the expansion the molecular beam is skimmed twice before entering a electrostatic beam deflector, where polar molecules are deflected according to their initial rotational quantum state. Second, after the deflector a subset of quantum states is selected and crossed by a non-resonant, non-ionizing laser pulse inducing alignment and orientation by the combined action of the laser and a static electric field. Alignment and orientation is created either in the adiabatic limit using a nanosecond laser pulse or in the impulsive limit using a short (fs-ps) laser pulse, creating a rotational wave packet. Finally, either the degree of alignment and orientation of the ensemble of molecules is measured or the molecules are singly ionized and the molecular frame photoelectron angular distributions (MFPADs) are measured.

There are different approaches to characterizing molecular alignment and orientation such as weak field polarization techniques [69], optical Kerr effect [54, 70], Raman [14], linear dichroism [71, 72] and resonant dissociation [73]. The

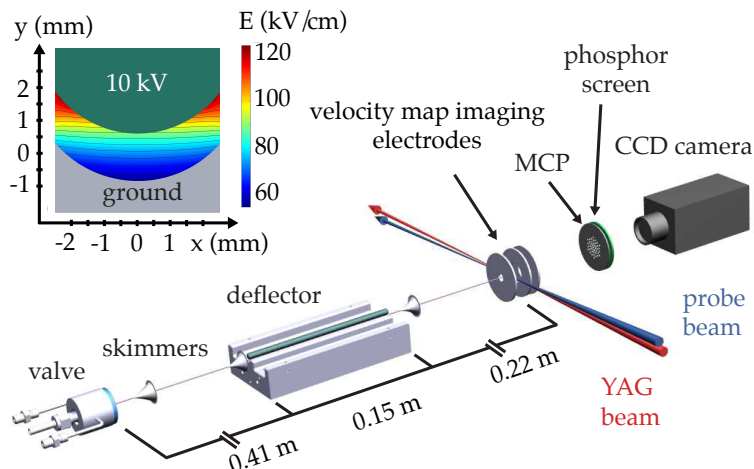


Figure 3.1: Schematic overview of the experimental setup.

approach used in our lab to detect alignment and orientation relies on photo-fragment imaging from Coulomb explosion.

A schematic overview of the experimental setup is provided in Fig. ???. A detailed description of the distinct parts of the setup and experimental steps is provided in the following sections.

3.1 The Optical Setup

The cornerstones of our optical setup are the femtosecond and nanosecond laser systems. A schematic illustration of the laser and optical setup is shown in Fig. 3.2. The nanosecond laser system consists of an injection seeded, Q-switched Nd:YAG laser (Spectra Physics, Quanta Ray Pro 270-20). The laser operates at a repetition rate of 20 Hz and delivers 10 ns long pulses at a wavelength of 1064 nm with pulse energies up to 1.5 J.

The femtosecond laser system is a regenerative, chirped pulse amplified Ti:Sapphire laser system. The system is divided into two parts, an oscillator and an amplifier. The oscillator (Spectra-Physics Tsunami) is pumped by a diode pumped Nd:YVO₄ cw laser (Spectra-Physics Millennia V), that through second harmonic generation provides a 532 nm output of more than 5 W. The gain medium in the Tsunami laser is a Ti:sapphire crystal, and the laser operates around 800 nm. It generates sub 100 fs pulses through Kerr lens modelocking. The pulses have an energy of ~ 10 nJ and a repetition rate of 82 MHz.

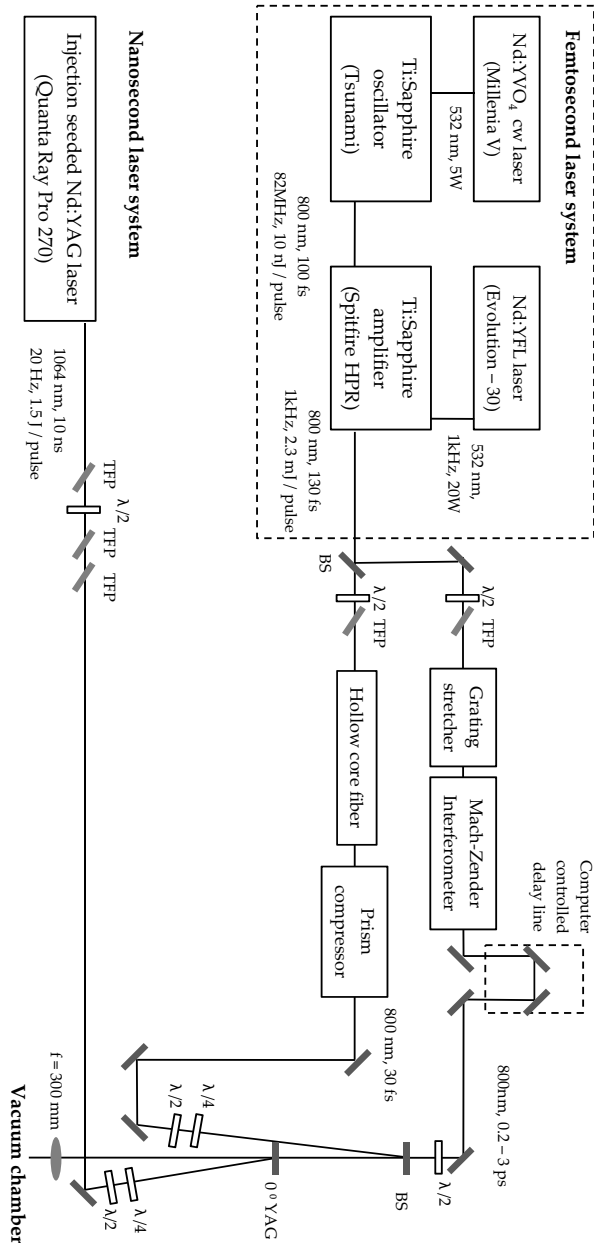


Figure 3.2: Schematic overview of the optical setup.

The train of low energy laser pulses from the oscillator are used to seed the amplifier. The amplifier is a Spectra-Physics Spitfire-HPR laser operating at 1 kHz. To operate without the risk of optical damage, the Spitfire uses the technique of chirped pulse amplification. The seed pulses are first temporally stretched using positive Group Velocity Dispersion in a grating stretcher, before regenerative amplification in a Ti:Sapphire crystal that has been optically excited by a pulse from a Nd:YFL laser (Evolution-30 laser, that like the Millennia is a diode pumped, intra-cavity doubled laser. It produces Q-switched pulses with average energy > 20 mJ at 527 nm, with a repetition rate of 1 kHz). Only one out of 82 000 pulses from the Tsunami is amplified, giving a repetition rate of 1 kHz. The pulse to be amplified is admitted into the resonator by a Pockels cell. A second Pockels cell switches the pulse out of the resonator again, insuring that the pulse is ejected after sufficient round trips, giving an overall amplification greater than 10^6 . After amplification the pulses are re-compressed in a grating compressor. The final output from the laser is ~ 130 fs pulses with a central wavelength of 800 nm, pulse energies of up to 2.3 mJ and a repetition rate of 1 kHz.

3.1.1 Alignment Pulses

To induce adiabatic alignment the fundamental output from the nanosecond laser is used. The requirement for adiabatic alignment is a smooth turn-on of the nonresonant aligning laser pulse on a time scale that is longer than the inherent rotational period of the molecules. The rotational periods of the molecules studied in this thesis are all less than 1 nanosecond. The injection seeder ensures a smooth temporal envelope and the pulse duration of 10 ns fulfills the criteria of the slow turn-on. Furthermore, at a wavelength of 1064 nm, the photon energy corresponding to 1.17 eV is far too low to excite any electronic states and far too high to address any vibrational states of most molecules, making it suitable for alignment. To control the pulse energy a combination of a half wave plate and a sequence of thin film polarizers is used. A half and a quarter wave plate ensures full control of the polarization state of the pulse. The nanosecond laser is synchronized electronically to the femtosecond laser with an overall timing jitter of less than ± 1 ns.

To induce nonadiabatic alignment a nonresonant, nonionizing near infrared laser pulse is needed. For this purpose part of the output from the femtosecond laser system is used. In order to create a high degree of alignment the temporal duration of the alignment laser is crucial, hence using the direct output from the laser of 130 fs limits the kick strength the molecules can withstand before ionizing. Therefore an easy way of controlling the duration of the alignment pulse is needed. Experimentally this is achieved by changing the temporal chirp of the

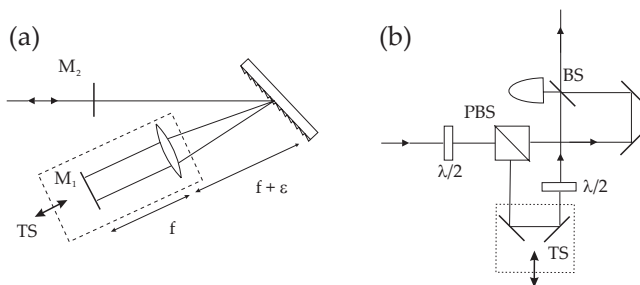


Figure 3.3: (a) The grating stretcher used to stretch the alignment pulses. (b) Schematic drawing of a general grating compressor

laser pulses using a grating stretcher. The grating stretcher exploits the fact, that the wavelength dependent reflection angle of a grating or a prism introduces group velocity dispersion [74, 75]. We use a folded, single grating design as shown in Fig. 3.3 (a).

In the grating stretcher the collimated, transform-limited output from the laser is sent onto the diffraction grating, causing different frequency components of the laser pulse to be reflected at slightly different angles. After the grating a combination of a cylindrical lens and a folding mirror (M_1) is used as a 1:1 telescope, projecting the image of the grating back onto the grating. For a configuration where the grating is displaced from the focal distance of the lens, the beam reflected from the grating will experience a temporal chirp as different frequency components travel different path lengths. The pulse, however, also gains a spatial chirp. The spatial chirp is removed by reflecting the beam back towards the grating for a second complete passage, using a second folding mirror (M_2). This removes the spatial chirp while doubling the temporal chirp, and effectively stretching the transform limited pulse.

The total amount of group velocity dispersion (GVD) added to the pulse can be calculated from the following expression [74, 76]

$$\phi''(\omega) = \frac{d^2\phi(\omega)}{d\omega^2} = -\frac{2\varepsilon\lambda^3}{\pi c^2 d^2} \left[1 - \left(\frac{\lambda}{d} - \sin\gamma \right)^2 \right]^{-1}. \quad (3.1)$$

where λ is the central wavelength of the laser, γ is the near Littrow angle of the grating, d is the groove spacing of the grating and ε is the displacement of the grating from the focal point. The width of the pulse with a certain amount of

GVD can be calculated as [77]

$$\tau = \tau_0 \sqrt{1 + \left(\frac{4 \ln(2) \phi''(\omega)}{\tau_0^2} \right)^2}, \quad (3.2)$$

where τ_0 is the full width at half maximum (FWHM) of the transform limited Gaussian pulse.

One benefit of introducing a telescope in connection with gratings is that it allows us to control the sign of the dispersion, as ε can take on positive as well as negative values. If $l < f$, i.e. $\varepsilon < 0$, the setup acts as a stretcher, creating a positive chirp, while the opposite is true for $\varepsilon > 0$.

From Eq. (3.1) and Eq. (3.2) one can calculate the displacement required to stretch a pulse. In our setup $d^{-1} = 1200 \text{ mm}^{-1}$ and the near Littrow angle at $\lambda_l = 800 \text{ nm}$ is $\gamma = 28.7^\circ$. In order to stretch the pulse from its original 130 fs to a pulse duration of 2 ps, calculations predict, that the displacement of the grating from the focal point is 10.6 mm. Experimentally we found it to be $\sim 11.5 \text{ mm}$, which is in good agreement with the calculated value.

In order to enhance the degree of alignment a double pulse arrangement can be used. In this regime the first pulse serves to pre-align the ensemble of molecules before a second pulse is sent in. In order to have optimum conditions a control of the relative intensity and temporal delay of the two pulses is needed. For this purpose we use a modified Mach-Zender interferometer^a (Fig. 3.3 (b)). To separate and adjust the relative energy in the two arms a half-wave plate in front of a polarizing beamsplitter (PBS) is used. The second half-wave plate in the setup ensures that the polarization of the two pulses is the same, by rotating the polarization by 90° . Placing the mirrors of one arm on a translational stage (TS) ensures control of the relative timing. The two pulses are finally recombined in a 50/50 beamsplitter (BS).

The pulse energy of the nonadiabatic alignment beam is controlled using a combination of a half-wave plate followed by a polarizing beam-splitter cube.

The grating stretcher described above was later upgraded by replacing the reflective grating with two holographic transmission gratings to avoid distortion of the beam profile by the cylindrical lens and to minimize losses.

3.1.2 Probe Pulses

To probe the degree of alignment a Coulomb explosion probe is used. The basic idea behind this probe scheme is to create a multiply charged, unstable molecular ion by ripping off several electrons using an intense laser field. Due to

^aThe modification consists of using the combination of a half-wave plate and a polarizing beam-splitter.

the excess positive charge of the molecule, the Coulomb repulsion between the nuclei will cause the molecular ion to dissociate rapidly. The molecule Coulomb explodes transferring the Coulomb energy to the ion fragments in the form of kinetic energy [16].

For many molecules, the Coulomb explosion process leads to fragment ions that recoil along particular bond axes. Recording the emission direction of the fragment ions, therefore, provides direct information about the spatial orientation of a particular bond at the instant of ionization. As an example, for iodobenzene recording the velocity vectors of I^+ ions gives information about the C-I axis, which is also the axis that is being aligned by a linearly polarized alignment pulse.

Iodine ions are easily isolated from other ions in a time-of-flight spectrometer, due to the large mass to charge ratio. The iodine ions are accelerated by a static electric field towards a detector. Velocity map imaging of the I^+ fragment can provide a quantitative measure of the degree of alignment as will be addressed in Sec. 3.2, where a detailed description of the detection system is given.

It is essential for the experiment that the probe pulse does not distort the orientation of the molecule on its own prior to dissociation. Therefore the molecule effectively has to be frozen during the multi electron ionization otherwise the electric field from the laser pulse could exert a large torque on the molecule, creating alignment on its own. Therefore, the Coulomb explosion pulse has to be short and intense enough for the molecule to dissociate before changing the alignment dynamics.

In this setup the short pulses are generated from the last part of the 130 fs output from the femtosecond laser system. The creation of short pulses is, according to the time-energy uncertainty principle, limited by the spectral width of the pulse. Broadening the spectrum of the pulses using self phase modulation in an argon filled hollow core fiber, followed by recompression in a pair of prisms, intense 800 nm pulses with a duration of ~ 30 fs, focussed down to peak-intensities up to $5.4 \times 10^{14} \text{W/cm}^2$ are obtained. The beam is focussed into a 50 cm long hollow core fiber with a core diameter of $\sim 250 \mu\text{m}$, using a $f = 60$ cm lens. The hollow core fiber is placed inside a 125 cm long plexiglas tube, with BK7 windows in each end, for the beam to propagate through. After the tube a concave lens with $f = -100$ cm re-collimates the beam.

The dielectric response of an isotropic media changes and becomes nonlinear when exposed to an intense electric field, which can lead to self phase modulation [78]. The nonlinear medium used here is argon.

With a pressure of 2 – 2.5 bar inside the tube and a pulse energy of $\sim 400 \mu\text{J}$ before the tube, we obtain a spectral broadening from ~ 10 nm to ~ 50 nm. The transmission efficiency through the tube is $\sim 65\%$

After broadening of the spectrum the pulses are re-compressed in a pair of prisms. Similar to gratings negative angular dispersion can be obtained in a pair of prisms. The group velocity dispersion generated in a pair of Brewster cut prisms from angular dispersion is given by [75, 77]

$$\frac{d^2\phi(\omega)}{d\omega^2} \approx -4L_p \frac{\lambda^3}{2\pi c^2} \left(\frac{dn}{d\lambda} \right)^2, \quad (3.3)$$

where L_p is the distance between the apexes of the two prisms. Angular dispersion is however not the only contribution to the GVD in a prism compressor. Since the beam passes through a certain amount of glass in each prism the GVD induced in the material can not be neglected. With $x = l_g$ corresponding to the mean glass path, the total dispersion of the prism sequence reads [77]

$$\frac{d^2\Phi_{tot}(\omega)}{d\omega^2} \approx \frac{\lambda^3}{2\pi c^2} (l_p n'' - 4L_p n'^2), \quad (3.4)$$

where n' and n'' can be calculated using the Sellmeier equations [79].

To ensure that the pulses are as short as possible inside the vacuum chamber, it is necessary to compensate for the dispersion in optical components after the compressor. This is done by fine tuning the amount of prism glass, while optimizing the ion signal from multiphoton ionization of argon inside the chamber.

For the photoelectron measurements a singly ionizing pulse is needed. For that purpose the intensity of the probe pulse is damped using reflective density filters until the molecules only undergo single ionization, with essentially no fragments. The density filters introduce dispersion to the pulse, due to the extra amount of glass added to the beam path. This is however compensated for by tuning the amount of glass introduced in the prism compressor.

3.1.3 Combining and Characterizing the Beams

The laser beams are all overlapped collinearly along a single axis before focussing onto the molecular beam. The 800 nm nonadiabatic alignment beam and the Coulomb explosion beam are overlapped in a 0° beam-splitter by taking the reflection of the Coulomb beam and sending the alignment beam in from behind. The nanosecond YAG beam is overlapped with the 800 nm femtosecond beams in a zero degree dichroic mirror with high reflectivity for 1064 nm. In this fashion a collinear overlap is ensured, however with the disadvantage of a high loss of pulse energy of the 800 nm beams. The beams are then focussed onto the molecular beam using a $f = 30$ cm lens. With telescopes in the nonadiabatic and adiabatic alignment beams, the spotsizes of the beams in the focus are adjusted. The polarization states of the different beam are controlled by half wave and

quarter wave plates placed in the beam path of each beam just before collinear combination.

Overlapping the beams is closely connected to the characterization of the beam. The characterization of the beams requires the measurement of three parameters; The pulse energy, E_{pulse} , and the spatial and the temporal pulse profile, determined by the focal spot size, w_0 , and the pulse duration τ .

The intensity of a Gaussian laser pulse can be described as [80]

$$I(\mathbf{r}, t) = I_0(t) \exp\left(-2\frac{r^2}{w_0^2}\right), \quad (3.5)$$

where r is the distance from the center of the beam, $r^2 = x^2 + y^2$, w_0 is the spot size measured from the center of the pulse till the place where the intensity has dropped to I_0/e . It can be calculated from the full width at half maximum value

$$w_0 = \frac{w_{FWHM}}{\sqrt{2 \ln 2}}. \quad (3.6)$$

For a Gaussian pulse envelope we can derive

$$I_0(t) = \frac{\varepsilon_0 c}{2} |E_0(t)|^2 \equiv I_0 \exp\left(-4 \ln 2 \frac{t^2}{\tau^2}\right), \quad (3.7)$$

where τ is the pulse duration measured at FWHM and I_0 is the peak intensity.

The pulse energy can be found by integrating Eq. (3.5) over x , y and t . From that one can derive an expression for the peak intensity

$$I_0 = \frac{4\sqrt{\ln 2}}{\pi^{3/2}} \frac{E_{\text{pulse}}}{w_0^2 \tau}. \quad (3.8)$$

The spatial overlap of the two beams is ensured by first overlapping the beams in a 10 μm pinhole outside the vacuum chamber. This is done by inserting a metal mirror before the vacuum chamber window. In order to imitate the conditions inside the vacuum chamber, the beams propagate through a replica of the vacuum chamber window. In the focus of the beams the 10 μm pinhole is placed. The transmission through the pinhole is measured with a photodiode. By optimizing the photodiode signal a good spatial overlap is ensured. Depending on the molecules a final optimization of the overlap is done inside the vacuum chamber, by optimizing the yield of a particular photofragment, in a geometry sensitive to the presence of both laser pulses.

The temporal overlap is found by carrying out a cross-correlation using sum-frequency mixing in a non-linear crystal.

First the pinhole is replaced by a BBO (beta barium borate: $\beta\text{-BaB}_2\text{O}_4$) crystal, this ensures that the crystal is placed in the foci of the two laser beams.

First, the alignment beam is set to have ordinary polarization with respect to the crystal (in this setup this means vertical polarization) using a half-wave plate. From the alignment pulse alone it is now possible to generate 400 nm using type I second harmonic generation in the BBO crystal. The frequency doubled 400 nm light is measured with a photodiode through a bandpass filter (TR03). After optimization of the signal the two beams are combined, with the Coulomb beam being polarized orthogonally to the alignment beam. At 800 nm type II second harmonic generation is obtained by turning the crystal 22° with respect to type I SHG around the ordinary axis of the crystal, i. e. vertical axis. At this angle 400 nm is generated only when the two beams are overlapped in time. By measuring the photodiode signal as a function of the delay between the two pulses the cross correlation trace is found. The cross-correlation measurement has been completely computerized with a data acquisition program that measures the photodiode signal while changing the delay of the alignment beam. The alignment beam is optically delayed using a translational stage. This stage is driven by a stepper motor, also computer controlled through the data acquisition program.

3.2 Vacuum and Detection System

The experiments described in this thesis were all performed under ultra high vacuum in two different vacuum chamber systems.

The experiments involving carbondisulfide (Chapter 7) were conducted on a vacuum chamber constructed in 2006. This vacuum chamber system is composed of two differentially pumped vacuum chambers, a source chamber and a target chamber separated by a 1-mm-diameter skimmer. The purpose of the skimmer is twofold: One, it determines the width of the molecular pulse in the interaction region and two, it enables differential pumping of the two chambers. The vacuum system is based on ultra high vacuum (UHV) technology. Each chamber is pumped by a 500 l/s turbomolecular pump backed by foreline vacuum pumps. The background pressure in the source chamber is $\sim 3 \times 10^{-8}$ mbar.

The molecular beam is expanded from a miniaturized, pulsed, high pressure Even-Lavie valve placed at the bottom of the source chamber, operated at a maximum repetition rate of 40 Hz. When the valve operates at a stagnation pressure of 100 bar and a repetition rate of 33 Hz, the pressure in the source chamber stays below 2×10^{-5} mbar due to the very short opening time of the valve ($\sim 10 \mu\text{s}$). From the source chamber the molecular beam expands vertically through the skimmer into the target chamber, where one or more laser beams can be made to intersect it at 90° . The skimmer is located ~ 15 cm above the nozzle and after another ~ 30 cm the molecular beam reaches the interaction region. At this point

the gas pulse is ~ 3 mm wide. From the interaction region the ion fragments are guided by a static electric field onto the detection system, positioned on axis with the molecular beam. The background pressure in the target chamber is $\sim 6 \times 10^{-10}$ mbar and increases to a maximum of 1×10^{-8} mbar when operating at 33 Hz, 100 bar helium (He).

From early in my PhD project I took part in the design and construction of a new molecular beam machine. The vacuum chamber system was finished and operational in 2008 and since then all experiments were conducted on this chamber. The molecular beam machine consists of three differentially pumped vacuum chambers; The source chamber housing a pulsed valve (pumped by a 2000 l/s turbomolecular pump), the deflector chamber (pumped by a 500 l/s turbomolecular pump) and the target chamber housing the ion/electron spectrometer (pumped by a 500 l/s turbomolecular pump). The molecular sample is seeded in an inert carrier gas and expanded through a pulsed valve into vacuum. In order to obtain optimal cooling of the molecular beam, a miniaturized, high pressure Even-Lavie valve [81] is used operating at a maximum repetition rate of 1 kHz and at a backing pressure of 90 bar of helium (He) or 25-30 bar of neon (Ne) limited by the onset of cluster formation. While rotational temperatures down to 0.4 K have been achieved under similar conditions [82], the typical rotational temperature in our experiments is ~ 1 K. Two 1-mm-diameter skimmers placed 15 cm, separating the source and the deflector chamber, and 38 cm downstream from the nozzle collimate the molecular beam before it enters a 15-cm-long electrostatic deflector.

After passing through the deflector, the molecular beam enters the differentially pumped detection chamber via a third skimmer of 1.5 mm diameter. In the detection area, the molecular beam is crossed by one or two laser beams that are focused by a spherical lens with a focal length of $f = 300$ mm. The lens is mounted on a vertical translation stage so that the height of the laser foci can be adjusted with high precision. Ionic fragments produced in the Coulomb explosion are accelerated in a velocity focusing geometry towards the detector. The detector can be gated with a time resolution of ~ 90 ns, which allows for mass selective detection of individual fragments. A microchannel plate (MCP) detector backed by a phosphor screen is employed to detect the position of mass-selected ions.

3.2.1 The Molecular Beam

The molecular beam is created by a supersonic expansion of a mixture of the molecular gas and an inert carrier gas (He or Ne).

In a supersonic expansion [83] a high pressure gas mixture of the molecular sample and a carrier gas is expanded through a small orifice into vacuum. Since

a large fraction of the mixture consists of the carrier gas, the molecule in question will undergo a large number of collisions with the carrier gas atoms. During the expansion the random thermal motion of the static gas is converted into a directed motion in the expanding gas. The sample molecules are accelerated to the light carrier gas velocity (1800 m/s for He and 800 m/s for Ne at room temperature). This leads to a direct cooling of the translational temperature, defined by the width of the velocity distribution. In the early stages of the expansion, collisions in the jet between molecules with small relative velocities carry away the energy of the internal degrees of freedom. The rotational and vibrational cooling achieved in the jet is thus determined by the total number of collisions the molecules undergo before the carrier gas is too diluted downstream and hence the cooling terminates [83].

In our laboratory we use two miniaturized, pulsed, high pressure valve (E.L.-7-2004 and E.L.-7-4-2005-HRR) designed and built by Uzi Even and Nachum Lavie [81, 82]. The valves are actuated by driving a current pulse through a solenoid. The valve can be operated at a maximum repetition rate of 40 Hz and 1 kHz, respectively. The molecular gas is expanded through a conical nozzle of 250 μm diameter. Compared to a sonic nozzle this reduces the divergence of the beam significantly and hence increases the sample density in the interaction region [81]. In the experiments described in the following chapter different molecules are studied.

The construction of the valve, with the sample holder located inside the valve body makes it possible to run a wide range of molecules, liquids as well as solids, as it can operate in the temperature range 30 – 250°C. The density of the molecular gas is controlled by controlling the temperature. A vapor pressure of only a few mbars are required and expanded in up to 100 bar He or 20-25 bar of Ne, limited by the onset of cluster formation. Hence, only a small fraction of the mixture gas contains the molecule to be studied. This is a specially important feature of the valve as it provides an easy way of tuning the rotational temperature of the seed molecule. At a stagnation pressure of only a few bars the cooling is not very efficient and rotational temperatures of tens of Kelvins are produced. Increasing the backing pressure, however, increases the cooling efficiency and at a He stagnation pressure of 100 bar sub-Kelvin temperatures can be achieved [82]. The rotational temperature is to some extent also effected by the amplitude and duration of the current pulse driving the solenoid valve, hence careful optimization is required prior to an experiment.

3.2.2 Electrostatic Beam Deflection

Two 1-mm-diameter skimmers (Beam Dynamics, Type II) placed 15 cm, separating the source and the deflector chamber, and 38 cm downstream from the

nozzle collimate the molecular beam before it enters a 15-cm-long electrostatic deflector. A cut through the electrodes of the deflector is shown in the inset of Fig. 3.1 together with the electric field created. A trough with an inner radius of curvature of 3.2 mm at ground potential and a rod with a radius of 3.0 mm at high voltage create a two-wire field. The vertical gap across the molecular beam axis is 1.4 mm, while the smallest distance between the electrodes is 0.9 mm. The two-wire field geometry is ideally suited for molecular beam deflection. The gradient of the electric field along the vertical direction is large and nearly constant over a large area explored by the molecular beam, while the electric field is very homogeneous along the horizontal direction. Thus a polar molecule experiences a nearly constant force in the vertical direction independent of its position within the deflector, while the force in the horizontal direction (i. e. broadening of the beam in the horizontal direction) is minimized. In our setup, the deflector is mounted such that molecules in high-field-seeking (low-field-seeking) quantum states are deflected upwards (downwards).

The new vacuum chamber was later upgraded. Two changes were imposed. First, to ensure better cooling the first skimmer was replaced by a larger one of different shape (Beam Dynamics 50.8, 3 mm aperture). Second, a set of capacitor plates (17 cm long) were inserted in the region between the deflector and the interaction region, i. e. from the exit of the deflector to the repeller plate of the VMI spectrometer discussed next. The purpose of the capacitor plates is to maintain a weak field after the molecules leave the deflector. The separation between the plates is 2.7 mm. To make room for the capacitor plates the final skimmer was removed. The effect of the capacitor will be discussed in App. A.

3.2.3 The Velocity Map Imaging Spectrometer

In the interaction region the molecular beam is crossed at right angles by the focussed laser beams. In this experiment the molecules are first hit by the non-adiabatic or adiabatic alignment pulse and subsequently Coulomb-exploded to create detectable ion-fragments that recoil along the bond axis as described in Sec. 3.1.2. From the recoil velocities of the ion fragments one can extract direct information about the spatial orientation of the molecules prior to dissociation. Hence, a way of detecting the ion-fragments is needed.

To project the ions onto a detector a velocity map imaging spectrometer is used. It consists of an open three-electrode electrostatic lens that accelerates the ions towards a position sensitive detector.

Velocity map imaging was first introduced by Eppink and Parker [84, 85] in 1997. They showed how electrostatic ion lenses allowed mapping of all particles with the same initial velocity vector onto the same point on a 2D detector, irrespective of their position of creation in the ionization volume. It is essential that

the position on the detector only depends on the initial velocity of the ion and not the spatial position, since the probed volume cannot be regarded as a point. In the interaction region the molecular beam has a width of a few mm (~ 3 mm in the "old" and ~ 2 mm in the "new" vacuum chamber system) and the Coulomb explosion beam is focused to a spot size of ~ 25 μm , leading to a Rayleigh range [80] given by $Z_R = \pi w_0^2 / \lambda \approx 2.5$ mm. The ions are hence created in a long ellipsoidal volume, which would lead to a significant blurring of the image due to this non-point source geometry if imaging did depend on the point of creation. The velocity map imaging spectrometer consists of 3 electrostatic plates with circular apertures; repeller, extractor and ground plate. The ratio between the repeller and extractor voltage has to be chosen correctly in order to ensure sharp velocity focussing. Experimentally the focussing of the electrostatic lens is checked by looking at the spot created by an ion without initial kinetic energy, such as a molecular parent ion. Focussing of the electrostatic lens is obtained for the minimum spot size on the detector.

By varying the voltages of the repeller and the extractor but keeping the ratio constant one can vary the strength of the extraction field.

The flight length from the interaction region to the detector is ~ 25 cm (for both vacuum chamber systems). Since all ions of the same charge experience the same force from the electrostatic field the acceleration and therefore the velocity of the ion during the flight to the detector, depends on their mass alone. In this way the electrostatic lens also serves as a time-of-flight (TOF) mass spectrometer, separating the different ion fragments temporally, as the arrival time of the ion is proportional to the square root of the mass-to-charge ratio, $\text{TOF} \propto \sqrt{m/q}$.

The spectrometer is caged in a μ -metal shield. These cylinders of metal with high magnetic permeability provide a shield against background magnetic fields in the time-of-flight region, from the interaction region to the detector. The heavy ions are unaffected by these stray magnetic field, and the μ -metal cylinders are mainly implemented in the vacuum chamber for the experiment on electron detection.

3.2.4 The Detection System

The detector consists of a 50 mm diameter (active diameter ~ 41.5 mm) micro-channel plate (El-Mul Technologies, Ltd., chevron MCP, B050V) backed by a phosphor screen (El-Mul Technologies, Ltd., ScintiMaxTM P47) of similar size. When an energetic particle, an electron or an ion, impacts the front of the detector it kicks off electrons. When a sufficiently high voltage difference is applied between the front and the back of the MCP, these electrons are accelerated towards the back, building up signal with each additional impact to the channel walls, and hereby creating an electron avalanche. The many micron-size diame-

ter channels in the MCP guide the electron pulses created from each hit through the material without changing the transverse direction, i.e. the position from which the electrons leaves the MCP corresponds to the point where it was initially hit. The electrons leave the MCP and are accelerated towards the phosphor screen if the potential difference between the backside of the MCP and the phosphor screen is sufficiently high. When the electron pulse impacts the phosphor screen it excites the phosphor creating localized spots which subsequently emits a flash of light. These phosphorescent blobs, visible to the naked eye, are then recorded by a charge coupled device (CCD) camera (Allied Vision Technologies, Marlin F-046 (Max. 52 Hz) and Pike F-032 (Max. 208 Hz)), outside of the vacuum chamber. The detector can be gated by applying a fast high-voltage pulse to the front of the MCP only at the arrival time of the ion-fragment of interest. In this way the detector only has sufficient gain to produce a electron pulse in the time interval of interest. The detector can be gated with a time resolution of ~ 90 ns, which allows for mass selective detection of individual fragments.

The spectrometer, as discussed previously, separates the ions temporally according to mass, and time-of-flight measurements can be conducted using the MCP as a fast high gain amplifier. Using a fast oscilloscope it is possible to measure the rapid voltage changes induced by the ion fragments hitting the detector, and the ion yield as a function of flight time is recorded.

3.2.5 Data Acquisition and Processing

Each image from the CCD camera is immediately transferred to the computer. In a data acquisition program (developed by Simon S. Viftrup and later upgraded by Jens Hedegaard Nielsen) each blob is identified and its center coordinates are calculated and stored on a shot-to-shot basis. The identification of the center position ensures that all ion hits are counted with the same weight regardless of the blob size, which may vary due to the non-uniform sensitivity of the detector. This also ensures higher resolution; in principle even sub-pixel resolution is obtained. Several approaches are taken to reduce noise in the images. First of all the phosphorescent blobs only appear on the detector for a very short time, therefore the exposure time of the camera is set to the lowest possible value, 25 μ s. Second a threshold is applied to the camera gain; in this way the gain is kept at a level where the blobs are just big enough for the center to be determined precisely without saturating the CCD. Furthermore the ellipticity of each blob is calculated and very asymmetric blobs are considered double blobs (two blobs hitting the detector too close to be separated within the camera resolution) and its center is counted twice.

From the stored blob positions angular and radial distributions can be calculated and by assuming a Gauss shape of each blob an ion image can be con-

structured. It is important to keep in mind that the ions are projected onto a 2D detector, hence the ion image is a two dimensional projection and thus only contains information about the ion velocity in the detector plane. From the angular distribution one can extract a qualitative measure of the degree of alignment in the form of $\langle \cos^2 \theta_{2D} \rangle$, where θ_{2D} is the angle with respect to the vertical axis in the image. In our data analysis program one can specify the radial region from which $\langle \cos^2 \theta_{2D} \rangle$ is calculated, in this way it is possible to determine the qualitative alignment degree of at specific kinetic energy channel.

Furthermore it is important to notice that the measured value of $\langle \cos^2 \theta_{2D} \rangle$ not only contains information about the two-dimensional angular distribution of the molecule, but also depends on the angular selectivity of the probe with respect to the molecule in question.

Unless certain assumptions can be made about the initial 3D distribution, the value of $\langle \cos^2 \theta_{2D} \rangle$ can not be directly transferred to $\langle \cos^2 \theta \rangle$, and the two expectation values should not be confused. In general $\langle \cos^2 \theta_{2D} \rangle$ provides a good qualitative measure.

3.2.6 Timing

The entire data acquisition system is synchronized to the repetition rate of the femtosecond laser. The Synchronization and Delay Generator (SDG) controlling the timing necessary for the Spitfire regenerative amplifier to operate, provides a master trigger signal of 1 kHz, which is send to a Stanford Research Systems Delay Generator (SRS DG535), from which all necessary delays are generated digitally. The SRS lowers the repetition rate down to match the maximum repetition rate of the data acquisition system, with the limiting factor being the computational time during center determination of the blobs. Experiments involving the nanosecond laser were conducted at 20 Hz limited by the repetition rate of the laser system. The SRS controls the timing of the trigger pulses to the various elements in the setup: the valve, the high voltage gate on the MCP, the camera and the Q-switch of the nanosecond laser.

4

ELECTROSTATIC DEFLECTION OF COLD MOLECULAR BEAMS

4.1 Introduction

For a large range of experiments in chemistry and physics, a high level of control over the external and internal degrees of freedom of molecules would be very beneficial. This includes control over the translational and the rotational motions, as well as the selection of a single quantum state or a small subset of states. Such quantum-state-selected targets provide unique possibilities, for example, for manipulating the external degrees of freedom with static electric fields [5, 86] or optical fields [7, 52], or both [24, 25]. The quantum-state selection also naturally discriminates between individual stereo-isomers of large molecules [87]. The resulting samples of aligned or oriented individual isomers offer unique prospects for novel experiments with complex molecules, such as femtosecond pump-probe measurements, X-ray or electron diffraction in the gas-phase [47, 48], high-harmonic generation [88] or tomographic reconstructions of molecular orbitals [38]. Moreover, it would provide considerably increased control in reaction dynamics experiments [3, 4, 89].

Strong cooling can be achieved in supersonic expansions of molecules seeded in an inert atomic carrier gas. For small molecules (consisting of just a few

atoms) only a few rotational states are populated at the typical temperatures on the order of 1 K. For larger polyatomic systems rotational cooling down to or even below 1 K still leaves the molecular ensemble distributed over a considerable range of rotational states, thereby often masking quantum state specific effects. State selection can be performed using inhomogeneous electric or magnetic fields. The interaction of the dipole moment with an external field is known as the Stark effect. The Stark effect can be used to manipulate molecules, with the resulting force depending on orientation of the dipole with respect to the electric field. In a purely classical description the force on a molecule in an inhomogeneous electric field is given by the negative gradient of the Stark potential energy

$$\mathbf{F}(\mathbf{r}) = -\nabla V_{\text{Stark}}(\mathbf{E}) \quad (4.1)$$

For a molecule with a linear Stark shift the potential energy depends on the magnitude of the electric field, E

$$V_{\text{Stark}} = -\mu_{\text{eff}}(E)E \quad (4.2)$$

where $\mu_{\text{eff}}(E)$ is the effective dipole moment, which is an inherent property of the quantum state. The possibility to deflect polar molecules in a molecular beam with an electric field was first described by Kallmann and Reiche in 1921 [90] and experimentally demonstrated by Wrede in 1927 [91]. As early as 1926, Stern suggested that the technique could be used for the quantum state separation of small diatomic molecules at low temperatures [92]. In 1939 Rabi *et al.* [93] introduced the molecular beam resonance method, by using two deflection elements of oppositely directed gradients in succession, to study the quantum structure of atoms and molecules. Whereas deflection experiments allow the spatial dispersion of quantum states, they do not provide any focusing. For small molecules in low-field-seeking states this issue could be resolved using multipole focusers with static electric fields. These were developed independently in 1954/55 in Bonn [94, 95] and in New York, where they were used to produce the population inversion for the first MASER experiments [96, 97]. About ten years later, molecular samples in a single rotational state were used for state specific inelastic scattering experiments by the Bonn group [98] and, shortly thereafter, for reactive scattering [99, 100]. In the following decades, multipole focusers were extensively used to study steric effects in gas-phase reactive scattering experiments [3]. Also for the investigation of steric effects in gas-surface scattering experiments [101] and photodissociation [102], the preparation of oriented samples of state-selected molecules using electrostatic focusers was essential. For the last decade, it is also possible to manipulate the speed of small molecules using switched inhomogeneous electric fields in the so-called Stark decelerator [103]. More recently, also the optical [104] and magnetic [105] analogs have been demonstrated.

Obtaining similar control over large molecules is more difficult, because all low-lying quantum states are high-field seeking at the required electric field strengths. In order to confine these molecules, dynamic focusing schemes are necessary [106–108]. Dynamic focusing of large molecules has been demonstrated in the alternating-gradient (AG) deceleration of benzonitrile [109] and in the conformer selection of 3-aminophenol [87]. However, if focusing is not necessary, spatial dispersion of quantum states can still be achieved using static electric fields in a Stern-Gerlach-type deflector. This molecular beam deflection has been used extensively as a tool to determine dipole moments and polarizabilities of molecular systems ranging from diatomics [91] over clusters [110] to large biomolecules [111].

In this chapter quantum-state selection of large molecules will be demonstrated, following the original proposal of Stern [92]. A detailed analysis of electrostatic beam deflection is presented. It is shown, how the rotational temperature of cold supersonic jets can be determined with high precision from deflection measurements and that indeed a small subset of quantum states can be addressed in deflected samples of large molecules. In particular, the ground state has the largest Stark shift and molecules residing in this state are deflected the most. Our goal is to isolate and use rotational ground state molecules, or at least samples of molecules in the few lowest lying states, as targets for various experiments. Since the deflection does not change the initial state distribution but merely disperses it, it is crucial that the population of ground state molecules in the molecular beam is initially as large as possible. Therefore, the rotational temperature of the molecular beam is made as low as possible using a high-pressure supersonic expansion [81]. In the following chapters it is shown how the resulting state-selected molecules can be used to improve laser-induced alignment and mixed field orientation.

The design and construction of the electrostatic beam deflector was made by our collaborators, Frank Filsinger, Jochen Küpper and Gerard Meijer at the Fritz Haber Institut der Max Planck Gesellschaft in Berlin. The simulations presented in this chapter have all been performed by Frank Filsinger.

4.2 Experimental

The experimental setup was described in details in Chapter 3. In brief about 3 mbar of iodobenzene (Sigma Aldrich, 98% purity) or benzonitrile (Sigma Aldrich, 98% purity) is seeded in an inert carrier gas and expanded through a pulsed valve into vacuum. In order to obtain optimal cooling of the molecular beam we use our miniaturized, high pressure Even-Lavie valve [81] operating at a backing pressure of 90 bar of He or 25-30 bar of Ne limited by the onset

of cluster formation. The molecular beam is first skimmed twice before entering the electrostatic beam deflector. The gradient of the electric field along the vertical direction is large and nearly constant over a large area explored by the molecular beam, while the electric field is very homogeneous along the horizontal direction. Thus, a polar molecule experiences a nearly constant force in the vertical direction independent of its position within the deflector, while the force in the horizontal direction (i. e. broadening of the beam in the horizontal direction) is minimized. In our setup, the deflector is mounted such that molecules in high-field-seeking (low-field-seeking) quantum states are deflected upwards (downwards). After passing through the deflector, the molecular beam enters the differentially pumped detection chamber via a third skimmer of 1.5 mm diameter. In the detection area, the molecular beam is crossed by the probe laser beam focused by a spherical lens with a focal length of $f = 300$ mm. The lens is mounted on a vertical translation stage so that the height of the laser foci can be adjusted with high precision. To characterize the beam deflection the probe beam (30 fs (FWHM) pulses, 800 nm, beam-waist $\omega_0 = 21$ μm) is used to determine the density in the molecular beam via photoionization.

4.3 Results and Discussion

In the first experiment, the deflection of benzonitrile molecules (BN, $\text{C}_7\text{H}_5\text{N}$) seeded in 90 bar of He is investigated. BN is an ideal candidate for electrostatic beam deflection due to its large permanent dipole moment of 4.515 D. From the precisely known molecular constants [112] the Stark curves (potential energy) of a given rotational quantum state can be calculated as a function of the electric field strength. For details of the exact procedure the reader is referred to [113]. Figure 4.1 shows the Stark energies for the lowest rotational states of BN. Due to the small rotational constants and the resulting high density of rotational states, a large number of states is populated even under the cold conditions in a supersonic expansion. At a rotational temperature of 1 K, the typical temperature in our experiments (vide infra), 66 rotational quantum states (with 419 M -components) have a population larger than 1% relative to the ground state. At the electric field strengths present in the deflector, indicated by the shaded area in Fig. 4.1, all low-lying quantum states are high-field seeking. This is due to mixing of closely spaced states of the same symmetry and typical for large asymmetric top molecules. The Stark shift and thus the force a molecule experiences in an inhomogeneous electric field depends on the rotational quantum state. Molecules in the ground state have the largest Stark shift and are, therefore, deflected the most. In general, the Stark shift decreases with increasing J quantum number. Thus, the lower the rotational temperature of the molecular

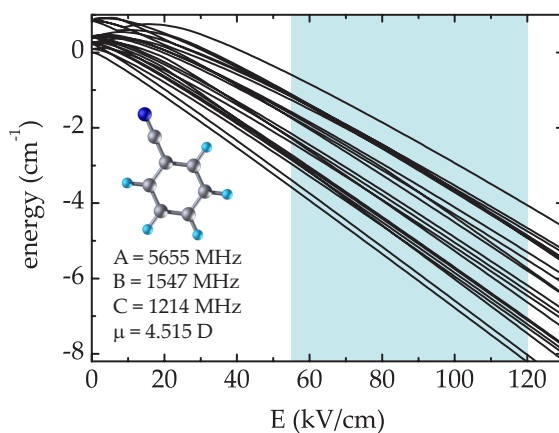


Figure 4.1: Potential energy as a function of the electric field strength for the lowest rotational quantum states of benzonitrile. The shaded area indicates the actual electric field strength inside the deflector. In the inset, the molecular structure is shown together with the relevant molecular constants [112].

beam is, the more the beam is deflected.

Figure 4.2 shows vertical intensity profiles of BN for various high voltages applied to the deflector. Vertical intensity profiles are obtained by recording the BN^+ signal from photoionization by the fs-laser as a function of the vertical position of the laser focus. If no high-voltage is applied to the deflector, the molecular beam extends over about ~ 2 mm. In this case, the size of the molecular beam in the detection region is determined by the mechanical aperture of the experimental setup, i. e. by the dimensions of the deflector and the last skimmer before the detection region. As the high voltage is turned on, the molecular beam profile broadens and shifts upwards. At a voltage of 10 kV, a large fraction of the molecules is deflected out of the original, undeflected beam profile. A small fraction of the molecules, however, is almost unaffected by the deflector.

In order to understand these experimental findings, Monte Carlo simulations have been employed. For details the reader is referred to [113]. In brief, trajectory calculations are performed for molecular packets of individual rotational quantum states. These calculations yield single-quantumstate deflection profiles. Then, the single-state profiles are averaged according to the populations of the respective states in the original molecular beam (i. e. at the entrance of the deflector). From these simulations, it is obvious that the molecules in the original beam are not rotationally thermalized, an effect that has previously been

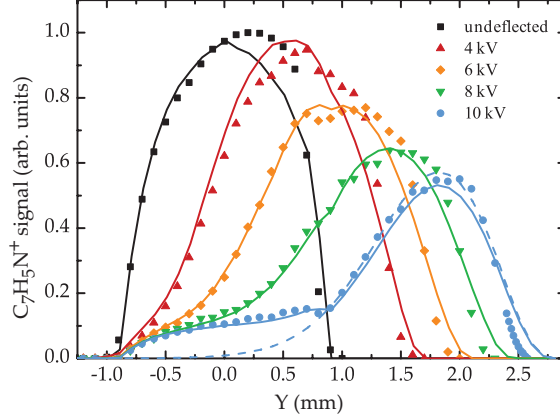


Figure 4.2: The vertical spatial profile of the molecular beam measured by recording the laser induced BN^+ signal (see text). The experimental data are shown together with the corresponding simulated profiles.

observed in rotationally resolved spectroscopy [114, 115]. A number of different descriptions of the populations of rotational states has been given [115]; we use the formula for a two-temperature model originally proposed by Wu and Levy [114]. Finally, the rotational temperature of the low-temperature component in the molecular beam is obtained by fitting the simulated deflection profiles to the experimental data using a local optimization algorithm. All deflection profiles measured at the different voltages are fitted simultaneously, where the fraction w of the low-temperature component, a general intensity scaling factor s between undeflected and deflected profiles, and the rotational temperature T_{rot} of the low-temperature component are the fitting parameters. Best agreement between experimental data and simulations is found for $q = 0.93$ and $T_{\text{rot}} = 0.8$ K. The resulting simulated deflection profiles nicely reproduce the experimental data as shown in Fig. 4.2 (solid lines). In particular, the undeflected part of the molecular beam for 10 kV can be perfectly simulated, which indicates, that the use of a two-temperature model was indeed justified. For comparison, also a simulated deflection profile for 10 kV using a one-temperature model is shown (dashed line in Fig. 4.2).

In order to estimate the uncertainty of T_{rot} , deflection profiles are calculated for different rotational temperatures. For each fixed rotational temperature, the best values for s and q are determined using the fitting procedure outlined above and the resulting deflection profile for a voltage of 10 kV is plotted in Fig. 4.3. With increasing T_{rot} , the peak of the beam profile shifts towards smaller

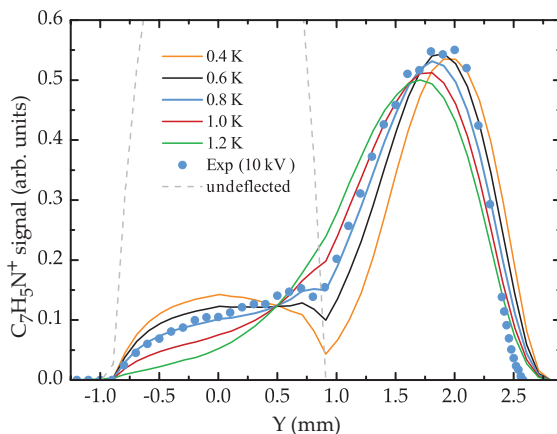


Figure 4.3: The vertical profile of the molecular beam measured by recording the laser induced BN^+ signal (see text). The experimental data are shown together with the corresponding simulated profiles for different rotational temperatures. Simulations are shown for the two-temperature model; see text for details.

y-values, while, at the same time, the intensity in the undeflected part of the beam profile is reduced. From the comparison of experimental data and simulation, an uncertainty of T_{rot} of ± 0.2 K is estimated.

The deflection of iodobenzene molecules (IB, $\text{C}_6\text{H}_5\text{I}$) is investigated in the same way. Vertical intensity profiles are measured by recording the signal of I^+ ions, created by Coulomb explosion with a circularly polarized probe pulse, as a function of the vertical position of the probe laser focus. Figure 4.4 a) shows deflection measurements for IB seeded in 90 bar of He. IB (mass 204 u) is heavier than BN (mass 103 u) and has a considerably smaller dipole moment of only 1.625 D [116] compared to BN. Therefore, smaller deflections are observed for IB (see Fig. 4.2) under identical expansion conditions. However, the interaction time with the electric field and the time-of-flight from deflector to detection region can be increased when Ne is used as a carrier gas instead of He. Changing the carrier gas reduces the mean velocity of the molecular beam from 1800 m/s to 800 m/s and significantly enhances the observed deflection as shown in Fig. 4.4 b). Following the fitting procedure outlined above, T_{rot} can be determined for IB as well. In the case of IB, a one-temperature model with a rotational temperature of 1.05 K fits the experimental data best for the deflection measurements both in He and Ne. The uncertainty of T_{rot} is estimated to be ± 0.1 K for IB seeded in Ne and ± 0.2 K for IB in He. The somewhat larger un-

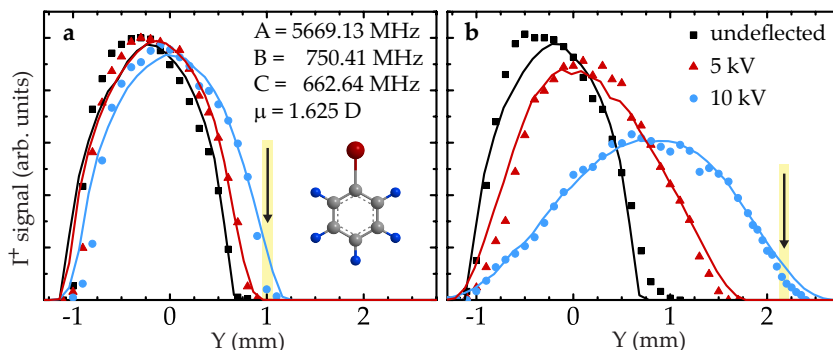


Figure 4.4: The vertical profile of the molecular beam measured by recording the laser induced I^+ signal (see text). The experimental data are shown together with the corresponding simulated profiles. Figure (a) shows the beam profiles for a He beam, Figure (b) shows the respective profiles for a Ne beam. Arrows indicate the laser positions for alignment and orientation experiments (vide infra).

certainty for the measurements in He reflects the small deflections observed for He. The simulated deflection profiles for IB are shown as solid lines in Fig. 4.4 and agree well with the experimental data .

The main purpose of the deflection studies presented in this work is to provide quantum-state-selected samples of large molecules for further experiments. The degree of deflection that a molecule experiences in the electric field of the deflector depends on its quantum state. The relevant quantity is the effective dipole moment μ_{eff} (the negative slope of the Stark curve), which depends on the electric field strength. Molecules residing in low rotational quantum states have generally the largest μ_{eff} and are, therefore, deflected most. These molecules can simply be addressed by moving the laser focus in the detection region towards the upper cut-off of the molecular beam profile. In order to understand the laser-induced alignment and orientation experiments presented in sections 5.4.1 and 5.4.2, it is crucial to know the relative populations of individual quantum states that are probed at a given height of the laser focus. The position of the laser focus within the molecular beam profile during the alignment and orientation measurements is indicated by an arrow in Fig. 4.4 b. At this position, the intensity of the deflected beam is 9% of the undeflected peak intensity. The composition of the molecular packets in the detection region can be extracted from the simulated deflection profiles. Table 4.1 provides an overview of the most abundant quantum states present in different regions of the beam profiles for IB at a rotational temperature of 1.05 K. For comparison, also the population of each

rotational quantum state in the undeflected beam for this rotational temperature is given. At the position of the laser focus for the orientation experiments (last column in table 4.1), the population of the lowest quantum states is significantly enhanced compared to the undeflected beam. The fraction of ground state molecules is enhanced by a factor of five, for instance. About 97% of the population resides in the few quantum states listed in table 4.1 with the $J_{K_a K_c} = 3_{03}$ state being most abundant. Moving the laser focus even closer towards the upper cut-off in the beam profile should reduce the number of quantum states that are probed even further. If a reduction of the beam intensity by two orders of magnitude can be afforded, only 4 quantum states are predicted to be probed with 37% of the molecules being in the $J_{K_a K_c} = 3_{03}$ state. At first glance, it is surprising that this state and not the absolute ground state, which is expected to have the largest μ_{eff} , is populated most in the deflected beam. In order to understand this, the Stark curves for the most deflected quantum states of IB are shown in Fig. 4.5 a, together with their effective dipole moments (Fig. 4.5 b). Below the relevant electric field strengths, both the $J_{K_a K_c} M = 3_{03}2$ and the $J_{K_a K_c} M = 4_{13}3$ M -sublevels have avoided crossings with close-by states of the same symmetry (dashed lines in Fig. 4.5 a). These avoided crossings lead to large local effective dipole moments that are comparable to the ground-state μ_{eff} . Thus molecules in these quantum states are deflected as much as ground-state molecules. Furthermore, states with $M \neq 0$ are doubly degenerate, whereas the ground state with $M = 0$ is only singly degenerate. Therefore, the population of molecules in the $J_{K_a K_c} M = 3_{03}2$ to begin with, i. e. in the undeflected beam, is even larger than the population in the ground state. From table 4.1 it is clear, that it will be difficult to isolate the rotational ground state of iodobenzene in our setup. Nevertheless, if the fraction of ground-state molecules could be increased from 1% in the undeflected to 26% in the deflected beam, dramatic effects are to be expected for a variety of further experiments.

We point out that we are assuming adiabatic following of potential energy curves in all simulations. Nonadiabatic transitions are unlikely in the strong fields inside the deflector, since the number of avoided crossings and their energy gaps generally increase with electric field strength. Moreover, the probability for nonadiabatic following depends on the rate of change of the field strength, which is only due to the slow translational motion of the molecules. However, nonadiabatic transitions have been observed in different Starkdecelerator beamlines at real [117] and avoided crossings [118] for small electric fields. Similarly, when the deflected molecules in the experiments reported here enter

On the other hand, the local effective dipole moments of the neighboring states (dashed lines in Fig. 4.5 a) are reduced by these crossings. At an avoided crossing, the two levels that are involved "exchange" their effective dipole moments. For large asymmetric top molecules, many avoided crossings can lead to a complicated shape of the adiabatic Stark curve and a strongly varying effective dipole moment with the electric field strength.

$J_{K_a K_c} M$	IB in He at $0.01 \cdot I_{\text{peak}}$		IB in Ne at $0.01 \cdot I_{\text{peak}}$		IB in Ne at $0.09 \cdot I_{\text{peak}}$		undeflected beam $P_{J_{K_a K_c}}^{\text{free}}$ (%)	
	P_M (%)	ΣP_M (%)	P_M (%)	ΣP_M (%)	P_M (%)	ΣP_M (%)		
0 ₀₀ 0	17.51	17.51	26.06	26.06	6.24	6.24	1.15	
1 ₀₁	0	0.02			3.90	13.61	3.24	
	1	7.69			7.71			9.70
1 ₁₁	0	1.92	23.84	23.84	2.37	7.79	1.55	
	1	15.66			17.58			5.43
1 ₁₀	0	1.81			2.41	6.26	1.55	
	1	0.02			1.82			3.86
2 ₀₂	1				0.57	7.74	4.75	
	2				7.17			
2 ₁₂	0				0.23	7.90	2.28	
	1				3.51			
	2	3.22			3.22			4.16
3 ₀₃	0	0.01	36.61	36.61	2.93	19.00	5.47	
	1	6.17			29.73			7.17
	2	23.55			36.61			8.01
	3				0.89			
3 ₁₃	2				0.20	2.98	2.65	
	3				2.79			
4 ₀₄	0	0.01			2.12	7.68	5.43	
	3	3.98			3.99			5.56
4 ₁₃	1		13.49	13.49	2.12	7.58	2.54	
	2	2.17			10.52			2.60
	3	8.35			10.52			2.87
5 ₀₅	1				0.19	6.73	4.80	
	2				3.24			
	4				3.30			
5 ₁₄	0				0.08	1.90	2.22	
	4	1.66			1.66			1.83
5 ₂₃	3	0.06					1.92	
	4	5.61			5.67			
6 ₁₆	2				0.19	1.26	1.91	
	3				1.07			
Σ		99.41		100.00		96.67	41.46	

Table 4.1: Relative population of individual quantum states in the deflected part of the molecular beam profile for $T_{\text{rot}} = 1.05K$. Left: IB in He at 1 % of peak intensity of undeflected beam. Center: IB in Ne at 1 % of peak intensity of undeflected beam. Right: IB in Ne at 9 % of peak intensity of undeflected beam (here orientation images were taken). P_M denotes relative population of individual M-sublevels in %, $P_{J_{K_a K_c}}$ the sum over all M-sublevels, and $P_{J_{K_a K_c}}^{\text{free}}$ the relative population of a given rotational quantum state in a free jet.

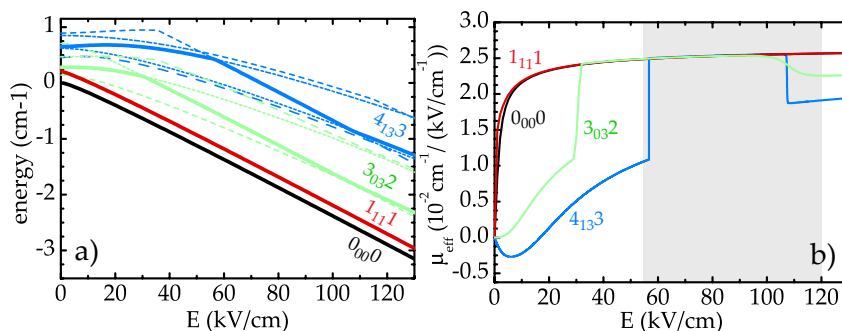


Figure 4.5: (a) Potential energy as a function of the electric field strength for selected quantum states of IB. Solid lines represent quantum states that are present close to the upper cut-off of the molecular beam profile for IB seeded in Ne. The respective $J_{K_a K_c}$ quantum numbers are given in the figure. (b) Effective dipole moment for selected quantum states of IB. The shaded area represents the range of electric field strengths in the deflector at 10 kV.

a field-free region, scrambling of population over the various M components of their rotational state will occur. For small molecules, like OCS or ClCN, the preparation of an ensemble of molecules, all in a single quantum state will be feasible with the present setup. For these systems, the number of quantum states that are populated in a supersonic jet is significantly smaller compared to large asymmetric top molecules like IB or BN. The spacing between neighboring quantum states is larger and the number of avoided crossings smaller. Thus, the differences in the effective dipole moment between individual quantum states are larger and, therefore, the degrees of their deflection will vary considerably.

5

LASER INDUCED 1D ALIGNMENT AND ORIENTATION

5.1 Introduction

Any application of aligned or oriented molecules will benefit significantly from, or simply requires, a strong degree of alignment or orientation. One efficient method to optimize the degree of alignment or orientation is to ensure that the molecular sample initially resides in the lowest-lying rotational states. This is achieved by lowering the rotational temperature as much as possible. In practice, strong cooling can be obtained by supersonically expanding a small fraction of the molecular gas of interest in an inert carrier gas. Very strong degrees of alignment have been reported using molecular beams with a rotational temperature around 1 K [60]. However, optimizing the degree of orientation in the mixed laser and static electric field method imposes an even stronger requirement on the initial rotational state distribution.

In this chapter it is shown how laser-induced 1D alignment and mixed field orientation, can be strongly enhanced using rotational quantum-state-selected molecules. The state selection is obtained by passing a cold molecular beam through an electrostatic deflector that spatially disperses molecules according to their rotational quantum state as described in the previous chapter. Here,

alignment and orientation occurs in the adiabatic limit where the laser pulse duration is much longer than the inherent rotational periods of the molecule [15, 56]. The state selection leads to strong enhancement in the degree of orientation and alignment of carbonylsulfide (OCS) and iodobenzene (IB) molecules compared to that achieved when no deflection is used.

5.2 Experimental Setup

A gas mixture of ~ 10 mbar carbonylsulfide (OCS) and 10 bar of Ne or 3 mbar of iodobenzene (Sigma Aldrich, 98% purity) and 90 bar of He or 20 bar of Ne (limited by the onset of cluster formation) is expanded supersonically into vacuum through our Even-Lavie valve forming a pulsed molecular beam. The molecular beam is skimmed twice and enters a 15-cm-long electrostatic deflector that spatially disperses the molecular beam in the vertical direction according to the initial rotational states as described in Chapter 4. After passing through the deflector, the iodobenzene molecules enter the differentially pumped detection chamber via a third skimmer of 1.5 mm diameter. The experiments involving OCS were performed after the vacuum chamber system had been upgraded, hence after exiting the deflector the OCS molecules pass through a homogeneous field from the capacitor plates ensuring no mixing of the M -states. In the experiments the capacitor-plates were kept at a potential of 500 V.

In the detection chamber the molecular beam is crossed at 90° by two focused laser beams. The lens is mounted on a vertical translation stage so that the height of the laser foci can be adjusted with high precision. The target of adiabatically aligned and oriented molecules is prepared by the combined action of a 10 nanosecond long laser pulse and the weak static electric field already used to project ions or electrons onto the 2-dimensional particle detector. The 10 ns (FWHM) long pulses from a Nd:YAG laser (1064 nm, $\omega_0 = 36 \mu\text{m}$) are overlapped in time and space with the 30 fs probe laser pulses ($\lambda = 800$ nm, $\omega_0 = 21 \mu\text{m}$). The probe pulses are used to Coulomb explode the molecules and subsequently the recoil directions of the ionic fragments are recorded. In the case of the linear OCS molecules S^+ ions are recorded to determine the molecular axis orientation. For iodobenzene molecules I^+ ions are recorded to determine the orientation of the symmetry axis of the molecule. 2D ion images of S^+ and I^+ recorded with a CCD camera provide direct information about the instantaneous molecular orientation of the OCS and C-I bond axis, respectively, with respect to the laboratory frame and are therefore the basic observables in these experiments. All experiments are conducted at 20 Hz, limited by the repetition rate of the YAG laser. The experiments described here are conducted on undeflected molecules compared to the most deflected molecules, i. e. a subset

of molecules selected in the lowest lying rotational quantum states.

5.3 Laser-Induced Alignment and Orientation of a Linear Molecules

In this section the linear molecule carbonylsulfide (OCS) is studied. OCS has a dipole moment of 0.71 D and polarizabilities $\alpha_{\parallel} = 7.516 \text{ \AA}^3$ and $\alpha_{\perp} = 3.875 \text{ \AA}^3$. The For a linear molecule alignment and orientation of the mayor polarizability axis and dipole moment is sufficient to achieve full orientational control over the molecule.

5.3.1 Deflection of the Molecular Beam

Initially the effect of the electrostatic beam deflector is characterized for OCS seeded in Ne. Figure 5.1 shows the vertical intensity profile of OCS for various high voltages applied to the deflector. The vertical spatial profiles are obtained by recording the OCS⁺ signal from photoionization by the femtosecond laser as a function of the vertical position of the laser focus. Compared to the vertical intensity profiles obtained for iodobenzene and benzonitrile, described in the previous chapter, the molecular beam with no voltage applied to the deflector extends over about ~ 2.5 mm instead of 2 mm. The reason for the change in the molecular beam size is that the experiments on OCS were performed after the upgrade of the molecular beam apparatus, i. e. with the first skimmer changed from 1 mm to 3 mm and the final skimmer replaced by a set of capacitor plates. The modifications, thus, broadened the molecular beam. Again as the high voltage is turned on, the molecular beam profile broadens and shift upwards. When 9 kV are applied to the detector the cutoff seems to end quite abruptly, indicating that the molecular beam is hitting the edges of the deflector or other components in the vacuum chamber. For that reason a maximum of 7 kV is applied in the following studies.

5.3.2 Laser-Induced Alignment

Next, alignment induced by the YAG pulse is studied. The basic experimental observables are 2-dimensional (2D) S⁺ ion images from Coulomb explosion of the OCS molecules. The geometry of the laser pulse polarizations with respect to the velocity map imaging (VMI) spectrometer is illustrated in Fig. 5.2. The YAG pulse is linearly polarized along the vertical direction (laboratory fixed Y-axis), hence parallel to the detector plane. The Coulomb explosion probe is linearly polarized perpendicular to the detector plane (laboratory fixed Z-axis).

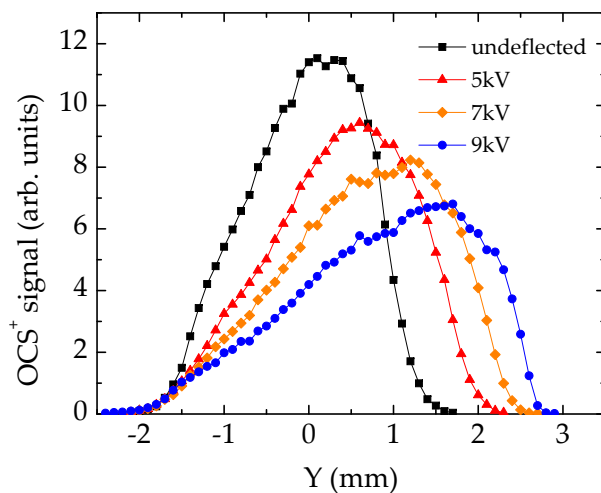


Figure 5.1: Experimentally measured vertical spatial profile of the molecular beam of carbonylsulfide for different deflection voltages applied, measured by recording the OCS^+ signal.

This ensures that there is no detection bias on the molecular orientation in that plan.

Figure 5.3a shows a S^+ ion image obtained from the probe pulse only. The image is circularly symmetric as to be expected from a random oriented ensemble of molecules in the present probe geometry. When the YAG pulse is included (Fig. 5.3, image b), the S^+ image exhibits strong angular confinement along the polarization of the YAG pulse. The S^+ ions appear in a radially localized region corresponding to a fragmentation channel of the Coulomb explosion. The channel is ascribed to the OCS molecules being doubly ionized by the probe pulse, resulting in fragmentation into a $\text{S}^+ + \text{OC}^+$ ion pair. In the images the central region has been cut away. OCS has an ionization potential of 11.4 eV and is very hard to Coulomb explode even with the intensities applied here, as a consequence the overall S^+ signal is very weak compared to the molecular ion. A large fraction of the S^+ ions are thus created from single ionization of OCS, through the $\text{S}^+ + \text{OC}$ fragmentation channel. S^+ ions leaving a neutrally charged carbonyl group have lower kinetic energy than those from the Coulomb explosion channel and will end up in the central part of the detector. Furthermore, S^+ has the same mass to charge ratio as O_2^+ and a large fraction of the ion hits

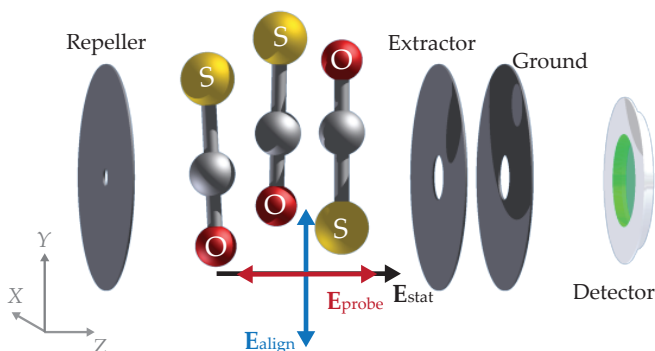


Figure 5.2: Schematic illustration of the polarization state of the YAG and the probe pulse with respect to the static electric field and the detector plane used to characterize alignment, including a sketch of the resulting molecular alignment. Repeller, extractor and ground refers to the electrostatic plates of the VMI spectrometer.

in the central region originate from ionization of O_2 background gas present in the target chamber. This has been verified experimentally by blocking the molecular beam. The pronounced angular confinement observed in images b and c is quantified by calculating the expectation value of $\langle \cos^2 \theta_{2D} \rangle$, where θ_{2D} is the angle between the YAG pulse polarization and the projection of the S^+ recoil velocity vector onto the detector plane. For OCS, $\langle \cos^2 \theta_{2D} \rangle$ values are calculated only from ions detected in the radial region corresponding to the $S^+ + OC^+$ fragmentation channel. It should be noted that $\langle \cos^2 \theta_{2D} \rangle = 0.50$ would correspond to perfectly randomly oriented molecules, whereas $\langle \cos^2 \theta_{2D} \rangle = 1$ would correspond to the quantum mechanically unfeasible situation of perfectly 1D-aligned molecules. Image a is recorded with only the probe laser present. This should correspond to a target of randomly oriented molecules. As expected in the chosen probe geometry the image is circularly symmetric and $\langle \cos^2 \theta_{2D} \rangle = 0.512$. When the YAG pulse is included (image b) a pronounced angular confinement is observed along the polarization of the YAG pulse and $\langle \cos^2 \theta_{2D} \rangle$ is increased to 0.875. These observations are in complete agreement with previous studies [60]. When the deflector is turned on at 7 kV and the laser foci moved towards the edge of the most deflected molecules (at the position corresponding to 2.15 mm of Fig. 5.1), corresponding to molecules in the lowest rotational states, the angular confinement is further enhanced (image c) leading to a $\langle \cos^2 \theta_{2D} \rangle$ value of 0.908. To investigate the influence of the YAG intensity on the molecular alignment, measurements were performed as a function of YAG intensity. In Fig. 5.4 $\langle \cos^2 \theta_{2D} \rangle$ values are plotted as a function of YAG intensity. Again, im-

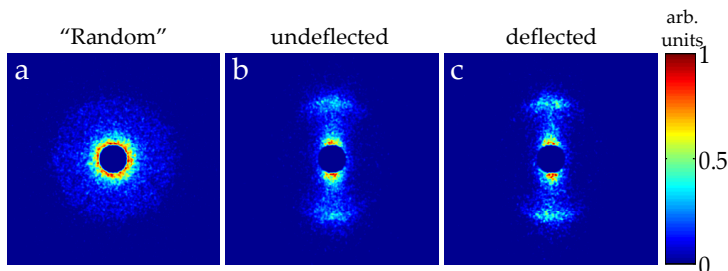


Figure 5.3: S^+ ion images illustrating alignment, recorded when the probe pulse Coulomb explodes the OCS molecules. The polarization of the YAG and the probe pulses are kept fixed at $\beta_{\text{align}} = 90^\circ$ and $\beta_{\text{probe}} = 0^\circ$ of Fig. 5.5. The labels "undeflected" and "deflected" correspond to images recorded at lens position, $Y = 0.0$ with the deflector turned off and $Y = 2.15$ mm with the deflector at 7 kV. The intensities of the YAG and the probe pulse are 1.4×10^{12} W/cm² and 5.4×10^{14} W/cm², respectively. The color scale indicates the relative number of ions and is the same for the subsequent figures of ion images in this chapter.

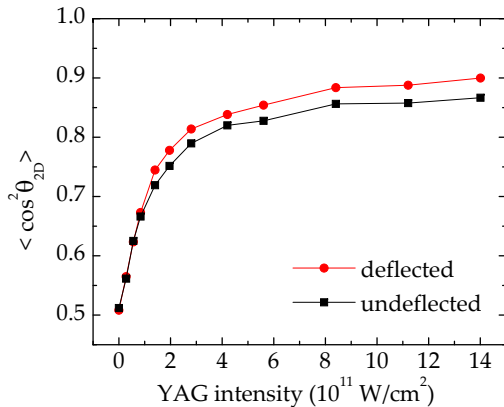


Figure 5.4: Degree of alignment as a function of the YAG intensity for OCS. The labels "undeflected" and "deflected" correspond to images recorded at lens position $Y = 0.0$ with the deflector turned off and $Y = 1.9$ mm with the deflector at 7 kV. The intensity of the probe pulse is 5.4×10^{14} W/cm²

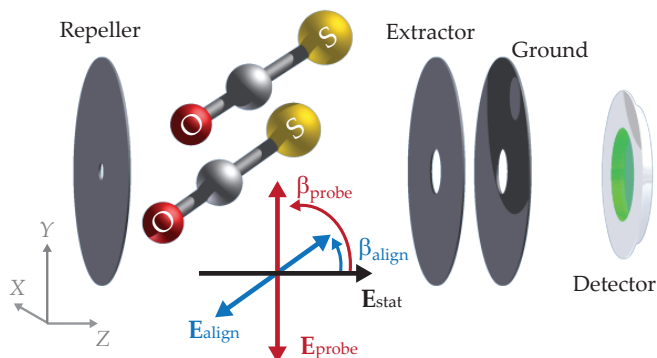


Figure 5.5: Schematic of the velocity map imaging spectrometer used to detect ions. The alignment of the molecules, illustrated by the OCS model, is determined by the alignment laser polarization, here shown for $\beta_{\text{align}} = 45^\circ$. The static electric field of the spectrometer, pointing from the repeller to the extractor electrode for ion detection, breaks the head-for-tail symmetry by preferentially placing the O-end towards the repeller where positive voltage is highest. Repeller, extractor and ground refers to the electrostatic plates of the VMI spectrometer.

improvements are observed when deflected rather than undeflected molecules are employed.

5.3.3 Mixed-Field Orientation

Next, orientation of the OCS molecules due to the combined action of the YAG pulse and the static electric (E_{stat}) from the VMI electrodes is discussed. Figure 5.5 illustrates the polarization state of the YAG and the probe pulse with respect to the static electric field of the VMI electrodes. The important difference compared to the alignment data is that the YAG polarization is rotated away from the axis perpendicular to the static field. Thus, the orientation data result from geometries where the angle β_{align} between the YAG polarization (the molecular bond axis) and the static electric field is different from 90° , see Fig. 5.5. To image orientation the probe pulse is linearly polarized in the vertical direction (laboratory fixed Y -axis), i. e. parallel to the detector. This ensures a clear separation of S^+ from the $S^+ + OC^+$ fragmentation channel. The choice of probe polarization does not secure that any molecule will be ionized, and thus detected, with the same probability independent of β_{align} . In fact, we expect an underestimation of the degree of orientation. Only a circularly polarized probe pulse would fulfill the requirements, however due to the limitations in the field

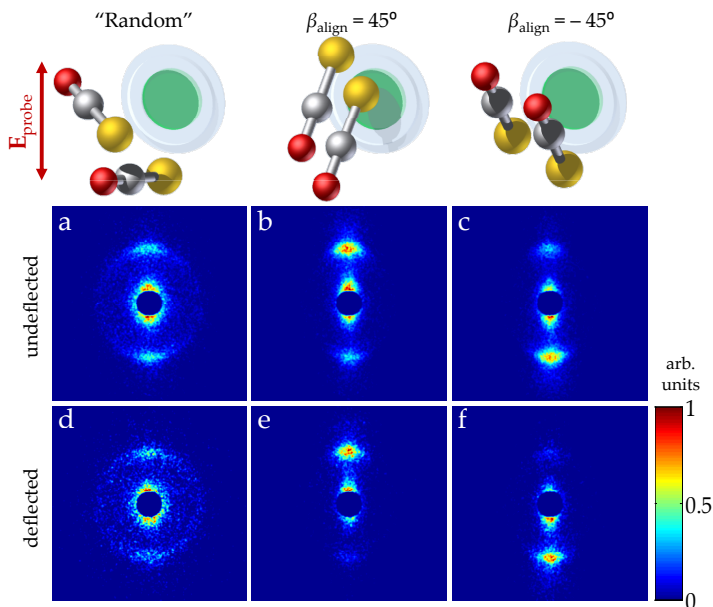


Figure 5.6: S^+ ion images illustrating alignment for $\beta_{\text{align}} = 45^\circ$ and -45° , respectively, recorded when the linearly polarized probe pulse Coulomb explodes the OCS molecules. The probe is polarized parallel to the detector, at $\beta_{\text{probe}} = 90^\circ$. The labels "undeflected" and "deflected" correspond to images recorded at lens position $Y = 0.0$ with the deflector turned off and $Y = 2.15$ mm with the deflector at 7 kV. The intensity of the YAG and probe pulse are 1.4×10^{12} W/cm² and 5.4×10^{14} W/cm², respectively. The static field is $E_{\text{stat}} = 594$ V/cm.

strength of the probe pulse, we were not able to use a circularly polarized probe pulse. The linearly polarized probe will induce some bias on the angular distribution of the S^+ ions (see Fig. 5.6 image a and d), however, importantly, it is up/down symmetric. Figure 5.6 shows S^+ ion images for both deflected and undeflected molecules with the YAG laser at $\beta_{\text{align}} = 45^\circ$ and -45° , respectively, where β_{align} is the angle between the static electric field, E_{stat} , and the alignment laser field, E_{align} . The amplitude of the static field is 594 V/cm. As mentioned, the linearly polarized probe alone gives rise to an image that exhibits some angular confinement, however the images are up/down symmetric. When the YAG pulse is included at $\beta_{\text{align}} = 45^\circ$ or -45° a strong angular confinement of the S^+ shows that the OCS molecules are sharply 1-dimensionally aligned along the polarization of the linearly polarized alignment pulse. In addition, a pronounced asymmetry of the S^+ ions emitted either parallel or anti-parallel to

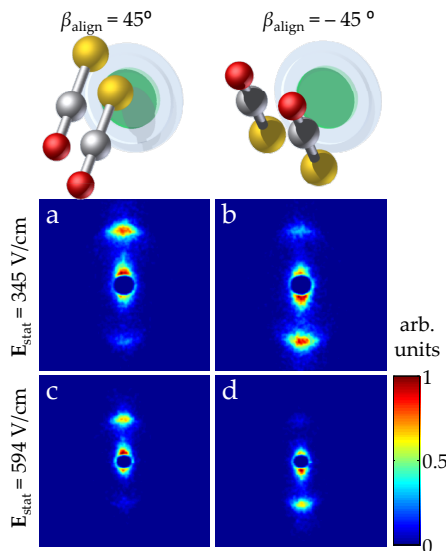


Figure 5.7: a,b S^+ ions images from deflected molecules for $\beta_{\text{align}} = 45^\circ$ and -45° , respectively and $E_{\text{stat}} = 345 \text{ V/cm}$. In a 73 % of all S^+ ions appear in the upper half of the detector. In b 28 % of all S^+ ions appear in the upper half of the detector. c, d Images of S^+ ions for $\beta = 45^\circ$ and -45° , respectively with the static field increased to $E_{\text{stat}} = 594 \text{ V/cm}$. In c and d respectively 80 % and 19 % of all S^+ ions appear in the upper part of the detector. The images are recorded at lens position, $Y = 1.9 \text{ mm}$ with the deflector turned on at 7 kV. The intensity of the YAG and probe pulse are $8 \times 10^{11} \text{ W/cm}^2$ and $5.4 \times 10^{14} \text{ W/cm}^2$, respectively.

E_{stat} , with an excess of S^+ in the upper (lower) region for $\beta_{\text{align}} = 45^\circ$ (-45°), shows that the molecules are oriented with the S-end preferentially pointing toward the extractor electrode where the electrical potential is lowest. Hence, the permanent dipole moment of OCS is pointing in the same direction as E_{stat} .

To quantify the up/down asymmetry, i. e. the degree of orientation, we determine for each image the number of S^+ ions, N_{up} , in the upper part of the $S^+ + \text{OC}^+$ channel (i. e. ions detected in the upper half of the images) compared to the total number of ions, N_{total} , in the channel. The ratio $N_{\text{up}}/N_{\text{total}}$ is then used to quantify the degree of orientation. In Fig. 5.6 image b and c 66 % and 33 % of the ion hits are detected in the upper half of the image, respectively. When the deflector is turned on and the foci of the lasers are moved to the edge of the most deflected molecules (Fig. 5.6 image e and f) the alignment and orientation is significantly improved, with 81 % (19 %) of the ions appearing in the upper

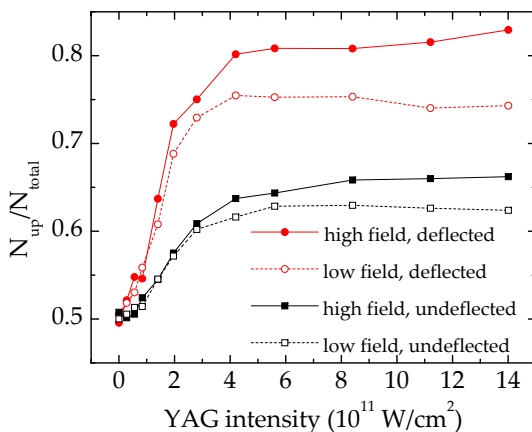


Figure 5.8: Degree of orientation as a function of the YAG intensity for OCS. The polarization of the YAG and the probe pulses are kept fixed through the series at $\beta_{align} = 30^\circ$ and $\beta_{probe} = 90^\circ$ of Fig. 5.5. The labels "undeflected" and "deflected" correspond to images recorded at lens position $Y = 0.0$ with the deflector turned off and $Y = 1.9$ mm with the deflector at 7 kV. The labels "low field" and "high field" refer to two different extraction fields corresponding to 345 V/cm and 594 V/cm, respectively. The intensity of the probe pulse is $5.4 \times 10^{14} \text{ W/cm}^2$.

half of the region corresponding to the $S^+ + OC^+$ channel of image e (f). To investigate the influence of the amplitude of the static field and the intensity of the YAG pulse measurements were performed at two different values of the static electric field as a function of YAG intensity. Figure 5.7 shows S^+ ion images from Coulomb explosion of the deflected OCS molecules similar to Fig. 5.6 image e and f, with the YAG pulse polarized at $\beta_{align} = 45^\circ$ or -45° with the amplitude of the static field at $E_{stat} = 345 \text{ V/cm}$ and 594 V/cm , respectively. A clear effect of the static field is observed.

To summarize and quantify the degree of orientation even further the N_{up}/N_{total} ratio is plotted as a function of the intensity of the YAG pulse for undeflected and deflected OCS molecules at two different amplitudes of the static field (see Fig. 5.8).

When state selected molecules are used a high degree of orientation is observed even at low intensity of the YAG pulse. Although the change in alignment degree shown in Fig. 5.4 between undeflected and deflected molecules was minor, the difference here is striking and clearly shows the advantage of selecting the lowest lying rotational states for strongly increasing the degree of

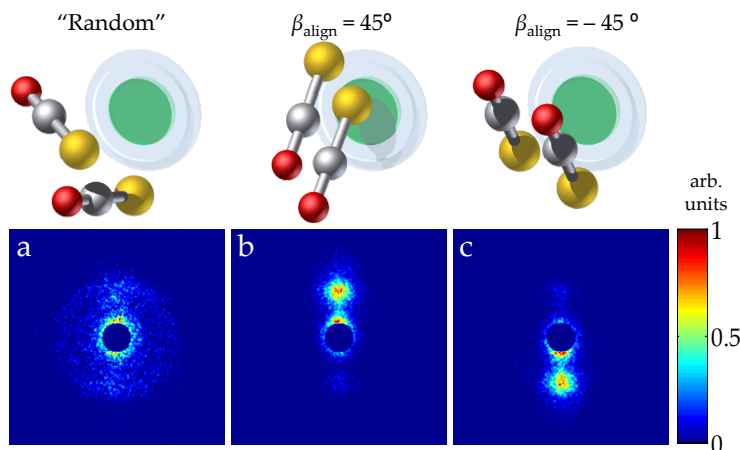


Figure 5.9: S^+ ion images illustrating orientation for $\beta_{\text{align}} = 45^\circ$ and -45° , respectively, recorded when the linearly polarized probe pulse Coulomb explodes the deflected OCS molecules. The probe is polarized parallel to the polarization of the YAG pulse, at $\beta_{\text{probe}} = 45^\circ$ and -45° , respectively. The images are recorded at lens position 2.15 mm with the deflector turned on at 7 kV. The intensity of the YAG and probe pulse are 1.4×10^{12} W/cm² and 5.4×10^{14} W/cm² respectively. The static field is $E_{\text{stat}} = 594$ V/cm.

orientation. As mentioned previously the choice of probe geometry clearly underestimates the degree of orientation. To quantify the extent of the error, S^+ ion images were recorded at $\beta_{\text{align}} = 45^\circ$ and -45° , with the probe pulse polarized parallel to the YAG pulse at $\beta_{\text{probe}} = 45^\circ$ and -45° , respectively (Fig. 5.9). The images are recorded under conditions otherwise similar to Fig. 5.6 e and f. A clear improvement is observed with the number of ions appearing in the upper half of the region corresponding to the $S^+ + OC^+$ channel increasing from 81 % (Fig. 5.6 image e) to 84 % (Fig. 5.9).

Finally, it should be noted that although preparation of a single quantum state should be feasible for OCS, this has not been verified experimentally yet. The degrees of alignment and orientation achieved in this section are not consistent with the selection of the rotational ground state. From the measurement we can not eliminate the possibility of bent states being populated in the supersonic expansion, that are also deflected.

5.4 Laser-Induced Alignment and Orientation of Asymmetric Top Molecules

In this section the methods described in the previous section are extended to the general class of asymmetric top molecules. To illustrate 1D-alignment and orientation of state selected asymmetric top molecules experiments are performed on iodobenzene. The vertical profiles of the molecular beam were already characterized in Chapter 4.

5.4.1 Laser-Induced Alignment

For iodobenzene the basic experimental observables are 2D I^+ ion images recorded when the IB molecules are irradiated with both the YAG pulse and the probe pulse. The geometry of the laser pulse polarizations with respect to the velocity map imaging VMI spectrometer is similar to the one applied in the alignment experiments of OCS (see Fig. 5.2). Hence, the YAG pulse is linearly polarized along the vertical direction and the probe pulse linearly polarized perpendicular to the detector plane, ensuring no bias on the molecular orientation in the plane of the detector. This results in a circularly symmetric I^+ image, when only the probe pulse is used (Fig. 5.10, image A1). When the YAG pulse is included (Fig. 5.10, image A2-A4), the I^+ images exhibit strong angular confinement along the polarization of the YAG pulse.

The I^+ ions appear as two radially localized regions, corresponding to two different fragmentation channels of the Coulomb explosion. The radius of the outermost (and weakest) ring is approximately $\sqrt{2}$ times larger than the radius of the innermost (and brightest) ring. Since the radius is proportional to the velocity of the ions, the I^+ ions from the outermost ring originate from a Coulomb explosion channel that releases twice as much kinetic energy as the channel producing the I^+ ions in the innermost ring. As pointed out in several previous studies from our group (see for instance [16]), this is only consistent with the innermost ring originating from IB being doubly ionized by the probe pulse and fragmenting into an $I^+ + C_6H_5^+$ ion pair, and the outermost ring originating from I^+ ions formed by triple ionization and fragmentation into an $I^+ + C_6H_5^{2+}$ ion pair. As shown in the previous section the pronounced angular confinement observed in images A2 and A4 is quantified by calculating the expectation value of $\langle \cos^2 \theta_{2D} \rangle$, where θ_{2D} here is the angle between the YAG pulse polarization and the projection of the I^+ recoil velocity vector onto the detector plane. In this section $\langle \cos^2 \theta_{2D} \rangle$ values are calculated only from ions detected in radial region corresponding to the outermost fragmentation channel. By doing so, the YAG intensities probed are restricted to a narrow range close to the maximum value, as the high nonlinearity of the multiphoton process occurs efficiently only

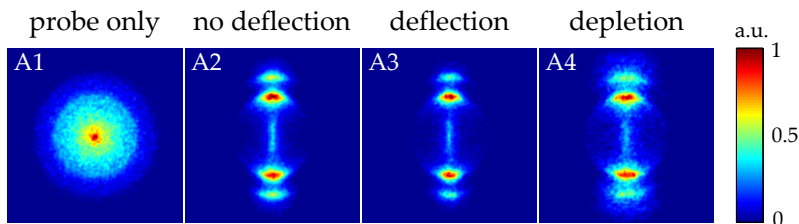


Figure 5.10: I^+ ion images illustrating alignment, recorded when the probe pulse Coulomb explodes the IB molecules seeded in 90 bar He. The polarizations of the YAG and the probe pulses are kept fixed as illustrated in Fig. 5.2. The labels "no deflection", "deflection", and "depletion" correspond to images recorded at lens position $Y = 0.0, 1.0$ and -0.9 mm, respectively, the latter two with the deflector at 10 kV (see Fig. 4.4a). The intensities of the YAG and probe pulse are 8×10^{11} W/cm² and 5×10^{14} W/cm², respectively. $E_{\text{stat}} = 297$ V/cm. The color scale indicates the relative number of ions. This color scale is the same for all subsequent figures showing ion images in this chapter.

in the spatial regions close to the focal point of the YAG beam. Image A1, recorded with only the probe pulse present, should correspond to a target of randomly oriented molecules. As expected the image is circular symmetric and $\langle \cos^2 \theta_{2D} \rangle = 0.515$. When the YAG pulse is included (image A2) a pronounced angular confinement is observed along the polarization of the YAG pulse and $\langle \cos^2 \theta_{2D} \rangle$ is increased to 0.947. When the deflector is turned on and the laser foci moved to the edge of the most deflected molecules (at the position marked in Fig. 4.4 a), corresponding to molecules in the lowest rotational states, the angular confinement is further enhanced (image A3) leading to a $\langle \cos^2 \theta_{2D} \rangle$ value of 0.968. By contrast, when the experiment is conducted on the least deflected molecules in the depleted region (image A4), corresponding to molecules in the highest rotational states, the alignment is weakened and $\langle \cos^2 \theta_{2D} \rangle = 0.900$.

We repeated the alignment measurements when IB was seeded in Ne. The results are displayed in Fig. 5.11. Like in the He case a pronounced improvement is observed when deflected rather than undeflected molecules are employed. Figure 5.11 shows images of I^+ recorded at three different intensities of the YAG laser for both undeflected and deflected molecules seeded in Ne. The effect of the deflector is clearly seen when comparing, for instance, image B1 (deflected) and A1 (undeflected). At this low YAG intensity 2.3×10^{10} W/cm² weak alignment is obtained in the nondeflected beam with $\langle \cos^2 \theta_{2D} \rangle = 0.695$. Going to the edge of the deflected molecular beam (position indicated in Fig. 4.4 b) a clear en-

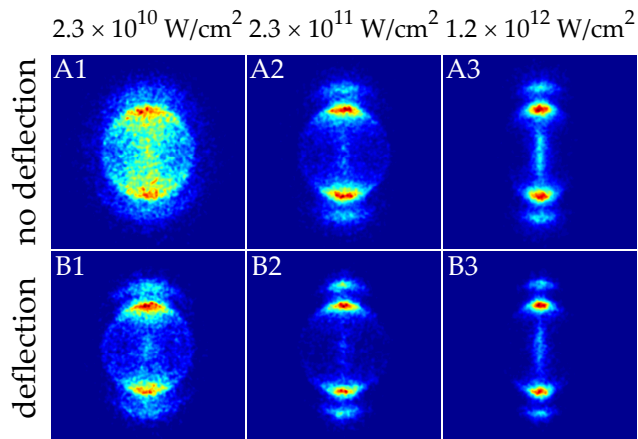


Figure 5.11: I^+ ion images illustrating alignment at different intensities of the YAG pulse, recorded when the probe pulse Coulomb explodes IB molecules seeded in 20 bar Ne. The labels "no deflection" and "deflection" correspond to images recorded at lens position $Y = 0.0$ mm (deflector turned off) and 2.15 mm (deflector at 10 kV), respectively. The intensity of the probe pulse is 5×10^{14} W/cm².

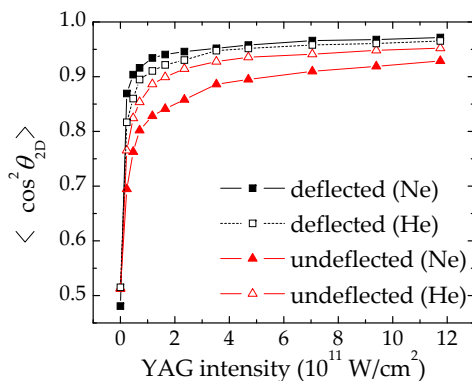


Figure 5.12: Degree of alignment as a function of the YAG intensity for IB seeded in 20 bar Ne or 90 bar He. The intensity of the probe pulse is 5×10^{14} W/cm².

hancement is observed (image B1) with the $\langle \cos^2 \theta_{2D} \rangle$ value rising to 0.869. Also, at high YAG intensity 1.2×10^{12} W/cm² the difference in angular confinement comparing the undeflected (image A3) to the deflected molecules (image B3) is visible. While $\langle \cos^2 \theta_{2D} \rangle = 0.929$ represents the limit of the degree of alignment of IB seeded in Ne in the undeflected beam, employing the deflector leads to an unprecedented degree of laser-induced alignment of $\langle \cos^2 \theta_{2D} \rangle = 0.972$. To quantify the angular information of the images, $\langle \cos^2 \theta_{2D} \rangle$ values are plotted as a function of YAG intensity; the results are displayed in Fig. 5.12 for molecules seeded in Ne as well as He^a. Even at very low laser intensities, a high degree of alignment can be obtained from an ensemble of quantum-state-selected molecules. The tendency shown in this graph with a steep rise and early saturation of the degree of alignment agrees with previous results investigating the dependence of alignment on the rotational temperature of the ensemble of molecules [60]. Effectively, the quantum-state selection corresponds to a "colder" albeit nonthermal beam. The contrast between the undeflected and the deflected beam is greater when Ne is used instead of He as a carrier gas. In the undeflected beam the maximum degree of alignment that can be achieved is smaller in Ne because the rotational cooling in the supersonic expansion is less effective due to the lower stagnation pressure [81]. Additionally, in the deflected beam, a better degree of alignment is expected for Ne, as the efficiency of the quantum-state selection in the present setup is significantly enhanced due to the longer residence time in the deflector (see Chapter 4).

5.4.2 Mixed-Field Orientation

Next, we discuss orientation due to the combined action on the molecules from the YAG pulse and the static electric field, E_{stat} , from the VMI electrodes. Figure 5.13 illustrates the polarization state of the YAG and the probe pulse with respect to the static electric field of the VMI electrodes. The important difference compared to the alignment data is that the YAG polarization is rotated away from the axis perpendicular to the static field. Thus, the orientation data result from geometries where the angle β_{align} between the YAG polarization (the C-I bond axis) and the static electric field is different from 90° , (see Fig. 5.13). In contrast to the OCS experiments, orientation of IB is imaged using a circularly polarized probe pulse. This ensures that any molecule will be ionized and thus detected with the same probability independent of β_{align} . This circularly polarized probe will induce some bias on the angular distribution of the I^+ ions

^aIt should be noted that the measurements presented in Fig. 5.12 with He as a carrier gas, were recorded under slightly different conditions than the remaining results on IB presented in this chapter. The results were recorded after the vacuum chamber had been upgraded with exchange of the first skimmer and introduction of the capacitor plates, which may have led to slightly better cooling of the undeflected beam.

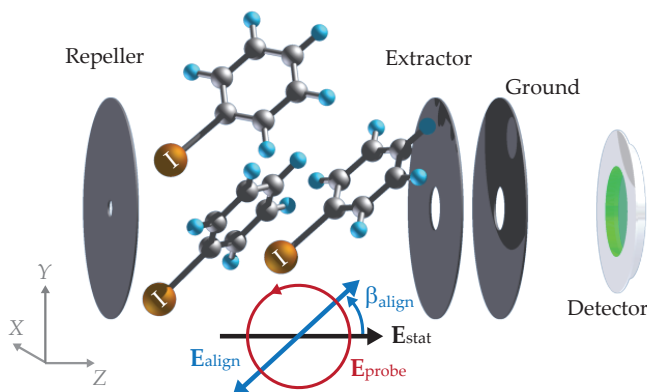


Figure 5.13: Schematic illustration of the polarization state of the YAG and the probe pulse with respect to the static electric field and the detector plane used to characterize orientation, including a sketch illustrating molecular orientation.

(see Fig. 5.14 image A1 and C1), however, importantly, it is up/down symmetric. Figure 5.14 shows I^+ ion images for different β_{align} values for both deflected and undeflected molecules seeded in He. As mentioned, the circularly polarized probe alone gives rise to an image that exhibits some angular confinement with $\langle \cos^2 \theta_{2D} \rangle = 0.70$ (Fig. 5.14, A1). Consequently, including the YAG pulse at $\beta_{\text{align}} = 90^\circ$, results in an image (Fig. 5.14, B1) that appears slightly different from the corresponding image with a linearly polarized probe (Fig. 5.10 A2), but still shows that the molecules are tightly aligned. Focusing first on the nondeflected data of Fig. 5.14 (rows A and B) two prominent changes are observed as the polarization of the YAG pulse is gradually rotated away from the detector plane (images A2-A6 and B2-B6). First, the location of the I^+ rings shifts closer to the center of the images. This is due to the fact that the C-I axis alignment and thus the emission direction of the I^+ ions follows the YAG pulse polarization. When the C-I axis is aligned at an angle β_{align} , the magnitude of the I^+ velocity vector recorded on the detector will be reduced by the factor $\sin(\beta_{\text{align}})$. The detrimental effect on the radial (velocity) resolution is obvious at $\beta_{\text{align}} = 135^\circ / 45^\circ$ (image A5 and B5) and $30^\circ / 150^\circ$ (image A6 and B6), where the two I^+ explosion channels, $I^+ + C_6H_5^+$ and $I^+ + C_6H_5^{2+}$, become indistinguishable as they merge in the 2D projection onto the detector plane. Second, as the YAG pulse polarization is turned away from 90° , the up/down symmetry of the images, characteristic for the alignment data described in Sec. 5.4.1 (and Fig. 5.14 column 1) is broken. For images with $90^\circ < \beta_{\text{align}} < 180^\circ$ (images B2-B6), more I^+ ions are detected in the upper part, whereas for $0^\circ < \beta_{\text{align}} < 90^\circ$ (images A2-A6), more I^+ ions are de-

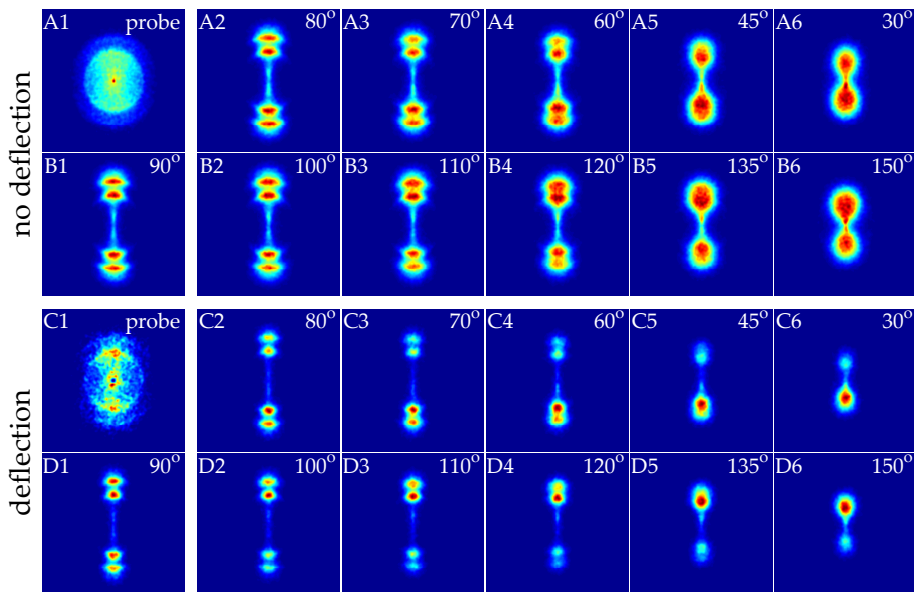


Figure 5.14: I^+ ion images illustrating orientation for different values of β_{align} , recorded when the circularly polarized probe pulse Coulomb explodes the IB molecules seeded in 90 bar He. The labels "no deflection" and "deflection" correspond to images recorded at lens position $Y = 0.0$ mm (deflector turned off) and 1.0 mm (deflector on at 10 kV), respectively. The intensity of the YAG and the probe pulse is 8×10^{11} W/cm² and 5×10^{14} W/cm², respectively. $E_{\text{stat}} = 595$ V/cm

tected in the lower part. The asymmetry becomes more pronounced as the YAG polarization is rotated closer to the axis of the static field. We interpret these observations as orientation due to the combined effect of the YAG laser field and the projection of the static electric extraction field E_{stat} on the YAG polarization axis. This projection (numerical value: $|\cos(\beta_{\text{align}})|E_{\text{stat}}$) increases as β_{align} is rotated toward 0° or 180° , which is expected to cause an increase in the orientation [24, 25], in agreement with the experimental findings. As discussed in Chapter 4, all states of IB are high-field seeking, hence the orientation is expected to place the I-end of the molecules toward the repeller plate (see Fig. 5.13), where the electrical potential is highest, because the dipole moment of IB is directed along the C-I axis pointing from iodine ("negative end") toward the phenyl ring ("positive end"). The expected resulting molecular orientation at a given angle of β_{align} is shown in Fig. 5.13. Thus, for $0^\circ < \beta_{\text{align}} < 90^\circ$, the I^+ ions are expected to preferentially be ejected downward and, for $90^\circ < \beta_{\text{align}} < 180^\circ$, they will be ejected

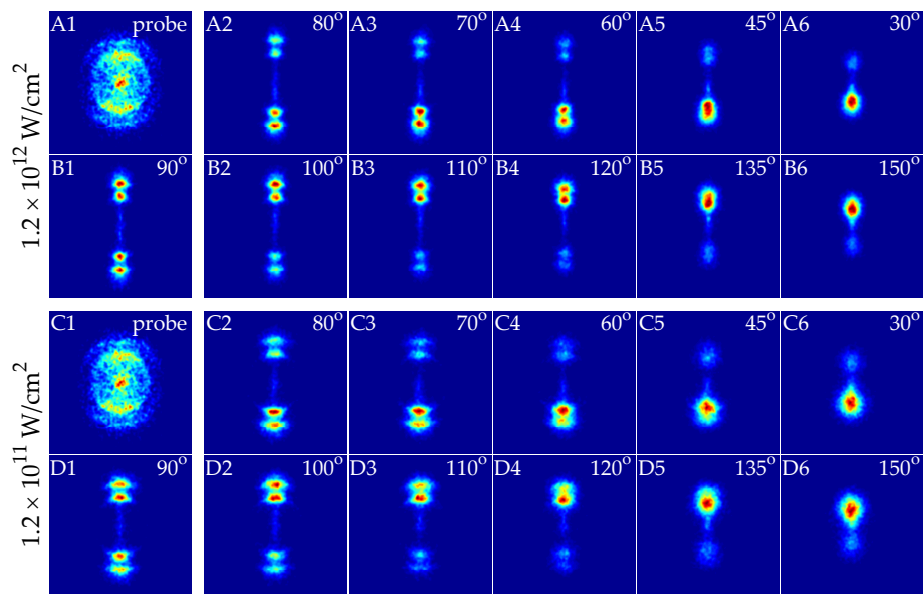


Figure 5.15: I^+ ion images of deflected IB seeded in 20 bar Ne, illustrating orientation at two different intensities of the YAG pulse. The images are recorded at lens position $Y = 2.25$ mm with the deflector at 10 kV. The intensity of the probe pulse is 5×10^{14} W/cm². $E_{\text{stat}} = 595$ V/cm

upward. This is in agreement with the up/down asymmetry in the images. The alignment (image D1) and orientation (images C2-C6 and D2-D6) improve significantly when the deflector is turned on and the foci of the lasers are moved to the position of the most deflected molecules (position marked in Fig. 4.4 a). The markedly better orientation resulting in a much more pronounced up/down asymmetry is clearly visible even when the YAG pulse is only turned slightly away from perpendicular, i. e. comparing deflected and undeflected images for $\beta_{\text{align}} = 100^\circ$ (images C2 and A2) and $\beta_{\text{align}} = 80^\circ$ (images D2 and B2). From the previous discussion it appears that the highest degree of orientation is achieved when β_{align} is rotated toward 0° or 180° . This is clearly seen from the images in rows C and D and, again, the improvement obtained with deflected molecules is striking (compare image C6 to A6, or D6 to B6).

Similar orientation measurements were conducted for IB seeded in Ne instead of in He. Figure 5.15 shows I^+ images at a series of β_{align} values for two different intensities of the YAG pulse recorded with the deflector at 10 kV at the position marked in Fig. 4.4 b. Compared to the images displayed in Fig. 5.14

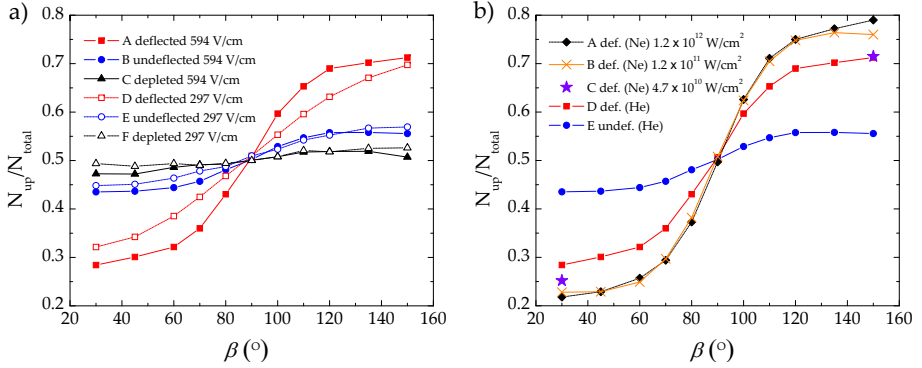


Figure 5.16: Orientation of iodobenzene represented by $N(I^+)_{\text{up}}/N(I^+)_{\text{total}}$ as a function of β_{align} , seeded in either He or Ne. Experiments conducted with He as a carrier gas are obtained at lens position $Y = 1.0$ mm for the deflector at 10 kV and lens position $Y = 0.0$ mm for the deflector off, the intensity of the YAG pulse was 7.8×10^{11} W/cm². Experiments involving the Ne carrier gas correspond to the lens position $Y = 2.25$ mm for deflector at 10 kV, the intensities of the YAG pulse are displayed in the insert. The intensity of the probe pulse for all curves was fixed at 5×10^{14} W/cm². $E_{\text{stat}} = 594$ V/cm.

rows A and B, although recorded at slightly different intensities of the YAG pulse, a significant improvement is observed. Furthermore even at low intensity of the YAG a high degree of orientation for IB seeded in Ne is achieved. At the same time some loss in the angular confinement, i. e. in the alignment degree, is visible. We assign the clear improvement in the up/down asymmetry to the more stringent state selection in Ne compared to He as described in Chapter 4, hence, manifesting itself in a higher degree of orientation.

To quantify the up/down asymmetry, i. e. the degree of orientation, we determine for each image the number of I^+ ions, $N(I^+)_{\text{up}}$, in the upper part of the $I^+ + C_6H_5^+$ and $I^+ + C_6H_5^{2+}$ channels (i. e. ions detected in the upper half of the images) as well as the total number of ions, $N(I^+)_{\text{total}}$ ($= N(I^+)_{\text{up}} + N(I^+)_{\text{down}}$). This ratio, as a function of β_{align} , is displayed in Fig. 5.16. Focusing first on curves C and D, representing IB seeded in He, the difference between the data for the deflected molecules and the data obtained with the deflector turned off is striking and shows the advantage of selecting the lowest-lying rotational states for strongly increasing the degree of orientation. The further improvement when Ne is used instead of He is clear from curves A and B. These two curves also show that the pronounced degree of orientation is maintained when the intensity of the YAG pulse is lowered by an order of magnitude compared to the

maximum value of $1.2 \times 10^{12} \text{ W/cm}^2$.

In Fig. 5.16 a the ratio $N(I^+)_{\text{up}}/N(I^+)_{\text{total}}$ is plotted as a function of β_{align} for deflected and undeflected molecules seeded in He for two different extraction fields. The difference between the data for the most deflected molecules and the data obtained with the deflector turned off is striking and shows the advantage of selecting the lowest-lying rotational states for strongly increasing the degree of orientation. From the data for deflected molecules it is also obvious that increasing the static electric field by a factor of 2 leads to better orientation. In addition, Fig. 5.16 a shows the results obtained for the least deflected molecules in the depleted region ($Y = -0.9 \text{ mm}$). The degree of orientation is significantly reduced compared to that obtained without deflection. In Fig. 5.16 b) the ration is plotted as a function of β_{align} for deflected molecules seeded in Ne at two different intensities of the YAG pulse (curve A and B), compared to the undeflected (curve D) and deflected (curve E) molecules seeded in He. The improvement when Ne is used instead of He is clear from curves A and B. These two curves also show that the pronounced degree of orientation is maintained when the intensity of the YAG pulse is lowered by an order of magnitude compared to the maximum value of $1.2 \times 10^{12} \text{ W/cm}^2$. Even at extremely low intensity of the YAG ($4.7 \times 10^{10} \text{ W/cm}^2$) marked with purple stars (C), a high degree of orientation is achieved when molecules are selected in the lowest rotational quantum states.

6

LASER INDUCED 3D ALIGNMENT AND ORIENTATION

6.1 Introduction

One of the great advantages of laser induced alignment and orientation is its extension to the general class of molecules.

As it was seen in the previous chapter in the case of a linearly polarized laser field, the most polarizable axis of a molecule is aligned along the polarization direction of the aligning laser, which is sufficient to ensure strong angular confinement of the figure axis of the molecules and, therefore, complete alignment control of linear and symmetric top molecules. This is termed 1-dimensional (1D) alignment. For asymmetric top molecules, 1D alignment does not suffice to provide complete alignment control. Rather, all three molecular axes of polarizability must be confined to laboratory-fixed axes. The first report on 3D alignment came from Stapelfeldt and coworkers in 2000 [18]. Here adiabatic 3D alignment was experimentally demonstrated by confining the two most polarizable axes of 3,4-dibromothiophene through the use of an elliptically polarized laser field.

Field free 3D alignment has been explored both theoretically and experimentally using two timedelayed orthogonally polarized femtosecond laser pulses by

Underwood and coworkers [19, 20]. Later Rouzee *et al.* [21] presented theoretical framework as well as experimental evidence of field free 3D alignment induced by an elliptically polarized kick pulse. In a different approach strong 3D alignment has recently been achieved by Stapelfeldt and coworkers by combining the techniques of adiabatic and nonadiabatic alignment [22, 23]. In these experiments a linearly polarized nanosecond laser pulse strongly adiabatically aligns the most polarizable axis of an asymmetric molecule (3,5-difluoriodobenzene) while an orthogonally polarized femtosecond kick pulse excites controlled rotation about the aligned axis.

As already mentioned in the case of polar molecules, confinement of the molecular axes is not sufficient to achieve full orientational control; it is also necessary to control the direction of the permanent dipole. As described in the previous chapter orientation can be added to alignment by combining the strong laser field with a weak static electric field. Therefore, we use 1D orientation to denote 1D alignment and, simultaneously, a preferred direction of the permanent dipole moment. Likewise, 3D orientation refers to 3D alignment occurring together with a preferred direction of the permanent dipole moment. 3D orientation was demonstrated by Sakai and coworkers in 2005 [27] using the combined action of a static electric and an elliptically polarized nanosecond laser field.

In the previous chapter it was seen how 1D alignment and orientation was strongly enhanced using rotational quantum-state selected molecules. In this chapter the method is extended and it is demonstrated how the use of rotational state-selected molecules also enables significant improvement of laser induced 3D alignment and (mixed-field) 3D orientation. The studies are carried out on 2,6-difluoriodobenzene ($C_6H_3F_2I$) molecules in the adiabatic limit.

6.2 Experimental Setup

A mixture of a few mbar of $C_6H_3F_2I$ and 90 bar of helium is expanded into vacuum using our pulsed Even-Lavie valve to produce a molecular beam with a rotational temperature of approximately 1 K. After passing through two 1 mm-diameter skimmers, the molecular beam enters a 15 cm-long electrostatic beam deflector. After passing the deflector, the molecular beam enters the target / detection area through a 1.5 mm-diameter skimmer where it is crossed by one or two laser beams that are focused by a spherical lens with a focal length of $f = 300$ mm. The lens is mounted on a vertical translation stage so that the height of the laser foci can be adjusted with high precision. One laser beam, consisting of 30 fs-long pulses (800 nm, beam-waist of $\omega_0 = 21$ mm which corresponds to 4×10^{14} W/cm²) is used to probe the molecules. In the first part of the experiment,

this laser beam is used to characterize the deflection by determining the density, at a given height, of the molecular beam via photoionization. Hereafter, this laser beam is used for Coulomb exploding of the molecules to determine their alignment and orientation by imaging the ionized fragments on the plane of the microchannel plate (MCP) detector. The second laser beam, consisting of 10 ns-long pulses from a Nd:YAG laser (1064 nm, $\omega_0 = 36$ mm), is used to align and orient the molecules. Two intensity values of the pulses are applied: 1.2×10^{12} W/cm² and 1.8×10^{11} W/cm², denoted hereafter as $I_{\text{YAG,high}}$ and $I_{\text{YAG,low}}$, respectively. The 2D ion images are recorded with a CCD camera. In particular, the I⁺ and F⁺ fragment ion distributions are useful experimental observables since these ions recoil along the symmetry axis and in the plane of the molecule, respectively. Thereby, they allow the determination of the molecular orientation at the time of the probe pulse. Also, the time-of-flight (TOF) of the ions from the laser interaction spot to the MCP is recorded. The experiments are conducted at 20 Hz, limited by the repetition rate of the YAG laser.

6.3 Results and Discussion

6.3.1 Molecular Beam Deflection

The effect of the deflector on the molecular beam is illustrated in Fig. 6.1 by the vertical intensity profiles, which are obtained by recording the I⁺ signal from photoionization due to the femtosecond probe laser as a function of the vertical position of the laser focus. When the deflector is turned off, the molecular beam extends over ~ 1.7 mm, mainly determined by the diameter of the last skimmer before the target area. When the deflector is turned on, the molecular beam profile shifts upwards. The shift becomes more pronounced as the voltage on the deflector is increased from 5 to 10 kV, consistent with the observations in Chapter 4. Molecules in the lowest rotational quantum states have the largest Stark shifts and are, therefore, deflected the most, consistent with the observations of Chapter 4. The following, experiments are conducted on quantum state-selected molecules by positioning the laser foci close to the upper cut-off region in the 10 kV profile at the lens position indicated by the arrow in Fig. 6.1 ($Y = 1.18$ mm).

6.3.2 1D and 3D Alignment

First it is confirmed that C₆H₃F₂I can be 1D aligned similar to the studies of iodobenzene in Sec. 5.4.1. From quantum chemistry calculations [119] the polarizability components of the C₆H₃F₂I molecules are determined to be $\alpha_{zz} = 21.3 \text{ \AA}^3$, $\alpha_{yy} = 14.5 \text{ \AA}^3$, and $\alpha_{xx} = 8.5 \text{ \AA}^3$, where the z-axis is parallel to the

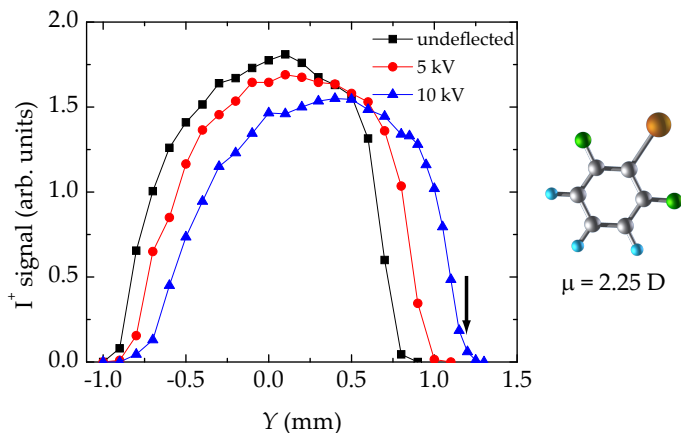


Figure 6.1: Vertical profiles of the molecular beam measured by recording the I^+ signal as a function of the vertical position of the fs probe beam focus. The experimental data are shown by black squares (deflector off, 0 kV), red circles (5 kV) and blue triangles (10 kV). The arrow denotes the position of the probe laser focus for acquiring images and TOF spectra of deflected molecules described in the following sections.

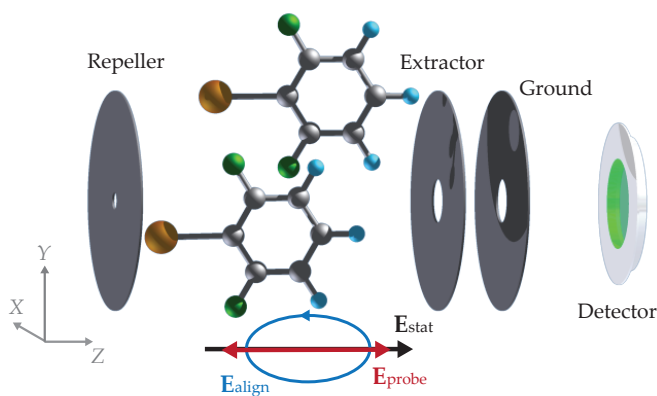


Figure 6.2: Schematic illustration of the polarization state of the YAG and the probe pulse with respect to the static electric field and the detector plane used to characterize orientation, including a sketch illustrating molecular orientation.

C-I axis, the y-axis is perpendicular to the z-axis but still in the molecular plane, and the x-axis is perpendicular to the molecular plane. It is therefore expected that a linearly polarized laser field will align the C-I axis along the polarization axis. With an elliptically polarized beam, the largest polarizability axis of the molecule is expected to be aligned along the major axis of the elliptical field, and the second most polarizable axis along the minor axis of the field. Therefore, it is expected that an elliptically polarized field will align the C-I axis along the major polarization axis and the molecular plane to the polarization plane. Initially, the linearly-polarized YAG pulse is used to induce 1D alignment of the $C_6H_3F_2I$ molecules. In Fig. 6.3, 2D I^+ ion images recorded with and without the YAG pulse for deflected and undeflected molecules. In the absence of the YAG pulse, the I^+ ion images are circularly symmetric (Fig. 6.3, images A1 and B1) due to the circular symmetry introduced by polarizing the probe pulse perpendicular to the detector plane. When the YAG pulse, polarized parallel to the detector plane, is applied, the I^+ ions exhibit strong angular localization about the polarization axis (Fig. 6.3 A2-A3 and B2-B3), showing that the C-I axis of the molecules is strongly confined along the YAG polarization, i. e. the $C_6H_3F_2I$ molecules are 1D adiabatically aligned. Images obtained with the YAG polarization parallel to the plane of the detector will in this chapter be regarded as a "side-view" image of molecular alignment. Similar to iodobenzene the degree of alignment is quantified by $\langle \cos^2 \theta_{2D} \rangle$, where θ_{2D} is the angle between the projection of the I^+ recoil velocity on the detector plane and the YAG polarization. The I^+ ions appear as two angular confined radial rings. The innermost (and brightest) ring results from I^+ ions when $C_6H_3F_2I$ is doubly ionized by the probe pulse and fragments into an $I^+ + C_6H_3F_2^+$ ion pair, whereas the outermost ring results from I^+ ions formed from triple ionization and fragmentation into an $I^+ + C_6H_3F_2^{2+}$ ion pair. The value of $\langle \cos^2 \theta_{2D} \rangle$ is determined in the radial range corresponding to the outermost ring. In the absence of the YAG pulse (Fig. 6.3, image A1 and B1), $\langle \cos^2 \theta_{2D} \rangle = 0.50$, as expected for randomly oriented molecules. The degree of alignment for the undeflected molecules at high intensity of the YAG pulse is $\langle \cos^2 \theta_{2D} \rangle = 0.94$ (image A3). When the deflector is turned on and the laser foci moved close to the upper cutoff region in the 10 kV profile ($Y = 1.18$ mm), corresponding to the lowest lying rotational states of the $C_6H_3F_2I$ molecules, the 1D alignment sharpens with an increase in the alignment degree corresponding to $\langle \cos^2 \theta_{2D} \rangle = 0.96$. Similar a clear improvement in the degree of alignment is observed at low intensity of the YAG pulse (compare image A2 to B2) with $\langle \cos^2 \theta_{2D} \rangle$ improving from 0.87 to 0.92.

To verify 3D alignment images are recorded with the YAG pulse polarized perpendicular to the detector plane, corresponding to the "end-views" of the molecules. All images in Fig. 6.4 are recorded in the end-view geometry. The tight confinement of the I^+ ions near the center (A2-A4 and C2-C4), compared

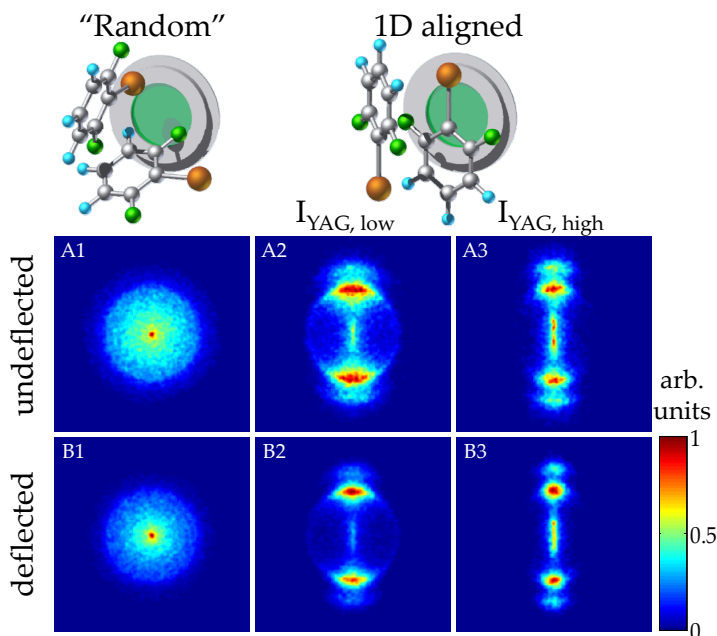


Figure 6.3: I^+ ion images illustrating alignment, recorded when the probe pulse Coulomb explodes the $C_6H_3F_2I$ molecules. The polarizations of the probe and the YAG pulses are kept fixed perpendicular and parallel to the detector, respectively, in a geometry similar to the one illustrated in Fig. 5.2. The labels "undeflected" and "deflected" correspond to images recorded at lens position $Y = 0.0$ mm (deflector turned off) and $Y = 1.18$ mm (deflector at 10 kV), respectively. I^+ images are recorded with the probe pulse alone (image A1 and B1), with the YAG included at an intensity, $I_{YAG,low} = 1.8 \times 10^{11} W/cm^2$ (images A2 and B2) and with the YAG included at an intensity, $I_{YAG,high} = 1.2 \times 10^{12} W/cm^2$ (images A3 and B3) for undeflected (row 1) and deflected (row 2) molecules, respectively. The color scale indicates the relative number of ions and applies for all the subsequent figures of ion images in this chapter.

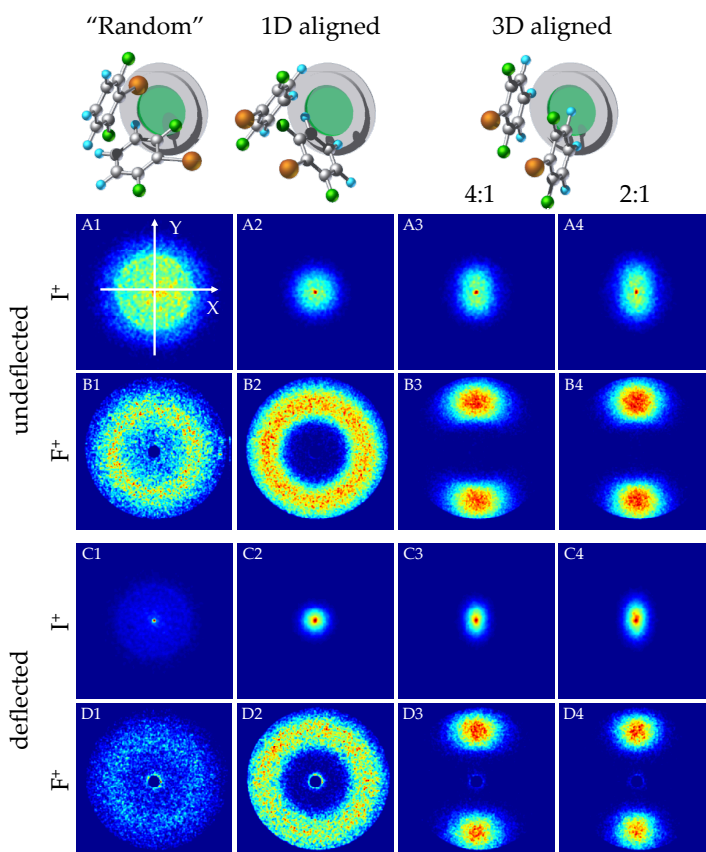


Figure 6.4: Ion images of I^+ and F^+ fragments recorded in "end-view" illustrating 1D and 3D-alignment. Alignment is obtained at an intensity of the YAG pulse of $I_{YAG,high} = 1.2 \times 10^{12} \text{ W/cm}^2$. Column 1 is recorded with the probe pulse only. In column 2 the YAG pulse is included polarized linearly perpendicular to the detector. In column 3 and 4 the YAG pulse is elliptically polarized with an ellipticity intensity-ratio corresponding to 4:1 and 2:1, respectively. Rows A and B correspond to I^+ and F^+ ion images, respectively, recorded at lens position $Y = 0.0 \text{ mm}$ with the deflector turned off. In rows C and D, I^+ and F^+ ion images, respectively, are recorded at lens position $Y = 1.18 \text{ mm}$ and the deflector turned on at 10 kV.

to the I^+ distribution without the YAG pulse (Fig. 6.4, image A1 and C1) is an alternative way to visualize the 1D alignment. In order to quantify the angular confinement, the average distances $\langle X \rangle$ and $\langle Y \rangle$ of I^+ ions along the horizontal (X) and vertical (Y) axes from the center of the end-view images are calculated, see Fig. 6.4 image A1. Without the YAG $\langle X \rangle = 37.4$ pixels and $\langle Y \rangle = 34.8$ pixels. Including the YAG $\langle X \rangle = 19.0$ pixels and $\langle Y \rangle = 19.0$ pixels without voltages applied to the deflector (image A2 in Fig. 6.4), and $\langle X \rangle = 12.3$ pixels and $\langle Y \rangle = 12.2$ pixels with 10 kV applied to the deflector (Fig. 6.4, C2).

1D alignment is also visible in the F^+ images. In the absence of the YAG pulse, the F^+ image, recorded in the end-view, takes the form of a circularly symmetric ring or donut shape (Fig. 6.4 B1 and D1). This is caused by the fact that the linearly polarized probe field preferentially ionizes molecules with their C-I axis along its polarization vector. When the linearly polarized YAG pulse is applied, the circular symmetry is conserved and the ring structure becomes more sharply defined to a localized radial area with no signal detected in the central region (Fig. 6.4, image B2 and D2). Such a ring structure is only compatible with the C-I axis being sharply aligned perpendicular to the detector plane and with the rotation of the molecular plane uniformly distributed around the C-I axis.

Next, we investigate the effect on the molecular alignment when the YAG polarization is changed from linear to elliptical. The end-view of the F^+ ions shows a dramatic change (Fig. 6.4 B3, B4, D3, D4). The initial circular symmetry is replaced by sharp localization along the minor axis (vertical in Fig. 6.4) of the elliptically polarized YAG pulse. The angular localization of the F^+ ions, largest for the 2:1 ellipticity ratio (B4 and D4), shows that the molecular plane is confined to the plane defined by the elliptical polarization, and the conservation of their radial confinement shows that the C-I axis remains localized around the major polarization axis. To quantify the planar confinement, the angular distributions of the F^+ ions were determined by radial integration of the images. The results are displayed in Fig. 6.6. Focusing on panel (a), containing the undeflected data, it is seen that, for the linearly polarized YAG pulse, a uniform distribution emerges, whereas for elliptical polarization, the angular distribution is localized. For the 4:1 ellipticity ratio (meaning that the intensity along the major axis is four times the intensity along the minor axis) the full widths at half maximum (FWHM) of the peaks in the angular distribution are 52.5° , and for the 2:1 ratio they are 48.5° . Regarding the localization of the C-I axis, more precise insight is obtained by observing the I^+ end-view images. It is seen that the initial circular distribution (Fig. 6.4 A2) develops into an elliptical shape when the YAG polarization is changed from linear to elliptical. This shows that the C-I axis has suffered a small distortion along the minor axis, but remains tightly confined. The distortion is largest for the 2:1 ellipticity ratio. This is evident directly from the images as well as from the X and Y values. With the 4:1

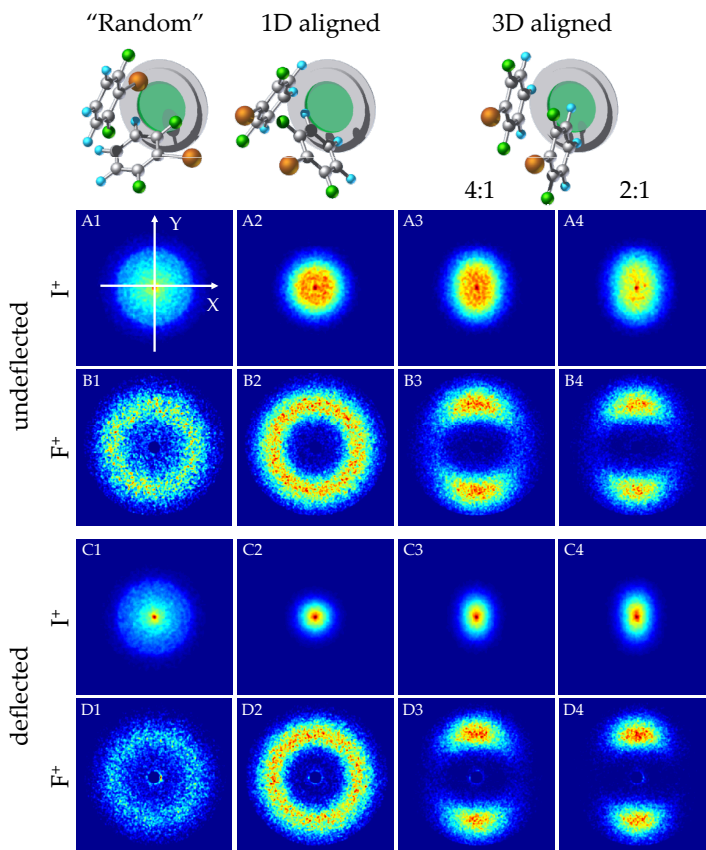


Figure 6.5: Same as Fig. 6.4 however with the intensity of the YAG pulse lowered to $I_{\text{YAG,low}} = 1.8 \times 10^{11} \text{ W/cm}^2$

ratio (A3) $\langle X \rangle = 18.1$ pixels and $\langle Y \rangle = 21.0$ pixels, whereas for the 2:1 ratio (A4) $\langle X \rangle = 18.2$ pixels and $\langle Y \rangle = 23.4$ pixels. Returning to the F^+ images, the C-I axis distortion is actually visible by slightly more radial smearing in the 2:1 image compared to the 4:1 image. Thus, we conclude that the elliptically-polarized YAG pulse induces pronounced 3D alignment of the $C_6H_3F_2I$. The confinement of the molecular plane increases as the polarization state is brought closer to circular polarization, but also gives rise to a larger distortion of the linear confinement of the C-I axis. These findings are consistent with previous observations on other molecules [18, 120].

When the deflector is turned on, the 3D alignment improves. The F^+ ion images show stronger confinement for both the 2:1 and the 4:1 configuration (Fig. 6.4 D3, D4) compared to the corresponding undeflected data (Fig. 6.4 B3, B4). This is also clear from the angular distributions in panel (b) of Fig. 5. For the 4:1 ratio, the FWHM decreases from 52.5° to 43.0° , and for the 2:1 ratio, from 48.5° to 37.0° . Turning to the I^+ end-view images in row C, it is seen that although the C-I axis is still distorted when an elliptically YAG pulse is employed, the C-I axis confinement is much improved compared to the situation for undeflected molecules (compare Fig. 6.4 image C3, C4 to image A3, A4). With the deflected molecules, $\langle X \rangle = 10.7$ pixels and $\langle Y \rangle = 15.3$ pixels for the 4:1 ratio, and $\langle X \rangle = 10.9$ pixels and $\langle Y \rangle = 17.3$ pixels for the 2:1 ratio. We conclude that both 1D and 3D alignment are significantly enhanced when quantum state-selected molecules are used.

Next, it is investigated if strong 3D alignment and orientation can be maintained as the intensity of the YAG pulse is lowered. Maintaining strong alignment even with a weaker alignment field may prove to be important in future applications. Figure 6.5 show 2D ion images of I^+ and F^+ at low intensity of the YAG pulse. The images reveal the same tendency as the high intensity images shown in Fig. 6.4. Again, considerably stronger confinement of the C-I axis and of the molecular plane, i. e. better 1D and 3D alignment, is obtained for deflected relative to the undeflected molecules. Focussing for instance on the end-view image of I^+ obtained with the linearly polarized YAG pulse (Fig. 6.5 C2) shows a circular spot with $\langle X \rangle = 15.7$ pixels, and $\langle Y \rangle = 15.8$ pixels for deflected molecules, whereas for the undeflected molecules $\langle X \rangle = 22.5$ pixels, and $\langle Y \rangle = 22.6$ pixels (Fig. 6.5 A2). The images of the F^+ ions for the 2:1 ratio exhibit stronger angular confinement when deflected molecules (Fig. 6.5 D4) rather than undeflected molecules (Fig. 6.5 B4) are used. This is also evident in the corresponding angular distributions in Fig. 6.6(c) that show a peak with a FWHM of 55.5° for the deflected molecules relative to more than 72° for the undeflected molecules.

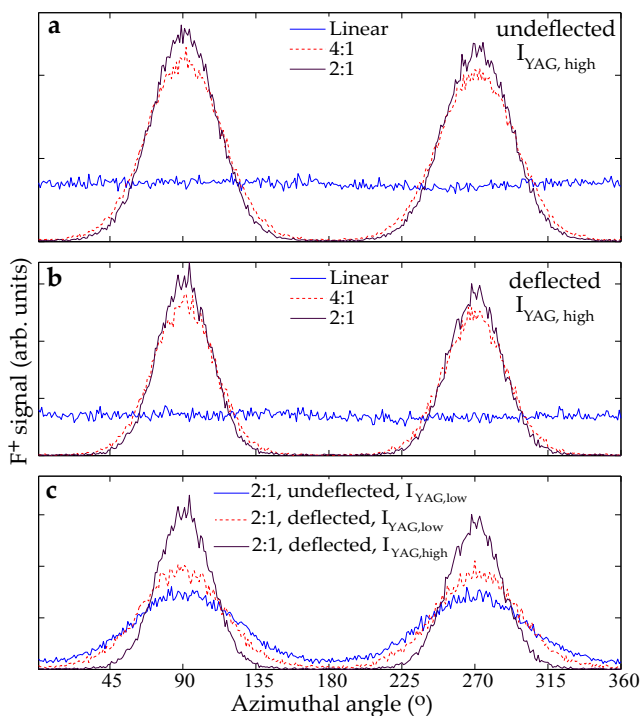


Figure 6.6: Angular distributions of the F^+ fragments for different YAG polarizations and intensities. (a) Angular distributions corresponding to images B2-B4 of Fig. 6.4 for undeflected molecules. (b) Angular distributions corresponding to images D2-D4 of Fig. 6.4 for deflected molecules. (c) Comparison between the angular distributions corresponding to low and high intensity of the elliptically polarized (2:1)YAG pulse, obtained from the F^+ ion images D4 of Fig. 6.4 and B4 and D4 of Fig. 6.5.

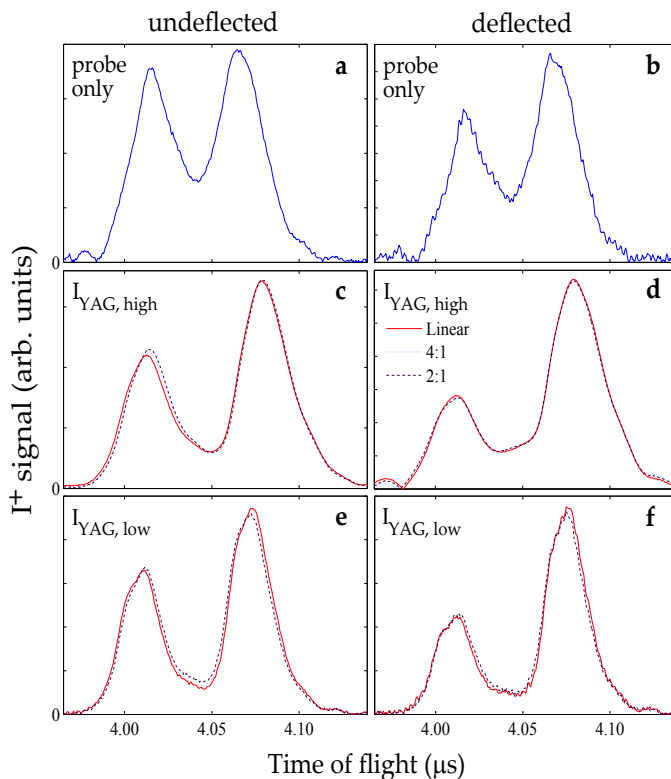


Figure 6.7: Time-of-flight spectra of the I^+ ions recorded with the probe pulse only ((a) and (b)), with the YAG pulse included at high intensity ($I_{YAG,high}$) ((c) and (d)), with the YAG included at low intensity ($I_{YAG,low}$) ((e) and (f)). In panels (c) and (f), the polarization state of the YAG pulse is linear (solid red curves), 4:1 elliptical (dotted blue curves) and 2:1 elliptical (dashed black curves). The data in the left column are recorded for undeflected molecules and the data in the right column for deflected molecules.

6.3.3 1D and 3D Orientation

The permanent electric dipole moment of $C_6H_3F_2I$ is 2.25 D. It is parallel to the C-I axis with the negative end pointing in the direction of the iodine atom. Consequently, it is expected that a static electric field, collinear with the major polarization axis of the alignment field, will force the iodine end of each molecule to point in the direction of the positive electrode of the static field. Our final task is to prove that the molecules are oriented in addition to being aligned. This is accomplished by supplementing the ion images already presented by time of flight measurements of the I^+ ions. The most optimal information is obtained by using the end-view geometry. In this situation, the C-I axis is aligned parallel to the static electric field from the electrodes (693 V/cm) in the ion spectrometer. The TOF spectra of the I^+ ions will now allow us to conclude that the permanent dipole moment (directed from the carbon atom on the C_2 axis to the I atom) is preferentially pointing towards the repeller plate (high electrostatic potential) as we expect. The TOF spectra recorded with the probe pulse alone are shown in Fig. 6.7 (a) and (b). As mentioned in connection with the F^+ ion images, the linearly polarized pulse is preferentially ionizing molecules with their axes along its polarization axis which explains the appearance of a forward and a backward peak [121] centered around 4.045 μs . A mild asymmetry in the signal strength of the forward and the backward peak is observed. For undeflected molecules, the asymmetry, defined as I_b^+ / I_f^+ is 52/48. For the deflected molecules the asymmetry increases to 59/41. To get an insight into the origin of this asymmetry, we calculate the molecular orientation due to the static electric field itself. First, the ensemble-averaged orientation cosine $\langle \cos \theta \rangle$ is calculated quantum mechanically, where θ is the polar angle between the molecular C-I axis and the static field direction. For an ensemble at a rotational temperature of 1 K $\langle \cos \theta \rangle = 0.011$, whereas for an ensemble corresponding to the state-selected molecules after the deflector (height = 1.18 mm, see Fig. 6.1) $\langle \cos \theta \rangle = 0.079^a$. To obtain the backward-forward ratio, b/f, we approximate the orientational distribution function [122] by the truncated series $n(\theta) = 1 + a_1 P_1(\cos \theta) = 1 + \langle \cos \theta \rangle \cos \theta$. Higher order Legendre polynomials can be neglected for the low electric field strength employed here. Furthermore, we assume that the molecules are probed with a detection efficiency scaling as $\cos^2 \theta$ to account for the alignment selectivity of the probe pulse. Using the calculated values for $\langle \cos \theta \rangle$ we get b/f = 52/48 for the 1 K ensemble and b/f = 60/40 for the state-selected ensemble. Both numbers agree well with the observations. We conclude that the observed backward forward asymmetry in the time of flight spectra observed in the absence of the YAG pulse is due to weak orientation induced by the static field, as well as due to alignment selectivity of the probe

^aThe value is estimated from the simulations performed on iodobenzene in Chapter 4.

beam. When the YAG pulse is included, two changes of the TOF spectra occur. First, the forward and the backward peaks become more separated. This results from the strong alignment induced by the YAG pulse. All molecules are confined near the TOF axis, which will cause I^+ ions to be ejected directly towards or 180° away from the detector, thus causing the maximum separation between the forward peaks. Second, the asymmetry increases. For the undeflected data (Fig. 6.7c) the backward-forward ratio is 63/37 and for the deflected data (Fig. 6.7d) it is 73/27. The TOF spectra for the elliptically polarized YAG (both 4:1 and 2:1 ratios) are essentially identical to the ones for the linearly polarized YAG.

Finally, a strong degree of orientation is achieved even with low intensity of the YAG pulse. The TOF spectra show a backward-forward asymmetry of 58/42 (Fig. 6.5 e) for the undeflected molecules, which increases to 67/33 (Fig. 6.5 f) for the deflected molecules.

NONADIABATIC ALIGNMENT

7.1 Introduction

Nonadiabatic or impulsive alignment has been explored in numerous studies of both linear, symmetric top and asymmetric top molecules [19, 32, 73, 123–126]. Alignment results from interference among the eigenstates forming the rotational wave packet. In the case of a linearly polarized, nonresonant laser pulse, the most polarizable molecular axis aligns along the polarization direction shortly after the pulse and at subsequent wave packet revivals. For linear molecules the revival pattern is perfectly periodic, as expected for a wave packet of discrete levels that corresponds to regular motion in the classical limit. Here, experimental observables exhibit alignment transients at integer multiples of the rotational period of the molecule, $T_{\text{rot}} = 1/(2B)$ (B is the rotational constant expressed in frequency units) and at fractions thereof. These transients are termed rotational revivals. Symmetric top molecules also have discrete regular spectra and exhibit similar revival patterns, although having an additional structure, due to the availability of two rotation axes. Asymmetric top molecules display much more interesting rotational dynamics, due to the irregularly spaced energy level structure.

In this chapter (and thesis) the studies are restricted to linear molecules. Nonadiabatic alignment is demonstrated for carbondisulfide (CS_2) and car-

bonylsulfide (OCS) molecules. For the later, it is demonstrated how selecting the molecules in the lowest rotational quantum-states leads to great enhancement of nonadiabatic alignment.

7.2 Experimental Setup

A gas mixture of ~ 20 mbar CS_2 and up to 100 bar He or ~ 10 mbar OCS and 10 bar Ne is expanded supersonically into vacuum. Experiments on CS_2 were conducted in the "old" vacuum chamber system, hence after the supersonic expansion the molecular beam enters the detection chamber through a 1 mm skimmer. In case of OCS the molecular beam is skimmed twice before passing through the electrostatic deflector and capacitor plates. In the interaction region the molecular beam is crossed at 90° by two pulsed, 800 nm, focused laser beams: the first to align the internuclear axis and the second to Coulomb explode the CS_2 or OCS molecules. The alignment pulse (0.3-0.5 ps) creates a coherent superposition of rotational states, i. e. a rotational wave packet, in each molecule. As a result the spatial orientation of the internuclear axis with respect to the alignment pulse polarization becomes time dependent. The spatial orientation is measured by Coulomb exploding the molecules using time delayed 30 fs pulses and recording the direction of the S^+ ions for both molecules.

7.3 Results and Discussion

7.3.1 Nonadiabatic Alignment of Carbondisulfide

To characterize the alignment dynamics of carbondisulfide, S^+ ion images were recorded every 0.33 ps in the interval 0-165 ps, corresponding to the temporal delay of the probe pulse with respect to the center of the alignment pulse. To quantify the degree of alignment, the value of $\langle \cos^2 \theta_{2D} \rangle$ is calculated at each position from the angular information of the S^+ ion images. The calculations are restricted to the radial range corresponding to S^+ ions created from double ionization of CS_2 through the $\text{S}^+ + \text{CS}^+$ fragmentation channel. The polarization of the probe beam was chosen to be perpendicular to the plane of the detector. The reason for choosing this particular geometry is that it is unbiased in the plane of the detector and hence, corresponds to a circular symmetric ion image for randomly oriented CS_2 molecules. In this probe geometry an isotropic distribution corresponds to $\langle \cos^2 \theta_{2D} \rangle = 0.50$. The polarization of the alignment beam is parallel to the detector leading to values of $\langle \cos^2 \theta_{2D} \rangle$ equal to 1 and 0 for perfectly aligned and perfectly anti-aligned molecules, respectively. For CS_2 the rotational constant is $B = 3.268$ GHz. Therefore a full revival of the rotational wave packet

is expected at $1/2B = 153.0$ ps. Figure 7.1 shows a long time scan covering the first full rotational period. Immediately after the alignment pulse the molecular ensemble aligns. This alignment, often referred to as the post-pulse or prompt alignment and encountered for by the δ -kick model, only lasts for at short time period before the wave packet de-phases. At longer time delays a re-phasing of the rotational wave packet is observed, hence the transients centered at 38, 77, 115 and 154 ps are identified as the quarter, half, three-quarter and full rotational revivals respectively. In between the the rotational transients the wave packet reaches a permanent level of alignment corresponding to $\langle \cos^2 \theta_{2D} \rangle \sim 0.6$ that is not representative of an orientationally isotropic distribution of molecules as discussed above. This permanent degree is due to the lack of molecules rotating in the plane perpendicular to the field vector of the alignment beam. Hence, confining the angular momentum of the molecules to the plane perpendicular to the polarization of the alignment pulse, the alignment pulse creates an anisotropic distribution of M states in the rotational wave packet. The appearance of full revivals as the rotational wave packet evolves is expected, however, to explain the observation of quarter and half revivals we need to address the nature of the molecule.

CS_2 is a triatomic molecule with sulfur atoms placed at each end. Sulfur nuclei are spin-0 bosons. Pauli's exclusion principle states that; when two identical bosons are exchanged the overall wave function must remain unchanged. During a 180° -rotation the two identical S nuclei are interchanged, however the rotational wave functions change sign by $(-1)^J$, hence, nuclear spin statistics implies that only even J states in CS_2 are permitted and therefore populated.

Both half and quarter revivals are expected for linear molecules with only every second rotational states populated. Although weak, transients are also observed at one eighth of the rotational period. The explanation for this lies in the projection of the full three-dimensional distribution onto the two-dimensional plane of the detector, causing different selection rules for $\langle \cos^2 \theta \rangle$ and $\langle \cos^2 \theta_{2D} \rangle$ and hence allowing revivals to occur at other fractions of the rotational period for the projection onto the detector plane [127]. In Fig. 7.1 (b) expanded views of the prompt alignment, the quarter, half, three-quarter and full rotational revival are shown for 5 and 60 bar of He backing pressure. This illustrates the effect of high and low rotational temperatures. In our experiments a high degree of alignment is required, therefore optimum rotational cooling is needed. The position of the highest degree of field-free alignment was identified as the peak of the half J the half revival. We discovered that by turning down the intensity of the alignment pulse to 2.9×10^{12} W/cm² the alignment dynamics became slower, as expected, but furthermore the alignment degree at the peak of the half revival actually increased. The degree of alignment at the peak of the half J revival reached a maximum of $\langle \cos^2 \theta_{2D} \rangle = 0.76$.

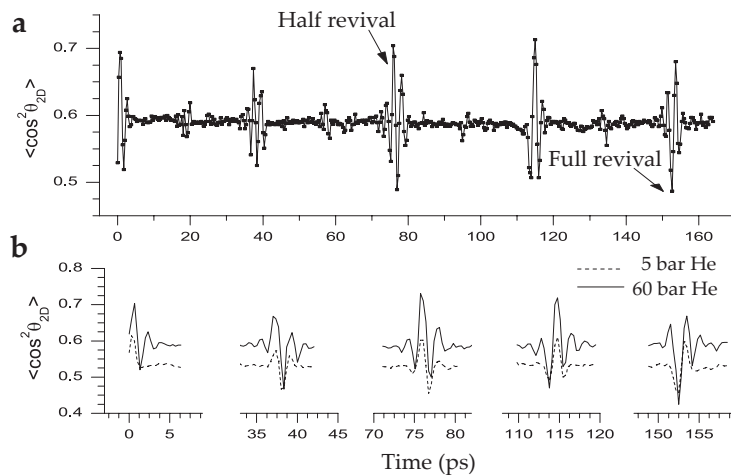


Figure 7.1: Alignment dynamics of CS_2 , quantified by $\langle \cos^2 \theta_{2D} \rangle$, as a function of time after the peak of the alignment pulse. (a) Long time scan covering the first full rotational period (153 ps). The alignment pulse duration was 0.5 ps, and the intensity was $1.1 \times 10^{13} \text{ W/cm}^2$. (b) Expanded views of the prompt alignment and some fractional revivals for 5 and 60 bar of He backing pressure, corresponding to high (dashed lines) and low (full lines) rotational temperatures, respectively. The laser pulse duration was 0.3 ps, and the intensity $1.1 \times 10^{13} \text{ W/cm}^2$.

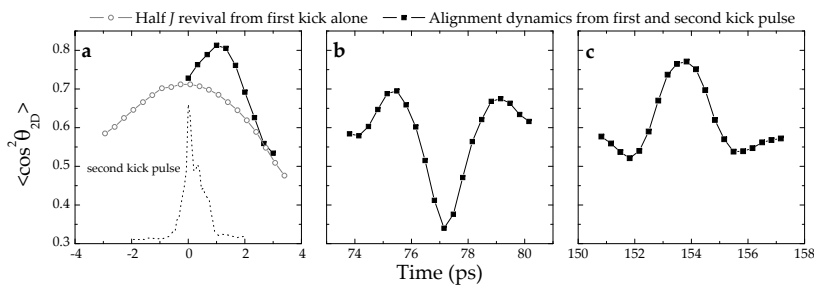


Figure 7.2: Alignment dynamics of the prompt alignment (a), half J (b) and full J (c) revival followed by the second kick pulse of a two pulse sequence. In the first panel the crosscorrelation trace of the second alignment pulse is displayed. Both pulses were 0.5 ps long. The first pulse had an intensity of $1.1 \times 10^{12} \text{ W/cm}^2$. At the time-delay of the first half J revival the second pulse, with an intensity of $3.0 \times 10^{12} \text{ W/cm}^2$ was sent in.

It is clear that obtaining a high degree of field-free alignment is essential. The degree of alignment obtained in adiabatic alignment experiments by far exceeds that of nonadiabatic alignment. An explanation can be found in the δ -kick model. In Sec. 2.4.1 it was illustrated why nonadiabatic alignment with a single pulse cannot provide the same high degree of alignment as adiabatic alignment. No matter how hard the molecules are kicked the ones originally at large angles with respect to the laser polarization will always lag behind, i. e. fail to align at the same time as the remaining molecules. To improve the degree of alignment the idea of using multiple pulses was proposed by Averbukh and Leibscher [66–68]. Experimental as well as numerical studies have shown that the strongest degree of one-dimensional field-free alignment obtainable with a single pulse can be enhanced using a two-pulse sequence in a parallel polarization geometry [128, 129]. The idea is that the first pulse prealigns the ensemble of molecules, i. e. enhances the number of molecules situated at small angles prior to the kick of the second pulse. Experiments were performed using a two-pulse sequence of parallel polarization. Both pulses were 0.5 ps long. The first pulse had an intensity of 1.1×10^{12} W/cm². At the time-delay of the first half J revival the second pulse, with an intensity of 3.0×10^{12} W/cm² was sent in. The alignment dynamics following the second kick pulse is displayed in Fig. 7.2. As seen from Fig. 7.2 the two pulse sequence inverts the dynamics observed from one-pulse alignment. Hence, anti-alignment or planar alignment is observed at the half J revival, and alignment at the full revival. The best degree of alignment was obtained just 1 ps after the second alignment pulse, reaching an alignment degree of $\langle \cos^2 \theta_{2D} \rangle = 0.81$.

7.3.2 Nonadiabatic Alignment of Carbonylsulfide

To demonstrate the effect of quantum-state-selection on nonadiabatic alignment, the half J revival of OCS molecules was characterized at different positions in the vertical molecular pulse profile (Fig. 7.3) for the deflector turned on at 7 kV as shown in Fig. 5.1. To characterize the dynamics S^+ ion images were recorded every 0.27 ps with respect to the center of the alignment pulse. At each position $\langle \cos^2 \theta_{2D} \rangle$ values were calculated from the angular information of the ion images. Similar to the measurements in Sec. 5.3 the calculations were restricted to the radial range corresponding to the $S^+ + CO^+$ fragmentation channel.

The rotational constant of OCS is $B = 6081.5$ MHz, therefore a full J revival is expected at $T = 1/(2B) = 82.2$ ps. As for CS_2 strong alignment is expected at the half J revival ($T = 41.1$ ps). Strong enhancement in the degree of alignment is observed as the foci of the lasers are moved from the depleted to the strongly deflected region. The maximum degree of alignment obtained at the peak of the J revival for deflected molecules corresponded to $\langle \cos^2 \theta_{2D} \rangle = 0.84$.

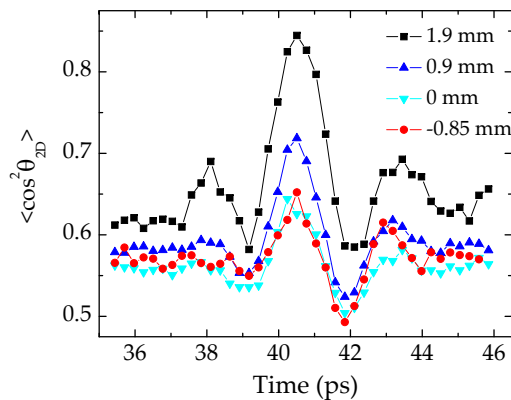


Figure 7.3: Alignment dynamics around the half J revival of OCS for different lens positions, quantified by $\langle \cos^2 \theta_{2D} \rangle$, as a function of time after the peak of the alignment pulse. The alignment pulse duration was 0.5 ps, and the intensity was $8.3 \times 10^{12} \text{ W/cm}^2$. The intensity of the probe pulse was $4.6 \times 10^{14} \text{ W/cm}^2$. For all traces the deflector was turned on a 7 kV, and the capacitor plates were at a potential difference of 500 V.

It should be noted, that the possibility to obtain orientation in the non-adiabatic regime also was investigated. However, at the amplitudes of the static field employed here, experiments revealed no evidence of molecular orientation.

Part II

PHOTOELECTRON ANGULAR DISTRIBUTIONS FROM ALIGNED AND ORIENTED MOLECULES

8

INTRODUCTION TO PHOTOELECTRON ANGULAR DISTRIBUTIONS

One of the fundamental tasks in physics and chemistry is the study of molecular structure and the observation of its evolution in time. The combination of photoelectron spectroscopy and ultrafast light sources is on track to set new standards for detailed interrogation of dynamics and reactivity of molecules [40, 41, 130–134]. A crucial prerequisite for further progress is the ability to not only detect the electron kinetic energy as has been done in traditional photoelectron spectroscopy over decades, but also to measure the photoelectron angular distributions (PADs) in the molecular frame [39–41, 130, 134–137]. Different approaches can be taken to obtain molecular frame photoelectron angular distributions (MFPADs). At wavelengths in the XUV or X-ray (from a synchrotron) or vacuum ultraviolet (VUV) range (from a frequency upconverted laser), single photon ionization can illuminate molecules from "within" [136]. At these wavelengths photoelectrons are produced by ionization of a core orbital, leaving the molecule in a highly excited state that decays quickly. In these types of experiments ionization is often followed by rapid disassociation of the molecule. Until recently the only method for extracting MFPADs relied on determining the orientation of the molecular frame after ionization by detecting molecular fragments in coincidence with the photoelectrons [130, 138–141]. This is, how-

ever, only possible if ionization leads to fragmentation thereby limiting both the species and the specific processes that can be studied. In the limit of multiphoton or tunneling ionization, characteristic for irradiation with strong laser fields, the highest occupied molecular orbital (HOMO) is most efficiently ionized, thereby creating (ground-state) ions that are often stable against dissociation. Hence, the alignment of the molecules prior to ionization is imperative for gaining access to MFPADs in strong laser fields. Combining strong field single ionization with the recent advances in the ability to control not only the alignment but even the orientation of gas phase molecules, may also provide more insight into strong-field ionization mechanisms. Single ionization of molecules by linearly polarized laser pulses is a fundamental process and the key step to understanding other strong field phenomena [142, 143], such as above threshold ionization (ATI), double ionization and high harmonic generation (HHG). Strong field physics has emerged as a field of great interest over the past few years as it has opened the opportunity to image molecular orbitals [38] and probing of nuclear dynamics with attosecond resolution [144].

The only demonstrations hitherto involved small linear unpolar molecules [39–41]. A decisive milestone is extension to the general class of polar molecules.

In the following sections I will provide an introduction to the fundamental processes and concepts involved in photoelectron spectroscopy studies and, additionally, highlight some historical milestones, preceding the experiments described in this part of the thesis, first in traditional photoelectron spectroscopy and finally in the strong field regime.

8.1 Traditional Photoelectron Spectroscopy

A photon can ionize a molecule if the energy of the photon exceeds the energy holding the electron to the molecule. In principle any energy above the ionization limit can lead to photoionization, with the excess energy being transformed into kinetic energy of the ejected electron and internal energy (electronic, vibrational and rotational) in the molecular ion. Due to conservation of energy

$$\hbar\omega = I_p + E_{kin,e^-} + E_{kin,ion} + E_{int} \quad (8.1)$$

where ω is the angular frequency of the laser field, I_p is the ionization potential of the molecule, E_{kin,e^-} and $E_{kin,ion}$ are the kinetic energies of the electron and parent ion, respectively and E_{int} is the energy associated with any excitation of internal degrees of freedom in the molecule. Due to the large difference in masses between the electron and the parent ion, the kinetic energy of the later is often neglected. The observables in any form of photoelectron spectroscopy experiment are the electron kinetic energy distributions and the photoelectron angular distributions (PADs).

In traditional photoelectron spectroscopy monochromatic light is used to photoionize the molecules. In this regime the photoelectron kinetic energies relates directly to the energy of the molecular orbitals involved in the photoionization. Over the last decades femtosecond time-resolved photoelectron spectroscopy has emerged as a powerful tool for investigations of photo-chemical and photo-physical problems studied in real time [145]. This evolution has been brought on by the advent of commercially available, broadly tunable femtosecond laser systems. Time resolved photoelectron spectroscopy is particularly well-suited for ultrafast non-adiabatic processes as it is sensitive to both electronic configurations, i. e. molecular orbitals, and to vibrational dynamics. Most time-resolved photoelectron spectroscopy (TRPES) experiments are basically pump-probe experiments studying excited state dynamics. The probe, typically a short visible or UV pulse excites the molecule, which is then at a variable delay probed by measuring the photoelectron kinetic energy spectrum originating from ionization by another UV pulse. A natural application of TRPES has been the study of excited state non-adiabatic couplings, involving the breakdown of the adiabatic (e.g. Born Oppenheimer) approximation [145]. The coupling between two electronically excited states is observed as the kinetic energies of the photoelectrons corresponding to ionization from the coupled states differ. The dynamics can then be followed by observing the evolution in the intensity of the different photoionization channels of the two coupled states [146].

As discussed previously the kinetic energy distributions are directly related to the molecular orbital energy, however, more information can be extracted from such measurements as the emission direction of the photoelectron, or to be precise the outgoing electron partial waves, contains information about the symmetry of the electronic state it was ejected from [147].

$$\Gamma_{\psi_f} \otimes \Gamma_{\mu} \otimes \Gamma_{\psi_i} \otimes \Gamma_{e^-} \ni \Gamma_{TS} \quad (8.2)$$

From Eq. (8.2) it is clear that if the symmetry of the initial state changes due to a non-adiabatic process the symmetry of the outgoing electron must also change. This is, however, only true when measured in the frame of the molecule. As most molecules are non-spherical most physical and chemical properties depend strongly on their relative orientation either in interactions with each other or with light. In the laboratory frame orientational averaging washes out, obscures or blurs the information contained in, for instance, the photoelectron angular distributions (PADs). Measuring PADs from fixed in space molecules has been a goal for researchers since the 1970s when it was first proposed by Dill [148] to be a *"much richer source of information on photoionization dynamics, being able to probe details "washed out" by the freely tumbling molecules of typical gas phase experiments"*.

Back then, as already introduced in Chapter 1, fixed-in-space molecules

could be obtained by techniques such as orienting molecules on surfaces (polymer films) or using molecular beam techniques. Since then a lot has happened.

One route to study molecular frame PADs is a recently developed technique based upon coincidence imaging spectroscopy of electrons and photofragment ions [130, 138–141]. In these type of experiments synchrotron radiation or UV laser pulses are used for ionization followed by rapid dissociation of the molecule. Measuring the recoil velocities of the electron and fragment ion in coincidence allows one to extract the full three-dimensional photoelectron angular distribution in the recoil frame using time and position sensitive detectors and hence, follow the dynamics of a photodissociation process along the entire reaction coordinate. This was demonstrated in 2006 by Geßner *et al.* on the dissociation of the NO-dimer [130].

A different approach to obtaining molecular frame PADs is to force alignment or orientation upon the ensemble of molecules onto the laboratory frame. This approach is brought on by recent advances in the ability to align gas phase molecules using short non-resonant, non-ionizing laser fields as described in Part I. Previously, the orientational resolution obtained from laser induced alignment did not match to the degree that can be extracted using coincidence techniques, however with recent improvements high degrees of alignment and even orientation are obtained, that are comparable to that extracted from coincidence measurements. These type of experiments presents the advantage of not requiring the molecule to be studied to dissociate when photoionized. Coincidence measurements rely on the axial recoil approximation of the molecular fragments and may be very difficult to generalize to more complex systems. However the two techniques do not exclude each other. Rather, to gain full insight the two techniques might complement each other.

In 2001 Suzuki and co-workers used a time resolved photoelectron imaging technique to study excited-state rotational wave packet dynamics in the S_1 state of pyrazine [149]. Photoelectron angular distributions resulting from two photon ionization of the S_1 state proved to be very sensitive to the orientation of the molecules in the excited state evolving wave packet, created by single photon ionization from the ground state. The experiments are in close resemblance with rotational coherence spectroscopy experiments, (initially demonstrated by Felker and Zewail in the 1990's [62]), as the alignment degree obtained in these experiments is very low compared to what can be achieved using strong non-resonant, non-ionizing laser fields. Low or not, the weak degree of alignment did lead to time-dependent anisotropic photoelectron angular distributions, hence effects are expected to become more pronounced with a higher degree of alignment. Several theoretical studies imply that photoelectron angular distributions are indeed very sensitive to the alignment that can be created by a laser pulse [150–152].

The first demonstration of time resolved PADs on laser induced transiently fixed-in-space molecules was presented in 2009 by Bisgaard *et al.* on CS₂ molecules investigating the dynamics on the nonadiabatic photodissociation process followed by photo excitation at 200 nm. The experiment is the laser-induced-alignment equivalent of the coincidence-measurement based NO-dimer studies [130].

8.2 The Strong Field Approach

The advances in ultrafast intense laser technology has triggered a key interest in strong field phenomena and single ionization of molecules in the multiphoton or tunnel regime presents a different approach to obtaining photoelectron angular distributions and hereby gaining access to time dependent structural information.

Characteristic of strong field ionization is that the electron is born in the presence of an intense laser field [143]. For linearly polarized laser fields the electron is accelerated in the field and as the sign of the field reverses it can be driven back to re-collide with the molecular core, due to the oscillations of the field. The nature of the re-collision can lead to either elastic electron scattering, producing electrons with high kinetic energy, also referred to as above threshold ionization (ATI), inelastic scattering causing further ionization (double ionization) or recombination accompanied by emission of a highly energetic photon, known as high harmonic generation (HHG).

When atoms or molecules are submitted to intense laser fields multiphoton processes can occur. A multiphoton process involves the net absorption or emission of more than one photon in an atomic or molecular transition and requires relatively large radiation intensities. At high enough intensities the laser field become strong enough to compete with the Coulomb forces in controlling the dynamics of atoms and molecules.

To provide a simplified picture and gain more insight into the nature of strong field ionization the semiclassical 'recollision' model was proposed by Corkum [142] and Kulander and coworkers [153] in the early 90's. The model suggested that strong field processes at low frequencies proceed through three distinct steps. In the first step the bound electron is detached from its parent ion by tunneling or over-the-barrier ionization. After tunnel ionization the unbound electron is assumed to have zero kinetic energy and interacts mainly with the field. The dynamics is assumed to be essentially that of a free electron in the field described by classical mechanics. Hence, the electron is accelerated by the laser field and receives a linear drift momentum that only depends on the laser field strength and phase at the time of the tunneling. In the third step the elec-

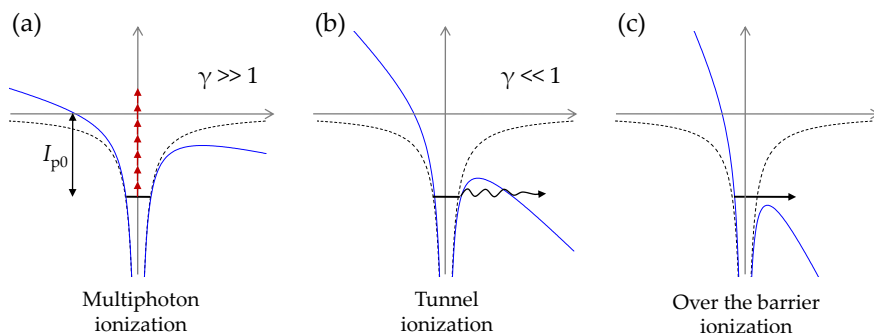


Figure 8.1: Strong field ionization regimes a, b and c show a schematic representation of the perturbation of an atomic Coulomb potential for the three main regimes involved in strong field ionization.

tron is accelerated back to re-collide with the core leading to different outcomes as mentioned above.

In light of the 3-step model the following subsections provide a more detailed description of the mechanisms involved in the distinct steps.

8.2.1 Ionization

The ionization step involved in strong field physics can be categorized into 3 main regimes depending on the laser field intensity and optical frequency.

At sufficiently low frequencies the ionization step can be viewed in the quasi classical picture. The key idea is that ionization occurs in a fraction of the optical cycle so that the electric field can be regarded as quasi static. An effective potential can be described as a superposition of the atomic or molecular potential and instantaneous laser field. At low intensities the ionization potential is only slightly perturbed and ionization can only occur through the net absorption of N photons, this regime is referred to as multiphoton ionization (See Fig. 8.1 a). As the intensity is raised the barrier becomes thinner and lower and eventually the bound electron can tunnel through the barrier, referred to as tunnel ionization (Fig. 8.1 b). Finally, at very high field strengths the electric field amplitude completely suppresses the Coulomb barrier below the energy level of the ground state leading to over-the-barrier ionization or barrier suppression ionization (Fig. 8.1 c).

A requirement for tunnel ionization to occur is that the barrier is lowered for sufficient time for the electron to escape the tunnel. If the optical frequency is

to high to qualify as being quasi static, ionization will occur in the multiphoton regime. It should be noted that the boundaries between the different regimes are floating. To quantify the regimes the Keldysh parameter was introduced in 1965 [154]. It is an approximate indicator as to the applicability of the tunneling model. The Keldysh parameter is related to the tunneling time and the optical period of the laser. The tunnel time is determined essentially by the mean free time of the electron passing through a barrier of width

$$l = \frac{I_p}{eE_0} \quad (8.3)$$

From the virial equation this leads to an average electron velocity on the order of $\sqrt{I_p/m_e}$, hence giving rise to a tunnel frequency of

$$\omega_t = \frac{eE_0}{\sqrt{2m_e I_p}} \quad (8.4)$$

The Keldysh parameter is defined as the ratio between the angular laser frequency and the tunnel frequency

$$\gamma = \frac{\omega}{\omega_t} = \frac{\omega\sqrt{2m_e I_p}}{eE_0} \quad (8.5)$$

where ω is the angular laser frequency.

For $\gamma \gg 1$, that is low intensity and short wavelength the ionization step is dominated by the simultaneous absorption of many distinct photons, hence multiphoton ionization. For $\gamma \ll 1$ tunnel ionization of the bound electron through a classical potential barrier provides the appropriate physical picture for the ionization process. The two regimes are not expected to be separated by a sharp transition and the intermediate regime with $\gamma \approx 1$ is expected to have contributions from both multiphoton and tunnel ionization. Experimentally this intermediate regime has, however, proved to be dominated by tunnel ionization [40, 142]. It has been referred to as the non-adiabatic tunneling regime and although the contribution from multiphoton ionization remains small in this regime the tunneling in this regime differs from the quasi static limit [155].

The question of how long time it takes for the electron to tunnel through the energetically forbidden region has been an issue of quite some debate. Does it happen instantaneously or does it take a finite amount of time. Recently, Keller and coworkers [156] shed some light on the matter with the first experimental measurement of an upper limit to the tunneling time on the orders of attoseconds, much lower than the previously assumed conventional transversal time for tunneling [157], indicating that there is no real tunneling delay time.

8.2.2 Propagation in the Field

After ionization the electron dynamics can be described using classical mechanics. In the simplest of models the electron dynamics are essentially those of a free electron in an electromagnetic field with the initial condition that the electron is born with zero kinetic energy. The resulting model is known as the simple man's model. Following the notation of Corkum *et al.* [142, 158] the electric field of a laser can be described as

$$\mathbf{E} = E_0 \varepsilon(t) (\cos(\omega t) \hat{\mathbf{e}}_z + \alpha \sin(\omega t) \hat{\mathbf{e}}_y) \quad (8.6)$$

where α allows for arbitrary polarization, with $\alpha = 0$ and $\alpha = 1$ corresponding to linearly and circularly polarized light, respectively. E_0 is the field strength, $\varepsilon(t)$ is the pulse envelope, $\hat{\mathbf{e}}$ is the unit vector in the field polarization direction and ω is the central frequency. In the nonrelativistic limit the electron will experience a force proportional to the electric field described by Newton's second equation

$$\mathbf{F} = m_e \frac{d\mathbf{v}}{dt} = -e\mathbf{E} \quad (8.7)$$

When neglecting the pulse envelope, the velocity of the electron in the field of the laser at time t is therefore

$$v_x = -\frac{e}{m_e} \int_{t_0}^t E_0 \cos(\omega t) dt = \frac{eE_0}{m_e \omega} (\sin(\omega t) - \sin(\omega t_0)) \quad (8.8)$$

$$v_y = -\frac{e}{m_e} \int_{t_0}^t \alpha E_0 \sin(\omega t) dt = -\frac{eE_0 \alpha}{m_e \omega} (\cos(\omega t) - \cos(\omega t_0)) \quad (8.9)$$

For a real laser pulse one should also include the pulse envelope in the above equations, however for simplicity it is neglected.

As a response to the applied electromagnetic field the electron is forced into a quiver or wiggling motion. The energy associated with this wiggling motion is referred to as the ponderomotive energy and for the electric field described in Eq. (8.6) it is given by the mean kinetic energy

$$U_p = \frac{1}{2} m_e \langle v^2 \rangle = (1 + \alpha^2) \frac{e^2 E_0^2}{4m_e \omega^2} \quad (8.10)$$

Note that the ponderomotive energy in this expression is dependent on the polarization state of laser pulse, however, this dependence disappears when it is expressed in terms of the peak intensity, where $I_0 = \frac{1}{2}(1 + \alpha^2)c\varepsilon E_0^2$

$$U_p = \frac{e^2 I_0}{2m_e \varepsilon_0 c \omega^2} \quad (8.11)$$

Expressing the Keldysh parameter first in terms of the peak intensity and secondly in terms of the ponderomotive energy gives

$$\gamma = \frac{\omega \sqrt{(1 + \alpha^2) \varepsilon_0 c}}{e} \sqrt{\frac{I_p}{I_0}} = \sqrt{\frac{(1 + \alpha^2) I_p}{2U_p}} \quad (8.12)$$

A consequence of Eq. (8.9) is that for circularly polarized light the electron trajectories can never return to interact with the parent ion. This is, however, not true for linearly polarized light, where the atom or molecule that undergoes ionization does not immediately become a well separated electron and ion, instead there is a significant probability of finding the electron in the vicinity of the ion for one or more laser periods.

8.2.3 Rescattering

In case of a linearly polarized laser field there is a significant probability within the first laser periods after ionization of recollision of the electron with the ion with very high kinetic energy leading to HHG, multiphoton two electron ejection and very high energy above threshold ionization electrons, all consequences of the electron-ion interaction. In this section I will focuss on above threshold ionization.

It was discovered in 1979 by Agostini *et al.* [159] that at sufficiently high intensities the ejected electron can absorb photons in excess of the minimum number required for ionization to occur. This phenomenon is called 'above threshold ionization' (ATI). The photoelectron spectra exhibited several peaks, separated by the photon energy and appearing at

$$E_{e^-} = (N + S)\hbar\omega - I_p \quad (8.13)$$

where E_{e^-} is the energy of the emitted electron, N is the minimum number of photons required for ionization, S is the number of excess photons absorbed and I_p is again the ionization potential of the atom or molecule.

Several observations were made from the ATI spectra. At high intensities peak suppression of the first ATI peaks is observed due to the energies of the atomic states being Stark shifted in the presence of a laser field. For low laser frequencies the AC Stark shifts of the lowest bound states are small in magnitude. However, the induced Stark shifts of the Rydberg and continuum states are essentially given by the electron ponderomotive energy U_p . With the upwards shift of the energies of the Rydberg and continuum states by about U_p compared to the lower lying states there is a corresponding increase in the intensity dependent ionization potential

$$I_p(I_0) \simeq I_p + U_p \quad (8.14)$$

When interpreting the ATI spectra one has to identify the regime in which the ionization takes place. For relatively long (picosecond) pulses the photoelectron escapes from the focal volume while the laser is still on. As the electron travels out of the inhomogeneous laser focus it experiences a force given by ∇U_p . The electron quiver motion is then converted into radial motion, increasing the kinetic energy by U_p and hence exactly canceling the decrease in energy caused by the (Stark shifted) increase in the ionization potential and Eq. (8.13) still applies. However, for short (sub-picosecond) pulses the laser field turns off before the photoelectron can escape from the focal volume resulting in a more complicated ATI spectrum. The observed photoelectron appear at distinct energies given by the values

$$E_{electron} = (N + S)\hbar\omega - I_p - U_p \quad (8.15)$$

relative to the shifted ionization potential. Photoelectrons produced at different spatial regions of the focal volume are emitted at different intensities and, thus, have different energies. Another phenomenon observed in strong field multiphoton ionization is termed Freeman resonances and first described by Buchsbaum and Freeman in the late 80's [160]. Freeman resonances result from different states of the atom or molecule being brought into multiphoton resonance during the laser pulse, by the intensity dependent Stark shift, resulting in substructure of the ATI peaks.

In the following chapters carbondisulfide (CS_2), carbonylsulfide (OCS) and benzonitrile ($\text{C}_7\text{H}_5\text{N}$) molecules, fixed in space by combined laser and electrostatic fields, are ionized with intense, linearly or circularly polarized, 30 femtosecond laser pulses. For 1-dimensionally aligned CS_2 the angular distribution of the photoelectrons exhibits a significant dependence on the angle between the polarizations of the aligning and ionizing laser fields. For 1-dimensionally oriented OCS the molecular frame PADs exhibit pronounced anisotropies, perpendicular to the fixed permanent dipole moment, that are absent in PADs from randomly oriented molecules. For 3-dimensionally oriented $\text{C}_7\text{H}_5\text{N}$ additional striking structures appear due to suppression of electron emission in nodal planes of the fixed electronic orbitals.

9

MULTIPHOTON IONIZATION OF LASER-ALIGNED CARBONDISULFIDE MOLECULES

In this chapter field-free aligned carbondisulfide (CS_2) molecules are singly ionized by multiphoton absorption from intense, linearly polarized 25 fs laser pulses. The angular distributions of photoelectrons exhibits a significant dependence on the angle between the polarizations of the aligning and ionizing laser fields. At time of the measurement it represented the first experimental evidence of the dependence of the photoelectron angular distributions (PADs) on the laser - field orientation [39]. Since then only few studies have been reported [40, 41].

The main observables in the experiments presented in this chapter are 2D PADs measured as a function of the angle between the polarization of the ionization pulse and the polarization of the alignment pulse, i. e. the internuclear axis of CS_2 . Prior to the photoelectron experiments the rotational dynamics following the alignment pulse is characterized by Coulomb explosion and subsequent velocity map imaging of the S^+ fragment ions. In this way optimum field-free alignment of the CS_2 molecules is ensured. The experimental details for achieving alignment are described in Sec. 7.3.1 of Chapter 7. Alignment is induced in the nonadiabatic (impulsive) regime using a 0.5 ps (FWHM) long pulse. When focussed to a spotsize of 51 μm it has a peak intensity of $2.9 \times 10^{12} \text{ W/cm}^2$. No

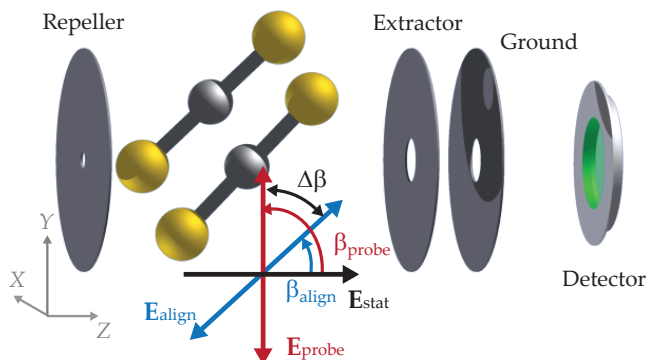


Figure 9.1: Schematic illustration of the polarization state of the alignment and the probe pulse with respect to the static electric field and the detector plane used to characterize alignment, including a sketch of the resulting molecular alignment. Repeller, extractor and ground refers to the electrostatic plates of the VMI spectrometer.

ionization is observed from this pulse alone. As described in the Chapter 7 the best degree of field-free alignment is identified to occur at the peak of the first half J rotational revival, ~ 76 ps after the peak of alignment pulse. At this position a degree of alignment corresponding to $\langle \cos^2 \theta_{2D} \rangle = 0.76$ is obtained. In the subsequent measurement the time delay between the alignment and probe pulses are kept fixed at ~ 76 ps. To create electrons the Coulomb explosion probe pulse (25 fs, $27 \mu\text{m}$) used for ion imaging is lowered to a peak intensity of $7.7 \times 10^{13} \text{ W/cm}^2$. At this intensity CS_2 primarily undergoes single ionization and dissociated fragment ions are barely visible in the time of flight spectrum of CS_2 , contributing no more than $\sim 4\text{-}5\%$ of the total ion signal.

The aligning and ionizing laser pulses are both linearly polarized. For all relative orientations the polarization of the ionizing pulse is kept polarized in the plane of the detector with $\beta_{\text{probe}} = 90^\circ$, i.e. along the laboratory fixed Y -axis, while the polarization of the alignment pulse (β_{align}) is controlled by rotating a half-wave plate situated in the beam path. A schematic illustration of the probe geometry is shown in Fig. 9.1.

Photoelectron images recorded at different relative orientations are displayed in Fig. 9.2 as a function of the vertical (p_Y) and horizontal momentum (p_X), parallel and perpendicular to the probe pulse, respectively. The images are recorded over 50000 laser shots and contain $2 - 5 \times 10^6$ electron hits. Image (a) is a reference image obtained from the probe pulse alone. In Fig. 9.2 (b)-(d) alignment is induced at different relative angles (b) $\Delta\beta = 0^\circ$, (c) $\Delta\beta = 45^\circ$ and (d) $\Delta\beta = 90^\circ$,

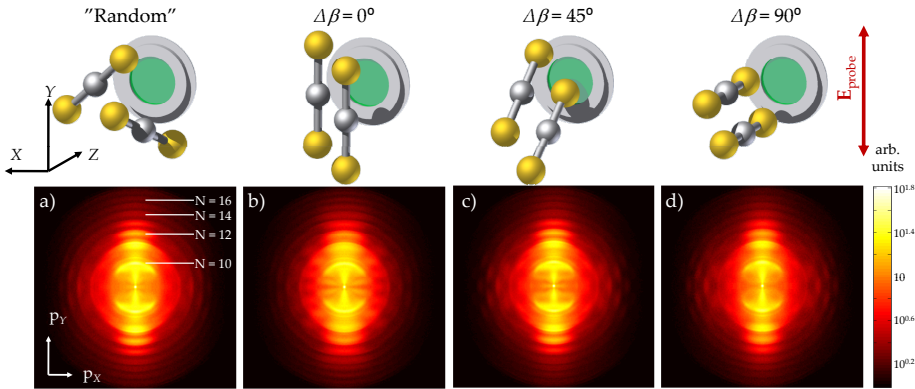


Figure 9.2: Two-dimensional photoelectron images as a function of the vertical momentum p_y and the horizontal momentum p_x from multiphoton ionization of (a) unaligned molecules and aligned molecules at an angle (b) $\Delta\beta = 0^\circ$, (c) $\Delta\beta = 45^\circ$ and (d) $\Delta\beta = 90^\circ$, where $\Delta\beta$ is the angle between the polarizations of the alignment and ionizing pulse. A ring structure is observed in the images corresponding to different above-threshold ionization (ATI) channels. N in (a) denotes the number of photon absorptions associated with the rings. The images have been symmetrized and are shown in a logarithmic color scale. The ionization pulse used to produce the photoelectron images has a peak intensity of $7.7 \times 10^{13} \text{ W/cm}^2$.

where $\Delta\beta = \beta_{\text{probe}} - \beta_{\text{align}}$ is the angle between the polarizations of the alignment and probe pulse.

The attention is first drawn to the radial structure observed in the images. The images exhibit well defined radial ring structures corresponding to the momenta of the electrons, i. e. the kinetic energy of the electrons, clotted around a series of discrete values.

In this context it is important to keep in mind that we cannot measure the full 3D distribution. What we measure is the projection onto the two dimensional detector plane. This limitation is imposed by the lack of any time resolution in our measurement scheme; the longitudinal component of the electron velocity remains unknown. The complete three-dimensional distribution can be reconstructed from the measured two-dimensional distribution by Abel inversion, however, only in cases where the distribution is cylindrically symmetric with the axis of symmetry parallel to the plane of the detector. Of the various conditions for which we make the measurements, this condition is satisfied only for two configurations - the ionization pulse must be polarized in the plane of the detector, and the molecules are either unaligned, or aligned along the polariza-

tion vector of the ionization pulse. The radial distribution of the Abel inverted unaligned image is shown in Fig. 9.3. Again, a well defined radial ring structure is observed.

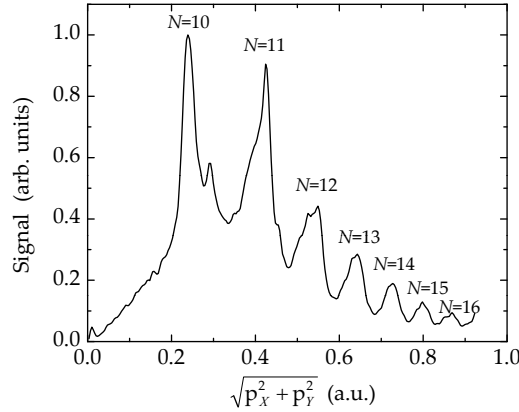


Figure 9.3: The radial distribution of the Abel inversion (Basex) of the unaligned image of Fig. 9.2 (a), displayed as a function of the electron momentum $\sqrt{p_x^2 + p_y^2}$.

To interpret the observations of the photoelectron images we need to account for the intensity effects connected with strong field ionization. A characteristic phenomenon observed in photoelectron spectroscopy in the multiphoton regime is above-threshold ionization (ATI), the absorption of additional photons by an electron already above the ionization potential leading to a series of peaks spaced by the photon energy. A further consequence of strong field ionization is the ac Stark effect, that shifts and modifies the potential energy surfaces during the strong electric field of the laser pulse, manifesting itself in terms of the induced ponderomotive potential (Eq. (8.10)).

The ponderomotive potential is connected with the wiggle motion of charged particles in response to an applied electromagnetic field of strength E_0 and frequency ω . This results in a red shift in electron kinetic energy and a broadening of the photoelectron spectrum. The ionization threshold of CS_2 is $I_p = 10.08$ eV and with a peak intensity of 7.7×10^{13} W/cm² of the 800 nm ionizing pulse the ponderomotive shift is 4.6 eV. The kinetic energy on an electron ionized by N photons is

$$E_{kin} = N\hbar\omega - U_p - I_p \quad (9.1)$$

The photon energy $\hbar\omega$ is 1.55 eV, leading to a minimum of 10 photons required to overcome the ionization threshold corresponding to the innermost pair of half rings in Fig. 9.2. Each of the subsequent pair of half rings in the progression at

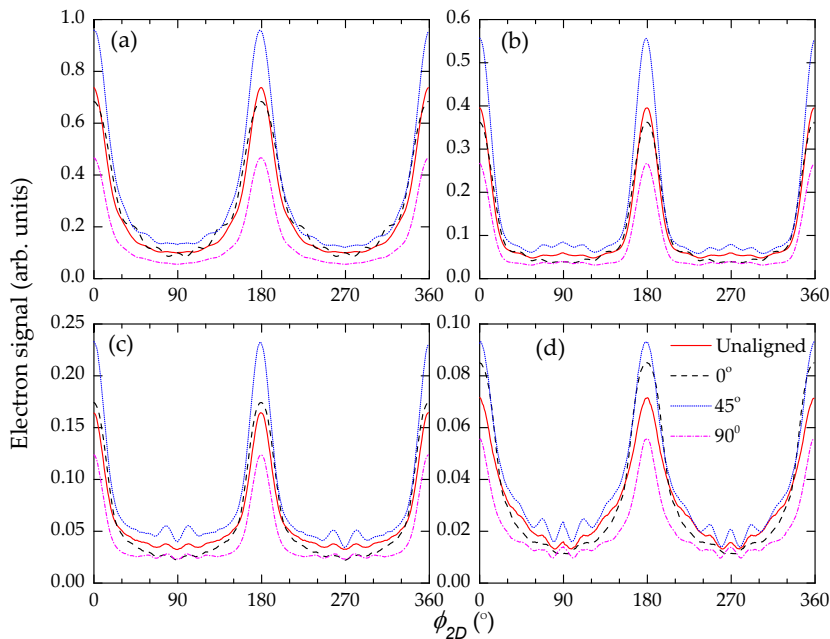


Figure 9.4: Experimental PADs for the (a) 11-, (b) 12-, (c) 13- and (d) 14-photon ionization channels extracted from the images in Fig. 9.2. In each panel the number of electrons recorded per laser pulse as a function of ϕ_{2D} are displayed, where ϕ_{2D} is the angle between the two-dimensional projection of the electron emission direction and the vertical ionizing pulse polarization.

larger radii result from absorption of additional photons. The peaks in the radial distribution of Fig. 9.2 and Fig. 9.3 are therefore identified as the absorption of $N = 10, 11, 12, \dots$ *etcetera* photons. A further observation is the very sharp radial substructure in the two innermost ring, corresponding to the lowest multiphoton orders. This is yet another intensity effect ascribed to Freeman resonances. Freeman resonances are due to Rydberg states brought into resonance by the ac Stark shift, giving rise to fine structure in the ATI spectra [145].

Next, the attention is turned towards the emission direction of the photoelectrons. As observed in the four images of Fig. 9.2 the bulk of the electron emission occurs along the polarization vector of the ionization pulse for all multiphoton absorption channels. Looking closer, however, structural differences are observed in the patterns for the different molecular alignment orientations of Fig. 9.2 (b)-(d). The differences are most easily observed for electrons in the outermost rings emitted perpendicular to the polarization of the probe pulse,

i. e. along the X -axis. The differences are especially pronounced when the parallel geometry is compared to the perpendicular geometry, i. e. comparing Fig. 9.2 (b) and (d).

To quantify the dependence of the electron emission on the relative orientation, $\Delta\beta$, photoelectron angular distributions (PADs) at the different $\Delta\beta$'s for each individual multiphoton channel by integrating radially over the corresponding pair of half rings in the images. The results, represented as the number of electrons recorded per laser pulse versus ϕ_{2D} , where ϕ_{2D} is the angle between the 2D projected electron ejection direction and the vertical ionizing pulse polarization, are displayed in Fig. 9.4 for the (a) 11-, (b) 12-, (c) 13- and (d) 14-photon ionization channels extracted from the images in Fig. 9.2, corresponding to no alignment pulse and $\Delta\beta = 0^\circ, 45^\circ$ and 90° . The angular resolution is better than 10 degrees. For each ATI channel in Fig. 9.4 a strong dependence on the magnitude of the electron signal upon the orientation of the molecules is observed. The $\Delta\beta = 45^\circ$ geometry provides the largest and $\Delta\beta = 90^\circ$ the smallest signals. These observations are consistent with measurements, based on detection of ion yield of intense-laser single ionization of the carbondioxide (CO_2) molecules in 2007 [161], where the ionization probability as a function of alignment angle was studied. The highest occupied molecular orbital (HOMO) of CO_2 has Π_g symmetry similar to CS_2 .

The PADs do not only differ in the overall signal, the PADs change qualitatively between the different orientations for electrons centered around 90° or 270° (i. e. along the X axis). Focussing for instance on the the 12-photon channel Fig. 9.4 (b) a local maximum is observed in the PAD around 90° and 270° for $\alpha = 45^\circ$, whereas the PAD recorded for $\alpha = 90^\circ$ exhibits a global minimum. Similar differences between the angular distributions recorded at different orientations are observed for higher order photon (ATI) channels.

To accompany our experimental results numerical calculations are performed using the Strong Field Approximation (SFA) by our collaborators in the theoretical group of Lars Bojer Madsen^a. For a detailed description of the theoretical model the reader is referred to [39]. The calculations are performed using the laser pulse parameters identical to the experimental values. Furthermore the results include an averaging over the focal volume of the ionizing pulse and the initial rotational temperature is taken to be 2 K. The results of the numerical calculations are shown in Fig. 9.5.

Angular distributions corresponding to the 11-, 12-, 13- and 14-photon absorption channels are displayed in Fig. 9.5. The results in the figure show a qualitative agreement with the experiment with minima at $\phi_{2D} = 90^\circ$ (270°) and maxima around $\phi_{2D} = 0^\circ$ (180°), but the detailed modulation differs some-

^aLundbeck Foundation Theoretical Center for Quantum System Research, Department of Physics and Astronomy, Aarhus University, Denmark

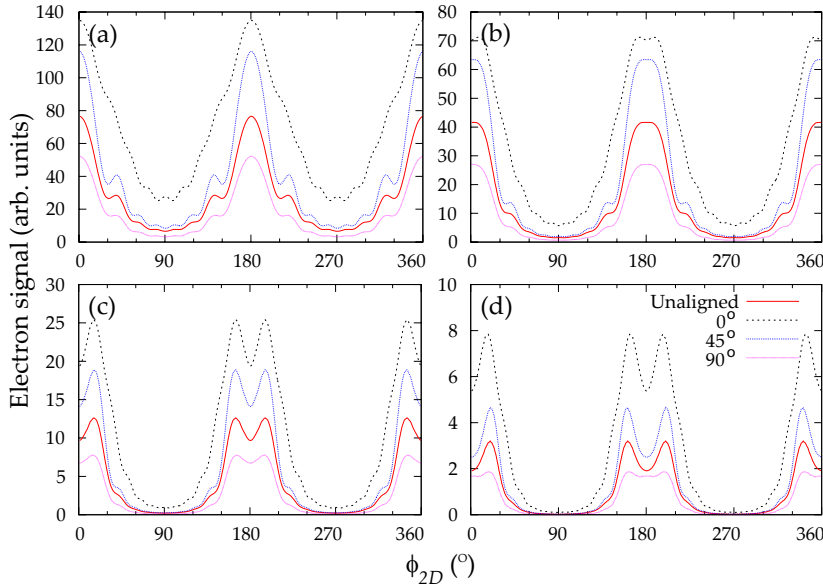


Figure 9.5: Calculated PADs using laser pulse parameters identical to the experimental values. (a)-(d) represent the signals obtained by integrating the $dP = dp_Y dp_X$ distribution over the circular areas identified as different ATI channels. The different curves correspond to the unaligned, $\Delta\beta = 0^\circ$, $\Delta\beta = 45^\circ$, and $\Delta\beta = 90^\circ$ geometries as detailed by the legends in (d). For ease of comparison, we have scaled the $\Delta\beta = 90^\circ$ alignment by a factor of 3.

what in size and shape from the experimental observations. At a quantitative level, on the other hand, there are significant differences. In the experimental data there is typically a factor of 8 between the minimum and the maximum in each PAD, whereas in the theoretical result this factor is $\sim 5.9 - 8.1$ in the 11-, $\sim 11.5 - 38.0$ in the 12-, $\sim 20.0 - 77.0$ in the 13- and $\sim 46.0 - 85.0$ in the 14-photon absorption channel. In general the theoretical model overestimates the ϕ_{2D} dependence. The calculations also differ from the experimental measurements in the magnitudes of the electron signals. Theory predicts the ionization yield to decrease in the order of $\Delta\beta = 0^\circ, 45^\circ$, unaligned and 90° . In the experimental data this is not the case as the order is 45° , unaligned, 0° , and 90° for the 11- and 12- photon absorption channels while it is $45^\circ, 0^\circ$, unaligned, and 90° in the 13- and 14-photon absorption channels. Several possible reasons for the discrepancy between the measurements and the predictions of the SFA have been investigated by the theoreticians. They believe that the discrepancy is associated

with the excited state spectrum of the CS₂ molecule and possibly with the final state Coulomb interaction, none of which are accounted for in the SFA.

There is reason to believe that high-lying Rydberg states could change the outcome of the calculations as intermediate Rydberg resonances are observed in our experimental data, hence indicating a similar strong influence of excited states. Unlike atoms, however, no standard approach exists for calculating the excited electronic states of molecules even in a simple system like CS₂. The ability to align a molecular ensemble prior to the interaction with an intense femtosecond laser pulse presents new challenges for theory in the description of even the first ionization step.

To investigate the photoelectron angular distribution from aligned molecules even further a series of measurements were performed under similar conditions as described above, however, in these experiment the intensity of the ionizing laser pulse was lowered to a peak intensity of 4.1×10^{13} W/cm². Again, alignment was created using a 0.5 ps (FWHM) long pulse, focussed to a spotsize of 51 μ m with a peak intensity of 2.9×10^{12} W/cm². No ionization is observed from this pulse. The ionizing laser pulse is fixed at a time delay between the aligning and ionizing laser pulses of ~ 76 ps. The 25 fs (FWHM) ionizing pulse is focussed to a spotsize of 27 μ m and has a peak intensity of 4.1×10^{13} W/cm². At this intensity CS₂ only undergoes single ionization and no dissociated fragment ions are observed in the time of flight spectrum of CS₂.

Photoelectron images recorded at different relative orientations of the aligning and ionizing laser pulses are displayed in Fig. 9.6. The images are recorded over 150000 laser shots (200000 laser shots for $\Delta\beta = 90^\circ$) and contain $1.5 - 2.5 \times 10^6$ electron hits. Image (a) is a reference image obtained from the ionization pulse alone. In Fig. 9.2 (b)-(d) alignment is induced corresponding to different angles (b) $\Delta\beta = 0^\circ$, (c) $\Delta\beta = 45^\circ$ and (d) $\Delta\beta = 90^\circ$.

As observed for the measurements at higher ionization intensity the images of Fig. 9.6 display a well defined radial ring structure. Compared to Fig. 9.2 fewer radial rings are observed in Fig. 9.6, consistent with the lower intensity applied. Furthermore it should be noted that lowering the intensity also diminishes the affect of the ponderomotive potential, which for the intensity of $I_0 = 4.1 \times 10^{13}$ W/cm² reduces to 2.49 eV, hence lowering the minimum number of photons required for ionization to 9 photons. Lowering the intensity of the probe changes the Keldysh parameter from $\gamma = 1.05$ in the previous to $\gamma = 1.42$ in the present study. As a consequence ionization is extended further into the multiphoton regime. In the images of Fig. 9.6 this is visible as a sharpening and even more well-defined radial ring structure. Similar to Fig. 9.2 changes are observed in the structure of the angular distribution for different angles $\Delta\beta$. The differences are particularly pronounced for electrons in the outermost rings emitted perpendicular to the polarization of the probe pulse, i. e. along the X -

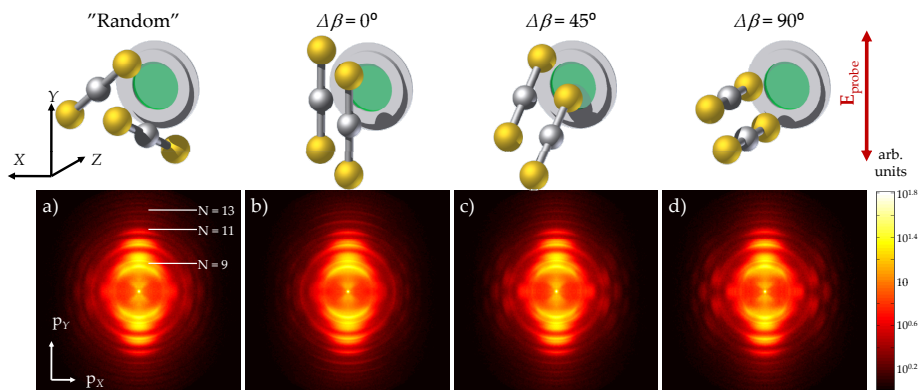


Figure 9.6: Two-dimensional photoelectron images as a function of the vertical momentum p_y and the horizontal momentum p_x from multiphoton ionization of (a) unaligned molecules and aligned molecules at an angle (b) $\Delta\beta = 0^\circ$, (c) $\Delta\beta = 45^\circ$ and (d) $\Delta\beta = 90^\circ$, where $\Delta\beta$ is the angle between the polarizations of the alignment and ionizing pulse. A ring structure is observed in the images corresponding to different above-threshold ionization (ATI) channels. The images have been symmetrized and are shown in a logarithmic color scale. The ionization pulse has a peak intensity of $4.1 \times 10^{13} \text{ W/cm}^2$.

axis.

In an attempt to enhance the orientational contrast of the photoelectron measurements the molecular alignment was enhanced. It is clear that obtaining a high degree of field-free alignment is essential.

Molecular alignment was enhanced using a two pulse sequence of parallel polarization as described in Chapter 7. Both pulses were 0.5 ps long. The first pulse had an intensity of $1.1 \times 10^{12} \text{ W/cm}^2$. At the time-delay of the first half J revival the second pulse, with an intensity of $3.0 \times 10^{12} \text{ W/cm}^2$ was sent in. The alignment dynamics following the second kick pulse was displayed in Fig. 7.2. As seen from Fig. 7.2 the two pulse sequence inverted the dynamics observed from one-pulse alignment. Hence, anti-alignment was observed at the half revival, and alignment at the full revival. The best degree of alignment was obtained just 1 ps after the second alignment pulse, reaching a $\langle \cos^2 \theta_{2D} \rangle$ of 0.81. At this position a series of photoelectron images were recorded from single ionization in the multiphoton regime using a 25 fs (FWHM) laser pulse with a peak intensity of $3.7 \times 10^{13} \text{ W/cm}^2$. The results are displayed in Fig. 9.7. An enhancement of the orientational contrasts in the PADs is observed. It could be argued that the measurements were performed under conditions that were

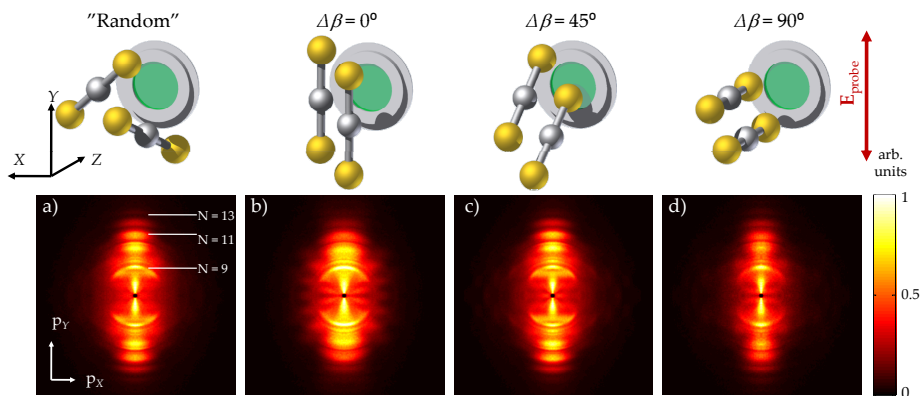


Figure 9.7: Two-dimensional photoelectron images from multiphoton ionization of (a) unaligned molecules and two-pulse aligned molecules at an angle (b) $\Delta\beta = 0^\circ$, (c) $\Delta\beta = 45^\circ$ and (d) $\Delta\beta = 90^\circ$, where $\Delta\beta$ is the angle between the polarizations of the alignment and ionizing pulse. The images have been symmetrized and are shown in a color scale. The ionization pulse used to produce the photoelectron images has a peak intensity of $3.7 \times 10^{13} \text{ W/cm}^2$.

not completely field-free, however, instabilities in our experimental setup at the time of acquisition, prevented us from fully exploiting the enhanced two-pulse alignment and the results should be viewed as preliminary. The strong contrasts do, however, encourage further investigations.

10

MFPADS FROM TUNNEL IONIZATION OF CARBONYLSULFIDE

In this section carbonylsulfide (OCS) molecules are fixed in space by the combined action of laser and electrostatic fields, prior to ionization with intense circularly or linearly polarized, 30 fs laser pulses. When measured in the molecular frame of the 1-dimensionally oriented OCS molecules the photoelectron angular distributions (PADs) exhibit pronounced anisotropies that are absent in PADs from randomly oriented molecules.

10.1 Circular Polarized Probe Beam

Experimentally a target of adiabatically aligned and oriented molecules is created by the combined action of a 10 nanosecond laser pulse and a weak static electric field. Before reaching the interaction point with the laser pulses and the static field the molecules are selected in the lowest-lying rotational quantum states by our electrostatic deflector. Hereby alignment and orientation is optimized, which is crucial for observation of the molecular frame photoelectron angular distribution (MFPAD) effects discussed next. The degree of alignment and orientation is initially measured by Coulomb exploding the molecules by an intense femtosecond (fs) probe laser pulse as described in Chapter 5.

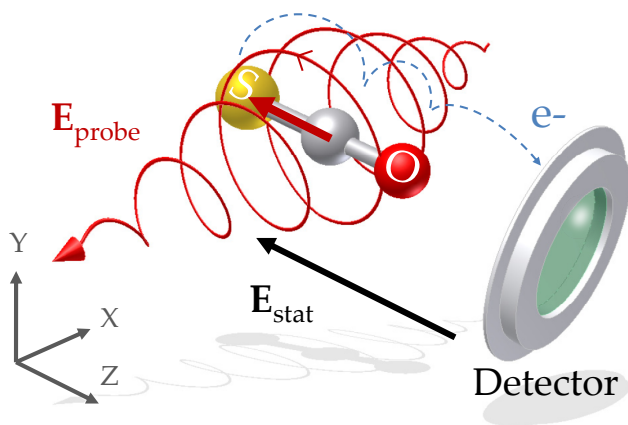


Figure 10.1: Schematic of the experimental setup used to produce photoelectron images showing an OCS molecule oriented with its permanent dipole moment (bold red arrow) pointing in the direction of the static electric field. The LCP probe pulse ionizes the molecule and imparts an upward momentum to the freed electron resulting in recording on the upper part of the detector (see text for details).

To obtain MFPADs the same experimental setup used to measure the degree of alignment and orientation as described in Sec. 5.3 is used, but several important changes are imposed. The 30 fs probe pulses are still applied, however, the polarization is changed from linear to circular and the intensity is lowered to a peak intensity of $\simeq 2.4 \times 10^{14} \text{ W/cm}^2$. At this intensity OCS only undergoes single ionization with essentially no fragmentation. The intensity puts the dynamics in the tunneling regime [154] with $\gamma = 0.89$ and the circular polarization ensures that no recollision of the freed electron with its parent ion occurs. Both conditions are important for the interpretation and modeling of the observed PADs.

In Fig. 10.1 the key idea of the experiment is illustrated. An OCS molecule is ionized by a left circularly polarized (LCP) pulse. The linear polarization of the alignment laser is parallel to the static field axis. To extract electrons instead of ions in the PAD measurements the polarity of the velocity map imaging spectrometer is inverted. Hereby, the OCS molecules are confined along the static field axis with the S-end facing the repeller electrode.

The resulting electron images are shown in Fig. 10.2. With only the probe pulse (Fig. 10.2a and b) the electrons emerge in a stripe parallel to the polarization plane (Y, Z) of the probe pulse. The images are up-down symmetric and the marginal difference between the images obtained with left and right circu-

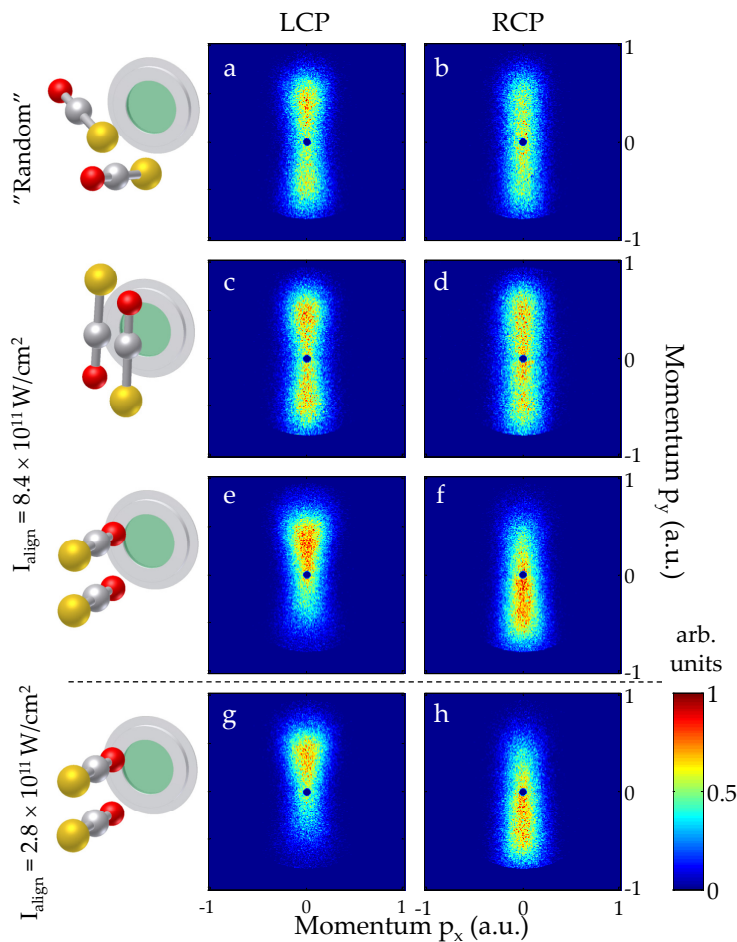


Figure 10.2: Two-dimensional momentum image of electrons produced when a randomly oriented sample of OCS molecules are ionized by the LCP (a) probe pulse. The polarization plane of the probe pulse is perpendicular to the image (detector). b, Same as a but for a RCP probe pulse. c, d, as a and b but with the OCS molecules aligned along the Y -direction by the alignment pulse polarized parallel to the image plane. e, f, as a and b but with the OCS molecules aligned along the Z -direction by the alignment pulse polarized perpendicular to the image plane. g, h, as e and f but with the intensity of the alignment pulse lowered from $I_{\text{align, YAG}} = 8.4 \times 10^{11} \text{ W/cm}^2$ to $I_{\text{align, YAG}} = 2.8 \times 10^{11} \text{ W/cm}^2$. The amplitude of the static field in these measurements is $E_{\text{stat}} = 345 \text{ V/cm}$.

larly polarized (LCP and RCP) pulses may be due to experimental imperfections in the purity of the polarization state and a weak orientation of the molecules caused by the static field alone. When the molecules are 1-dimensional (1D) aligned along the Y -direction the images are essentially unchanged and no up-down asymmetry is observed. When the alignment laser polarization is positioned along the Z -direction (see Fig. 10.1), a strong up-down asymmetry is observed (Fig. 10.2 d and e). The asymmetry reverses as the helicity of the probe pulses is flipped. For LCP (RCP) probe pulses the number of electrons detected in the upper part compared to the total number in the image is $\sim 64\%$ (39%). To investigate the influence of the aligning laser field on the PADs, similar measurements were performed at $1/3$ of the intensity as shown in image g and h. At this intensity the degree of orientation is only slightly changed and the images appear to be almost unchanged compared to before, hence, decreasing the field strength of the aligning laser does not seem to influence the electron trajectories and we conclude that no error in the measurements is introduced by the presence of the aligning laser field. The number of electrons detected in the upper part compared to the total number in image g (h) is $\sim 66\%$ (38%).

Prior to the PAD measurements, ion imaging measurements equivalent to the experiments presented in Chapter 5 reveal that the OCS molecules are strongly oriented along \mathbf{E}_{stat} . The ion imaging method described in Chapter 5 is, however, not applicable when the molecules are aligned along \mathbf{E}_{stat} because all S^+ ions will collapse in the center of the detector. As an alternative we note that $E_{\text{stat}} = 345 \text{ V/cm}$ in the PAD measurements. This value falls in between the value of the effective static field, i. e. \mathbf{E}_{stat} along the OCS bond axis, of Fig. 5.7 a and b ($\sim \cos(45^\circ) \times 345 \text{ V/cm} = 244 \text{ V/cm}$) and Fig. 5.7 c and d ($\sim \cos(45^\circ) \times 595 \text{ V/cm} = 420 \text{ V/cm}$) in Chapter 5. In the former (latter) case the orientation corresponds to a 73% (80%) up-to-total ratio. Therefore, the orientation degree in the PAD experiment geometry should be at least $77 - 78\%$. Although this neglects quantum mechanical coupling effects of the two fields [24], it provides a good approximation of the degree of orientation in the PAD measurements. The vertical probe geometry applied in Fig. 5.7 does, however, underestimate the degree of orientation, because the probe pulse preferentially ionizes (probes) the molecules aligned along its vertical polarization axis where the static field is zero and the molecules are not oriented. As a consequence, in the PADs measurements a degree of orientation is estimated to about 80% of the molecules having their O-end facing the detector and 20% facing oppositely.

To investigate the influence of the intensity of the ionizing laser pulse, measurements at three different intensities were performed. Figure 10.3 shows the electron images obtained with a left circular polarized (LCP) pulse. In a, d and g only the probe pulse is included for increasing intensity of the ionization pulse corresponding to $I_{\text{probe}} = 1.76 \times 10^{14} \text{ W/cm}^2$ in a, $I_{\text{probe}} = 2.44 \times 10^{14} \text{ W/cm}^2$

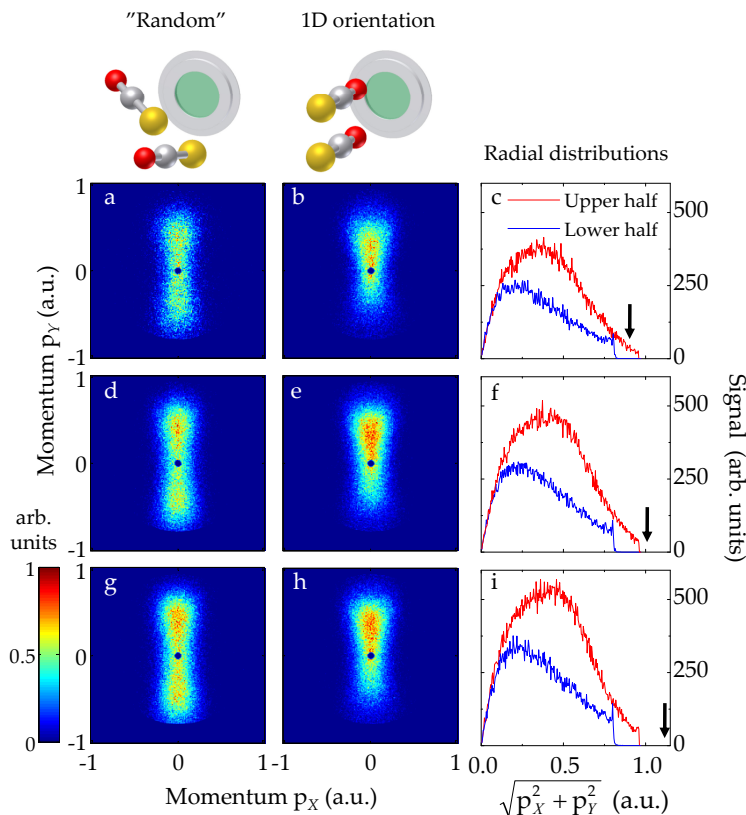


Figure 10.3: Two-dimensional momentum image of electrons produced when a randomly oriented sample of OCS molecules are ionized by the LCP for increasing intensity of the ionization pulse corresponding to $I_{\text{probe}} = 1.76 \times 10^{14} \text{ W/cm}^2$ in **a**, $I_{\text{probe}} = 2.44 \times 10^{14} \text{ W/cm}^2$ in **d** and $I_{\text{probe}} = 2.89 \times 10^{14} \text{ W/cm}^2$ in **g**. **b**, **e** and **h**, same as **a**, **d** and **g**, respectively, but with the OCS molecules aligned along the Z -direction by the alignment pulse polarized perpendicular to the image plane. In **c**, **f** and **i** the radial distributions of the upper and lower parts of images **b**, **e** and **h** are shown. $E_{\text{stat}} = 345 \text{ V/cm}$

in d and $I_{\text{probe}} = 2.89 \times 10^{14} \text{ W/cm}^2$ in g. In b, e and h the molecules are aligned in the geometry shown in Fig. 10.1 and again clear up/down asymmetries are observed. In c, f and i the corresponding radial distributions are given for the upper and lower half of images b, e and h respectively. Several observations can be made from the data. First of all as the intensity of the probe is increased the count rate increases and the electrons seem to acquire more momentum, i.e. extend further out towards the edge of the detector. The number of electrons appearing in the upper half of the images compared to the lower half is almost unchanged as the intensity is increased with $\sim 63\%$ in b and $\sim 64\%$ in e and h.

To try to explain the experimental findings we rely on a quantitative picture, based on a simple two step model together with the theoretical simulations performed by our collaborators in the group of Lars B. Madsen.

10.1.1 Ionization

In the first step the OCS molecules are ionized. Calculations of the Keldysh parameter for a peak intensity $I_{\text{probe}} \simeq 2.4 \times 10^{14} \text{ W/cm}^2$ gives $\gamma = 0.89$ placing the ionization step in the tunneling regime and further evaluations show that the tunnel emission happens over-the-barrier. Calculations of the ionization potential (I_{p0}) of OCS (computed as the positive energy of the highest occupied molecular orbital (HOMO)), is 11.4 eV, in agreement with the experimental value of 11.2 eV [162]. The OCS molecule has a dipole moment of 0.71 Debye pointing from the O-end towards the S-end. The OCS molecule has two degenerate HOMO orbitals shown in Fig. 10.4. Population analysis indicates that 75 % of the HOMO electron density is localized on the S-end, 15 % on the O-end and only 10 % on the C atom. This suggests that ionizing from the HOMO orbital would give rise to a larger dipole moment, in agreement with theoretical calculations. The HOMO-1 orbital of the OCS molecule has a significantly higher ionization potential (17.1 eV from Hartree-Fock calculations), and its contribution to the ionization dynamics is expected to be negligible.

In the presence of the strong probe field the energy levels in the neutral and cations are modified by Stark shifts. This leads to an effective ionization potential, $I_p^{\text{eff}}(\theta)$, given by:

$$I_p^{\text{eff}}(\theta) = I_{p0} + (\mu^{\text{OCS}^+} - \mu^{\text{OCS}})E_{\text{probe}} \cos \theta \quad (10.1)$$

$$+ \frac{1}{2}E_{\text{probe}}^2 [\{ (\alpha_{\parallel}^{\text{OCS}} - \alpha_{\parallel}^{\text{OCS}^+}) - (\alpha_{\perp}^{\text{OCS}} - \alpha_{\perp}^{\text{OCS}^+}) \} \cos^2 \theta + (\alpha_{\perp}^{\text{OCS}} - \alpha_{\perp}^{\text{OCS}^+})]$$

where μ^{OCS} (μ^{OCS^+}) is the permanent dipole moment of OCS (OCS⁺), $\alpha_{\parallel}^{\text{OCS}}$ and $\alpha_{\perp}^{\text{OCS}}$ ($\alpha_{\parallel}^{\text{OCS}^+}$ and $\alpha_{\perp}^{\text{OCS}^+}$) the polarizability components of OCS (OCS⁺) parallel and perpendicular to the internuclear axis, I_{p0} the ionization potential of OCS

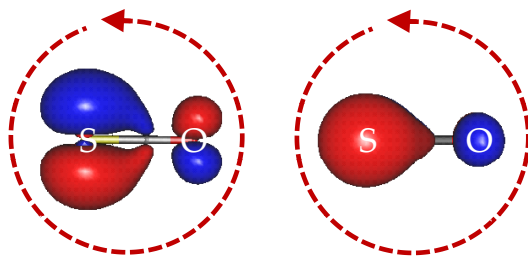


Figure 10.4: Visualization of the degenerate HOMO orbitals of OCS, at an isodensity contour value of 0.1. The orbital to the left lies in the polarization plane of the laser field, and is expected to contribute more to the total ionization yield than the orbital to the right, which has a nodal structure in the polarization plane. The circles with arrows pointing counter clockwise illustrate the circularly-polarized field.

in the absence of any external fields, and θ the polar angle between the instantaneous direction of the circularly polarized probe field and Z -axis (Fig. 10.1). Since the ionization (tunneling) rate depends exponentially on the effective ionization potential [163] Eq. (10.2) shows directly that the oriented OCS molecules may have an asymmetric ionization probability depending on whether the probe field has a component parallel or anti-parallel with the permanent dipole moment. The permanent dipole moment is larger for the cation than for the neutral molecule, leading to larger Stark shifts for the cation than for the neutral molecule. This suggests that the effective ionization potential is lower, hence ionization is more probable, when the instantaneous probe field is pointing in the same direction as the dipole moment than opposed to.

The situation is illustrated in Fig. 10.5a. Indeed calculations confirm that $I_p^{\text{eff}}(\theta = \pi)$ is smaller than $I_p^{\text{eff}}(\theta = 0)$, i. e. the ionization rate is larger for $\mathbf{E}_{\text{probe}}$ parallel rather than anti-parallel to the permanent dipole moment. More generally Eq. (10.3) describes that I_p is smallest, and therefore ionization most probable, for $\pi/2 \leq \theta \leq 3\pi/2$, corresponding to the half part of the optical period where the probe field has a component pointing towards the S-end. This angular dependence of the ionization probability causes a forward-backward asymmetry of the electron emission from the molecule with more electrons ejected when the field is pointing in the direction of the permanent dipole moment.

10.1.2 Propagation in the Field

After ionization the electrons escape the molecule in the presence of the remaining part of the strong probe laser field and are therefore subjected to the force

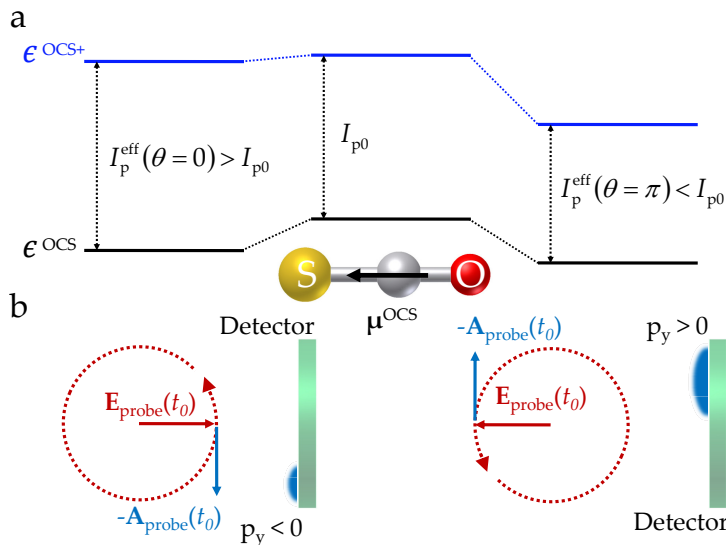


Figure 10.5: Principle of OCS ionization and electron emission. **a**, Sketch of the effective ionization potential for $\mathbf{E}_{\text{probe}}$ anti-parallel to μ^{OCS} (left), no $\mathbf{E}_{\text{probe}}$ (middle) and $\mathbf{E}_{\text{probe}}$ parallel to μ^{OCS} (right). The energy levels of OCS (OCS⁺) are shown by bold black (blue) horizontal lines. **b**, Illustration of the momentum transfer to the electron due to the force from the LCP probe field. In the tunneling process the electron escapes oppositely to the instantaneous direction of the probe field and acquires the final momentum, $-\mathbf{A}_{\text{probe}}(t_0)$. When $\mathbf{E}_{\text{probe}}$ is parallel (anti-parallel) to μ^{OCS} the electron receives an upward (downward) momentum, i.e., $p_y > 0$ ($p_y < 0$). The ionization rate is higher in the parallel case causing more upward than downward electrons.

described by Newton's second Law Eq. (8.7). This leads to a final momentum distribution: $\mathbf{p}_f = m_e \mathbf{v}_f = -|e| \int_{t_0}^{\infty} \mathbf{E}_{\text{probe}}(t) dt = -|e| \mathbf{A}_{\text{probe}}(t_0)$, where t_0 is the instant of ionization. The vector potential, $\mathbf{A}_{\text{probe}}(t)$, for LCP (RCP) advances the field by a phase of $\pi/2$ ($-\pi/2$) causing the forward-backward asymmetry in the ionization step to be transferred into an up-down asymmetry in the final momentum distribution (along the Y -direction, Fig. 10.1a). This is illustrated in Fig. 10.5b. The ejected electrons drift perpendicular to the electric field direction at the moment of ionization.

To explain the experimental findings the group of Lars B. Madsen has modeled the ionization process by modified tunneling theory. Their model is based on the static tunneling rate [163, 164] for an s -state with the binding energy of the highest occupied molecular orbital (HOMO) in OCS, taking saturation [165] into

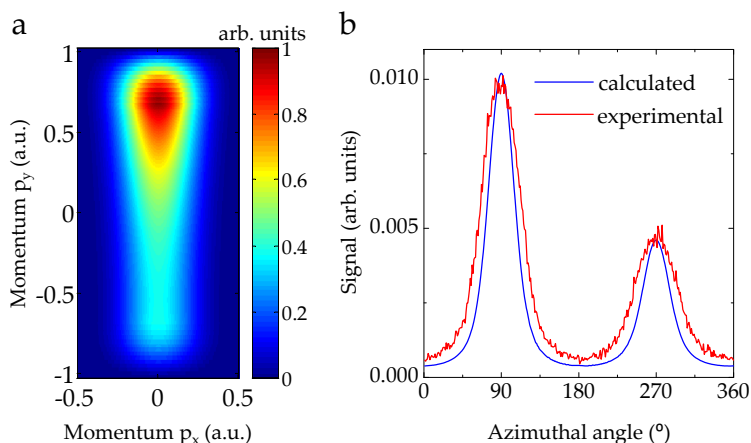


Figure 10.6: Calculated photoelectron images and angular distributions. **a**, Calculated 2-dimensional electron momentum distribution for ionization of 1D aligned and oriented OCS employing a LCP probe pulse similar to the one used in the experiment (Fig. 2d). **b**, Calculated (blue curve) angular distribution of the photoelectrons from the distribution in **a**. The red curve is the experimental angular distribution obtained from the image displayed in Fig. 10.2e.

account and, importantly, including Stark shifts of both OCS and OCS⁺ energy levels due to the interaction between the probe laser field, $\mathbf{E}_{\text{probe}}$, and the permanent and induced dipole moments. The calculated momentum distribution, projected onto the plane corresponding to the detector, is shown in Fig. 10.6 a for LCP probe pulses with the same characteristics as the experimental pulses. (The result with RCP pulses is identical except for having the opposite up-down asymmetry). Focal volume effects are included [166] and an orientation of 80/20 based on the experimental findings is assumed. The similarity with the measurements (Fig. 10.2 d) is clear. In particular, the theoretical up/total ratio of 65 %, compares very well with the measured value (64 %). A more quantitative comparison is provided in Fig. 10.6b, where the experimental and numerical angular distribution, obtained by radially integrating the distribution in Fig. 10.2 d, for LCP is plotted. The agreement is gratifying.

The observations of Fig. 10.3, showing that when the intensity is increased the electrons extend further out on the detector, can also be understood by simple classical arguments. In the simple classical picture the maximum kinetic

energy the electrons can pick up from a circularly polarized field is given by

$$E_{\text{kin,max}} = \frac{1}{2} m_e v_{\text{max}}^2 = \frac{e^2 E_0^2}{2m_e \omega^2} = U_p \quad (10.2)$$

where the maximum velocity the electron can accumulate from the field is readily obtained from Eq. (8.9).

Expressed in terms of the maximum acquired momentum it reads $p_{\text{max}} = \sqrt{2U_p/m_e}$.

The maximum drift momentum corresponding to the intensities applied in the experiments shown in Fig. 10.3 yield $p_{\text{max}} = 0.88$ a.u., 1.03 a.u. and 1.12 a.u. respectively, and are indicated on the radial distributions by an arrow. Although the values lie close to or above the active area of the detection region, the trend is quite clear and fits well with the cutoff in the data. Only very few electrons are expected to acquire the maximum drift velocity as is also seen in the radial distributions. This is to be expected due to focal volume effects and ionization not occurring only at the peak intensity. Furthermore, simply the fact that the images shown in Fig. 10.3 represent 2D projections of the full distribution also contribute.

10.2 Linearly Polarized Probe Beam

In this section photoelectron angular distributions from strong field ionization with intense, linearly polarized, 30 fs laser pulses of 1D oriented OCS molecules are measured. The experimental procedure is similar to the one described in the previous section, however, with the important difference that the polarization of the probe pulse is now changed back from circular to linear. Hereby the complexity is increased both experimentally, due to the enhanced number of probe geometries possible, but also in the interpretation as the linearly polarized probe pulse allows rescattering of the electron. The intensity of the probe pulse is lowered to $I_{\text{probe}} = 1.73 \times 10^{14}$ W/cm² placing the ionization in the tunnel regime with $\gamma = 0.74$.

Figure 10.7 shows photoelectron images recorded as a function of angle between the polarization axis of the probe beam and the molecular alignment axis. In all the images the linearly polarized probe beam is kept fixed along the *Y*-direction, hence parallel to the plane of the detector. When only the probe beam is included (Fig. 10.7 a and f) the bulk of the electron emission occurs along the polarization vector of the probe pulse. In addition, some radial structure is observed in the images, with the electron momentum distribution appearing to some extent to be grouped around a series of discrete values. These observations are ascribed to ATI channels characteristic of multiphoton ionization.

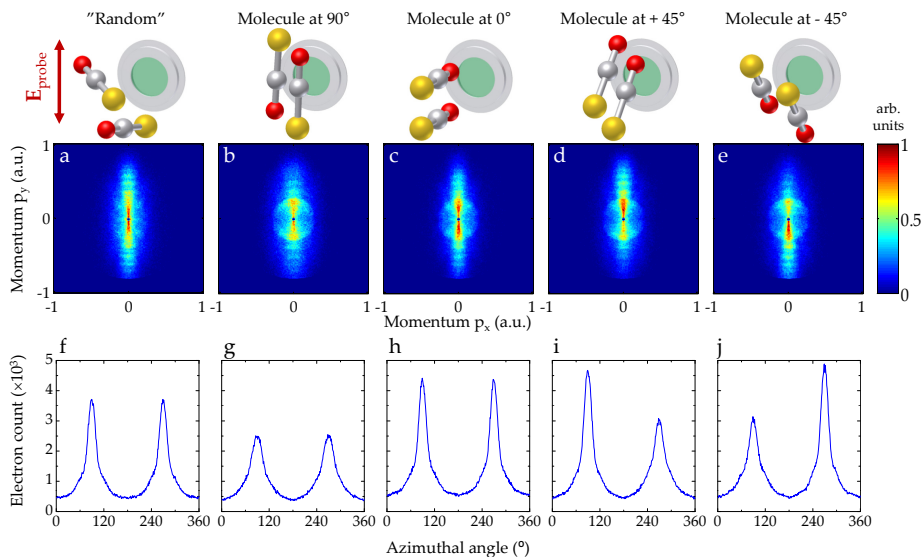


Figure 10.7: 2D photoelectron images as a function of the horizontal momentum p_x and the vertical momentum p_y from tunnel ionization of unaligned OCS molecules (a), from adiabatically aligned OCS molecules with $\beta_{\text{align}} = 90^\circ$ (b) and from adiabatically oriented molecules with $\beta_{\text{align}} = 0^\circ$ (c), $\beta_{\text{align}} = 45^\circ$ (d) and $\beta_{\text{align}} = -45^\circ$ (e), where β_{align} is the angle between the polarization of the alignment pulse and the static electric field from the VMI electrodes. All images are recorded with the probe pulse polarized vertically, i. e. along the y-direction ($\beta_{\text{probe}} = 90^\circ$, where β_{probe} is the angle between the polarization of the probe pulse and the static electric field from the VMI electrodes).

Clear up-down asymmetries are observed in images d and e with the number of electrons detected in the upper part compared to the total number of electrons corresponding to 53% and 46%, respectively.

f - j shows the angular distribution obtained for a momentum distribution corresponding to $\sqrt{p_x^2 + p_y^2} = 0.04 - 0.78$ a.u. of the images a - e.

The experiment was conducted with $I_{\text{probe}} = 1.73 \times 10^{14}$ W/cm², $I_{\text{align, YAG}} = 8.4 \times 10^{11}$ W/cm² and $E_{\text{stat}} = 345$ V/cm.

Although the intensity places the ionization in the tunnel regime, one has to remember that the boundaries between tunnel and multiphoton are floating and ionization occurs not only at the peak intensity, but due to focal volume averaging ionization at lower intensity approaching the multiphoton regime is highly likely to contribute.

When the alignment laser is included parallel to the polarization of the probe laser (image Fig. 10.7 b and corresponding angular distribution g) a broadening is observed, with more electrons emitted off axis, as well as a overall decrease in the electron emission signal. A narrowing and an increase in the signal is observed when the aligning laser is turned perpendicular to the detector (Fig. 10.7 c and h). However the most striking features appear when the molecules are oriented at $+45^\circ$ (Fig. 10.7 d and i) or -45° (Fig. 10.7 e and j). Pronounced up-down asymmetries are observed with the number of electrons detected in the upper part compared to the total number of electrons corresponding to 53 % and 46 % for d and e, respectively. The asymmetry increases with increasing momentum. For a momentum distributions corresponding to $\sqrt{p_X^2 + p_Y^2} = 0.39 - 0.78$ a.u. number of electrons detected in the upper part compared to the total number of electrons increases to 56 % and 42 % for image d and e, respectively. From the measurements of alignment and orientation we know that the geometries depicted in Fig. 10.7 d and e correspond to a degree of orientation of 73 % of the molecules having the S-end pointing away from the detector.

Similar to the experiment described in Fig. 10.7 PADs were obtained from field-free aligned molecules Fig. 10.8. Here molecular alignment is obtained in the non-adiabatic regime using a 0.5 ps long, 800nm kick pulse that sets up a rotational wave-packet in the molecule. The probe beam is then synchronized to the peak of alignment at time delay of $t = 40.5$ ps with respect to the alignment kick pulse, corresponding to the half J revival of OCS as described in Chapter 7.

For experimental reasons measurements were performed at a slightly lower intensity of the probe beam, corresponding to $I_{\text{probe}} = 1.50 \times 10^{14}$ W/cm². At this intensity the Keldysh parameter is $\gamma = 0.80$, still placing the ionization step in the tunnel regime. The observations of Fig. 10.8 a-c are very similar and perfectly consistent with the corresponding observations of Fig. 10.7 a-c. However in Fig. 10.8d where the molecules are aligned at $+45^\circ$ no up/down asymmetry is observed. The important difference between the experiments shown in Fig. 10.7 and Fig. 10.8 is that since the alignment is induced in the nonadiabatic regime for the latter, only alignment and not orientation of the molecules is observed. This shows that the asymmetry of Fig. 10.2 d and e originates from orientation of the molecular dipole moment rather than from an artifact of the ionizing probe field. It is important to note that asymmetries have been observed previously in PADs from strong field ionization of atoms with short (few cycle) pulses. In these experiments the asymmetry originated from the asymmetric nature of the

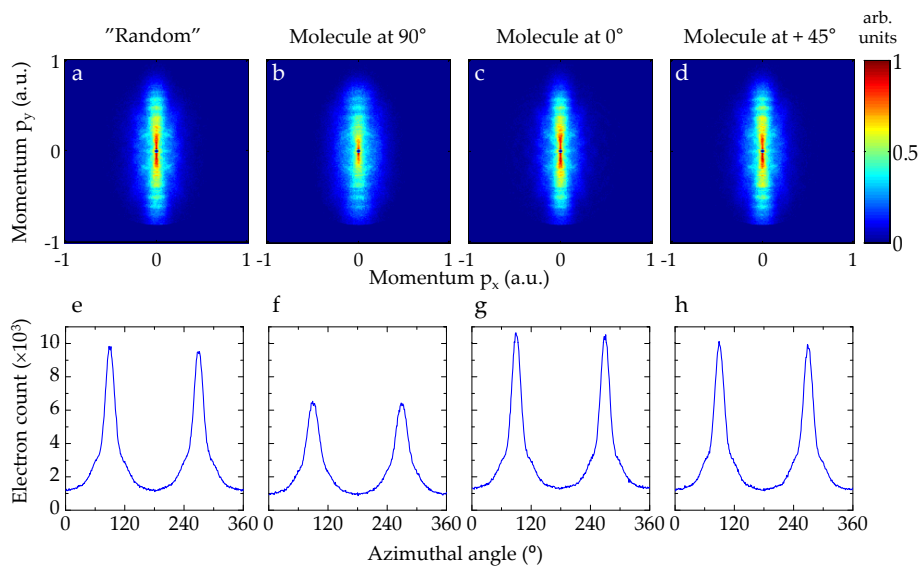


Figure 10.8: 2D photoelectron images as a function of the horizontal momentum p_x and the vertical momentum p_y from tunnel ionization of unaligned OCS molecules (a) and from non-adiabatically aligned OCS molecules with $\beta_{\text{align}} = 90^\circ$ (b), $\beta_{\text{align}} = 0^\circ$ (c) and $\beta_{\text{align}} = 45^\circ$ (d), where β_{align} is the angle between the polarization of the laser pulse and the static electric field from the VMI electrodes. All images are recorded with the probe pulse polarized vertically, i. e. along the y-direction ($\beta_{\text{probe}} = 90^\circ$, where β_{probe} is the angle between the polarization of the probe pulse and the static electric field from the VMI electrodes).

Compared to Fig. ?? image d displays no up/down asymmetry since alignment takes place in the non-adiabatic regime, where no orientation of the molecule is observed.

e - h shows the angular distribution obtained for a momentum distribution corresponding to $\sqrt{p_x^2 + p_y^2} = 0.04 - 0.78$ a.u. of the images a - d.

The experiment was conducted with $I_{\text{probe}} = 1.50 \times 10^{14}$ W/cm², $I_{\text{align}, 800} = 8.3 \times 10^{12}$ W/cm² and $E_{\text{stat}} = 345$ V/cm.

carrier envelope phase stabilized few cycle pulses [167–169]. The mechanism responsible for the asymmetry observed in the experiments described in this section is however completely different. The pulses imposed here are relatively long (not few cycle) and even more importantly not carrier envelope phase stabilized, hence they cannot introduce asymmetry on their own.

To investigate the origin of the asymmetries in the PADs further, experiments were conducted at different geometries of the alignment and probe pulse polarizations.

In Fig. 10.9 images were recorded with the probe beam polarized at $\beta_{\text{probe}} = +/ - 45^\circ$, where β_{probe} is the angle between the polarization of the probe pulse and the static electric field from the VMI electrodes. In images a and b only the probe beam is included at $\beta_{\text{probe}} = +45^\circ$ and -45° respectively. The images are perfectly up/down symmetric. The radial structure observed in Fig. 10.7 is no longer resolvable in these geometries due to the collapse of the 2D projection of the electron momentum distribution towards the center of the detector. In Fig. 10.9 c and d the OCS molecules are adiabatically oriented with $\beta_{\text{align}} = 0^\circ$, where β_{align} is the angle between the polarization of the laser pulse and the static electric field from the VMI electrodes. Clear up/down asymmetries are observed with the number of electrons detected in the upper part compared to the total number of electrons corresponding to 56 % in c, 43 % in d. Again, the asymmetry increases with increasing momentum giving rise to 59 % and 40 % of the electrons appearing in the upper part of images c and d, respectively, for a momentum distributions corresponding to $\sqrt{p_X^2 + p_Y^2} = 0.39 - 0.78$ a.u. In Fig. 10.9e and f and Fig. 10.9 g and h the polarization of the alignment laser is turned to $\beta_{\text{align}} = +45^\circ$ and $\beta_{\text{align}} = -45^\circ$ respectively. When the probe beam is parallel to the alignment beam e and h a broadening of the electron emission as well as a clear asymmetry is observed, with the number of electrons detected in the upper part compared to the total number of electrons corresponding to 54 % in e and 45 % in h. When the probe beam is perpendicular to the alignment beam Fig. 10.9 f and g no asymmetry is observed.

10.2.1 ‘Simple Woman’s Model’

In the previous section it was seen how the asymmetries in the PADs obtained with a circularly polarized probe laser were governed by an asymmetry in the ionization rate that manifested itself as an up/down asymmetry through the propagation of the electron in the remaining part of the field. However, here the underlying mechanism is different. In the case of a linearly polarized laser field Eq. (10.2) still holds and an asymmetry in the ionization probability is to be expected for an oscillating field alternating between having a component parallel or anti-parallel to the molecular dipole moment. However, this cannot en-

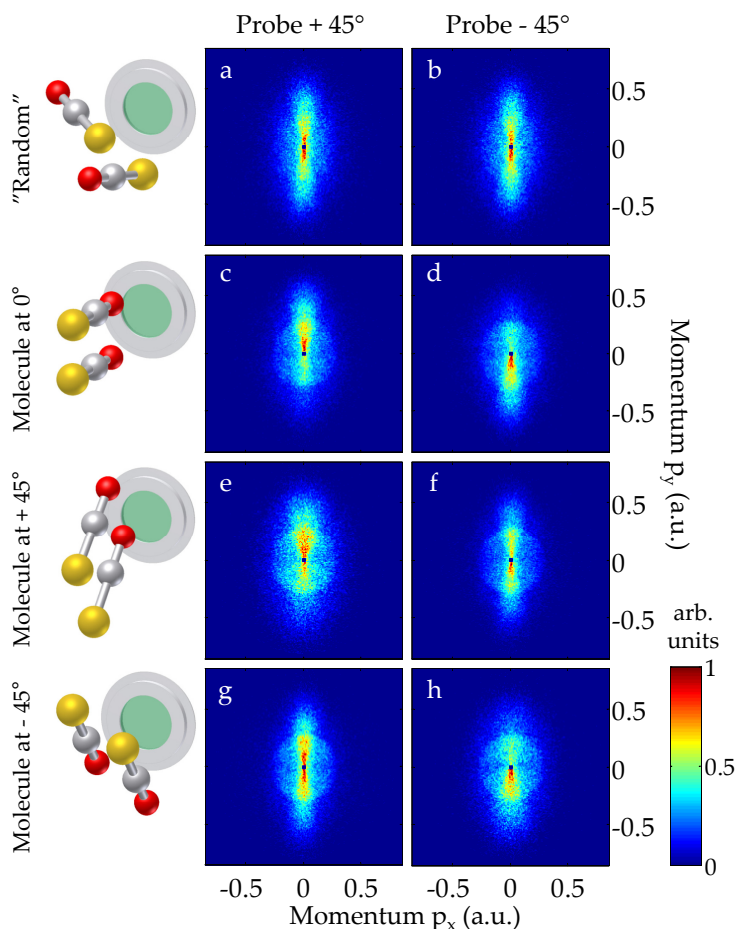


Figure 10.9: 2D photoelectron images as a function of the horizontal momentum p_x and the vertical momentum p_y from tunnel ionization of unaligned OCS molecules (**a** and **b**) and from adiabatically oriented OCS molecules with $\beta_{\text{align}} = 0^\circ$ (**c** and **d**), $\beta_{\text{align}} = 45^\circ$ (**e** and **f**) and $\beta_{\text{align}} = -45^\circ$ (**g** and **h**), where β_{align} is the angle between the polarization of the laser pulse and the static electric field from the VMI electrodes. The images **a**, **c**, **e** and **g** are recorded with the probe pulse polarized along $\beta_{\text{probe}} = 45^\circ$ and images **b**, **d**, **f** and **h** are recorded with the probe pulse polarized along $\beta_{\text{probe}} = -45^\circ$, where β_{probe} is the angle between the polarization of the probe pulse and the static electric field from the VMI electrodes.

Clear up-down asymmetries are observed in images **c**, **d**, **e** and **h** with the number of electrons detected in the upper part compared to the total number of electrons corresponding to 56% in **c**, 43% in **d**, 54% in **e** and 45% in **h**.

The experiment was conducted with $I_{\text{probe}} = 1.76 \times 10^{14} \text{ W/cm}^2$, $I_{\text{align, YAG}} = 5.6 \times 10^{11} \text{ W/cm}^2$ and $E_{\text{stat}} = 345 \text{ V/cm}$.

counter for an asymmetry in the PADs, as justified by the following arguments. Let us consider the situation illustrated in Fig. 10.10 with the probe polarized vertically along the Y -direction and the molecule fixed at $\beta_{\text{align}} = 45^\circ$. The linearly polarized laser field can then be described as

$$\mathbf{E} = E_0 \cos(\omega t) \hat{\mathbf{e}}_Y \quad (10.3)$$

From Eq. (10.2) we know that ionization is most likely to occur when the laser field is pointing in the direction of the S-end, hence for simplicity let us assume that the molecule is only ionized in an interval $\frac{\pi}{2} \geq \omega t \leq \frac{3\pi}{2}$, corresponding to the field pointing in the negative y -direction. Relying on the simple man's model and neglecting the pulse envelope the final velocities become proportional to $\sin(\omega t)$ as seen from Eq. (8.9), which in the interval $\frac{\pi}{2} \geq \omega t \leq \frac{3\pi}{2}$ is equally likely to adopt negative as well as positive values. The mechanism responsible for the up/down asymmetry must be found elsewhere. The main difference compared to the case of the circularly polarized laser field is that as the linearly polarized field alternates it can drive the electron back towards the ion allowing the electron to rescatter. The emitted electron can no longer be viewed as free after the initial ionization step as it stays in the vicinity of the parent ion for several laser cycles and the interaction with the molecular ion (potential) can no longer be neglected. In an attempt to interpret the observed finding one could speculate that as the electron returns to the molecular ion its trajectory will be influenced by the forces originating from the molecular dipole as illustrated in Fig. 10.10. For the two situations shown in Fig. 10.10 there will be a net force from the dipole pulling the electron in the positive Y -direction, independent of whether the electron returns from the positive or negative Y -direction. For the situation illustrated in Fig. 10.10 this would result in more electrons detected on the upper half of the detector, consistent with the experimental observations in Fig. 10.7 d. In fact this simple picture is consistent with all the geometries of Fig. 10.7 to Fig. 10.9.

Of course this is greatly simplifying the underlying physics as the rescattering of the electron with the molecules is very complex and recombination with the molecules is completely neglected. Only the dipole forces and not the coulomb potential is considered. However since the coulomb potential is spherical symmetric it is unlikely to participate in any asymmetric distribution. This attempt to interpret the experimental findings should give a qualitative picture of the mechanism and the group of Lars B. Madsen are currently working on interpreting the data more quantitatively.

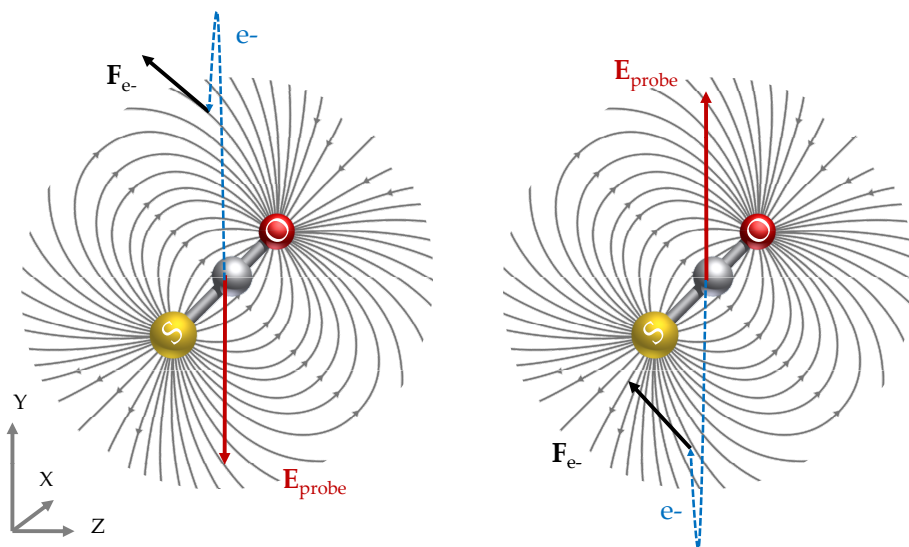


Figure 10.10: Schematic illustration of the rescattering of the electron responsible for the asymmetry of the PADs. See text for details

10.2.2 Symmetry Considerations

Another experimental feature that can be interpreted using simple arguments is the broadening of the off-axis electron emission when the polarization of the probe and the alignment laser coincides (Fig. 10.7 b, Fig. 10.8 b and Fig. 10.9 e and h).

As mentioned in the introduction in connection with TRPES the photoelectron angular distributions reveal or hold information of the orbital that is ionized from. Theoretically this has been shown to be the case also in the strong field regime. In theoretical studies a strong dependence on the anisotropy and the yield of the photoelectrons upon the orientation between the molecule and the field has been observed. In particular, electron emission in nodal planes is suppressed and interpreted to be a consequence of the symmetry of the highest occupied molecular orbital [170, 171]. If similar although simplified arguments are applied in case of OCS the strong connection between the PADs and the symmetry of the molecular orbital becomes clear. In simple terms the ionization rate is described by Fermi's Golden Rule [?]

$$W_{f \leftarrow i} = 2\pi\hbar |\langle \psi_f | \hat{H}_{int} | \psi_i \rangle|^2 \rho \quad (10.4)$$

where $\langle \psi_f | \hat{H}_{int} | \psi_i \rangle$ is the transition dipole moment from the initial state ψ_i to the

final state ψ_f through the interaction described by the interaction Hamiltonian operator and ρ is the density of states.

The ionization step is often expressed in terms of the vector potential of the electromagnetic field and the momentum operator. In the dipole approximation the laser-atom interaction is given by $H_{int}(t) = \frac{e}{m} \mathbf{A}(t) \cdot \mathbf{P} + \frac{e^2 N}{2m} \mathbf{A}^2(t)$ [172] which in the length gauge can be simplified to $H_{int}^L(t) = -\mathbf{E}(t) \cdot \boldsymbol{\mu}$ (ref to atoms and molecules) where the electric dipole moment operator $\boldsymbol{\mu}$ and the electric field \mathbf{E} describe the ionization step.

In order for the transition to occur the ionization probability must be non-zero. In terms of symmetry this is equivalent to the following condition being satisfied

$$\Gamma_f \otimes \Gamma_{\boldsymbol{\mu}\mathbf{E}} \otimes \Gamma_i \ni \Gamma_{TS} \quad (10.5)$$

requiring that the product of the symmetry species of the initial state Γ_i , the dipole operator $\Gamma_{\boldsymbol{\mu}\mathbf{E}}$ and the final state Γ_f must contain the totally symmetric irreducible representation Γ_{TS} of the molecular symmetry group, in order for the transition be allowed.

OCS is a linear molecule belonging to the point group $C_{\infty v}$. The degenerate HOMO shown in Fig. 10.4 has Π symmetry.

Considering one single active electron initially occupying the highest molecular orbital(HOMO) and the final state being that of the free electron wave the expression in Eq. (10.5) can be written as:

$$\Gamma_{e^-} \otimes \Gamma_{\boldsymbol{\mu}\mathbf{E}} \otimes \Gamma_{HOMO} \ni \Gamma_{TS} \quad (10.6)$$

This is, of course, an approximation equivalent to the single active electron strong field approximation that neglects any electron-electron interaction as well as electron-ion interactions. The electromagnetic field is so strong that the electron is promoted to the continuum too fast for any rearrangement in the parent ion electron configuration to take place and by far exceeding the Coulomb attraction.

For simplicity we will consider the situation where OCS oriented with the principal axis aligned along the laboratory fixed Z -direction. In this situation the laboratory frame (X, Y, Z) coincides with the molecular frame (x, y, z) . In the experimental setup the electric field can only have field components in the YZ -plane and E_X is zero, hence the transition can only occur through the y and z components of the electric dipole moment operator. The symmetry of the electric dipole moment operator is given by the symmetry of the corresponding components (x, y, z) specific for the point group. For a linearly polarized probe field in the Z -direction Eq. (10.6) reduces to

$$\Gamma_{e^-} \otimes \Gamma_z \otimes \Gamma_{HOMO} \ni \Gamma_{TS} \quad (10.7)$$

From a character table of the $C_{\infty v}$ point group Γ_z is found to have Σ^+ symmetry, hence being totally symmetric. In order for the above equation to be satisfied the emitted electron must also have Π symmetry. In other words, in the single active electron approximation, when the linear polarization axis of the probe field coincides with the principal axis of the OCS molecule, i. e. with the nodal planes of both degenerate HOMO orbitals, suppression of the electron emission in this direction is expected. Emission along this axis is symmetry forbidden. An overall decrease in the ionization yield is likewise expected and also consistent with the observations (Fig. 10.7 b, Fig. 10.8 b and Fig. 10.9 e and h).

11

MFPADS FROM TUNNEL IONIZATION OF BENZONITRILE

One of the strengths of our method is the extension to the general class of molecules. Although 3D MFPADs have been obtained using the coincidence method [141] the technique requires a triple (or at least double) ionization scheme to extract the full 3D information. Therefore, the method presented here is unique in extracting PADs from strong field single ionization of 3D oriented molecules. To illustrate the potential of our method experiments were conducted on benzonitrile (C_7H_5N) molecules (Fig. 11.2).

Experimentally a target of adiabatically aligned and oriented benzonitrile molecules is created by the combined action of a 10 nanosecond laser pulse and a weak static electric field. A gas mixture of ~ 5 mbar C_7H_5N and 90 bar of He is expanded into vacuum from our Even-Lavie valve. Before reaching the interaction point with the laser pulses and the static field the molecules are selected in the lowest-lying rotational quantum states by our electrostatic deflector. Similar to the PAD measurements on OCS described in the previous chapter, Coulomb explosion imaging measurements confirm that high degrees of alignment and orientation are achieved prior to the PAD measurement on C_7H_5N . Figure 11.1 a and b shows CN^+ ion images from Coulomb explosion of C_7H_5N with the alignment pulse at $\beta_{\text{align}} = 45^\circ$ or -45° and the probe pulse linearly po-

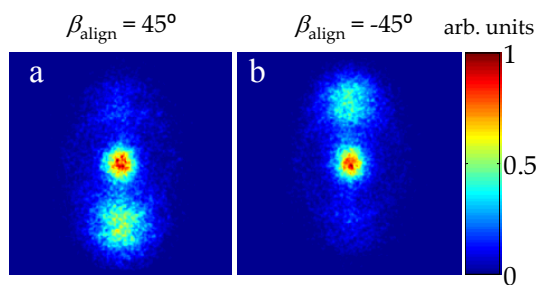


Figure 11.1: Orientation of C_7H_5N by ion detection. **a, b** Images of CN^+ ions for $\beta_{\text{align}} = 45^\circ$ and -45° , respectively and $E_{\text{stat}} = 286 \text{ V/cm}$. In **a** 69 % of all CN^+ ions appear in the upper half of the detector. In **b** 30 % of all CN^+ ions appear in the upper half of the detector. The intensity of the alignment and probe pulses are $7.7 \times 10^{11} \text{ W/cm}^2$ and $4.5 \times 10^{14} \text{ W/cm}^2$, respectively.

larized in the vertical direction (The probe geometry is similar to that of Fig. 5.5). Again, the angular confinement and the asymmetry of the CN^+ ion images give clear evidence of alignment and orientation of the C_7H_5N molecules. However, it should be noted that the asymmetry of the images clearly underestimates the real degree of orientation of the C_7H_5N molecules. In particular, CN^+ is not an ideal observable because, unlike I^+ from Coulomb explosion of iodobenzene, it overlaps with other fragment ions in the time of flight spectrum of C_7H_5N . Hence, the ion images of Fig. 11.1 also contain contributions from carbohydrate fragments from the benzene ring of equal (or nearly equal) mass-to-charge-ratio (e.g. $C_2H_2^+$). These "contaminant" ions are not expected to recoil along the C-CN axis. Furthermore, the ion images are recorded at $E_{\text{stat}} = 286 \text{ V/cm}$ which is significantly lower than the electrostatic extraction field in the electron PAD measurement described next ($E_{\text{stat}} = 467 \text{ V/cm}$). It is to be expected that the degree of orientation should increase strongly when E_{stat} is increased. Also, the orientation will improve due to the increase in the amplitude and the increased static field along the permanent dipole axis when the alignment laser is polarized parallel to E_{stat} . For the purpose of optimizing the experimental conditions, the CN^+ ion images proved, however, fully sufficient.

Next, photoelectron angular distributions are measured. Figure 11.3 displays the electron images and Fig. 11.4 the corresponding angular distributions. The intensity of the probe pulse in these experiment is $1.2 \times 10^{14} \text{ W/cm}^2$, placing the ionization slightly away from the tunneling regime. Even without the alignment pulse a weak up-down asymmetry (Fig. 11.3 a and b) is observed, which we ascribe to mild 1D alignment and orientation of the molecules due to the static field, the large effective dipole moment, and the very low rotational tempera-

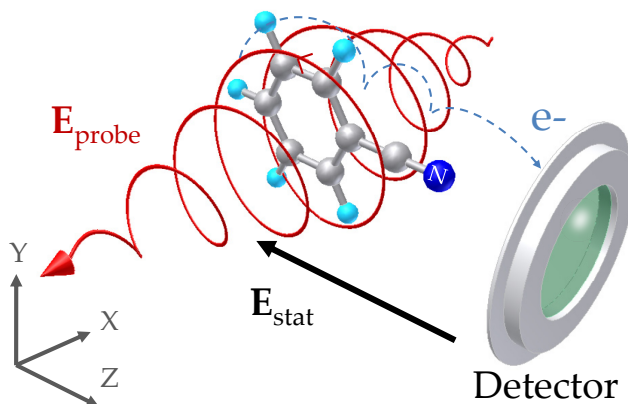


Figure 11.2: Schematic of the experimental setup used to produce photoelectron images showing a C_7H_5N molecule oriented with its permanent dipole moment pointing in the direction of the static electric field. The LCP probe pulse ionizes the molecule and imparts an upward momentum to the freed electron resulting in recording on the upper part of the detector (see text for details).

ture. When the 1D alignment pulse, linearly polarized along the static field axis, is included the asymmetry increases (Fig. 11.3c and d) due to stronger alignment and orientation. For LCP the up/total ratio is $\sim 55\%$, for RCP it is $\sim 44\%$. Unlike OCS described in the previous chapter, C_7H_5N is an asymmetric top molecule and the linearly polarized alignment pulse only confines the C-CN symmetry axis of the molecule, while the benzene ring remains free to rotate around this axis. Additional confinement of the molecular plane, and thus 3D alignment and orientation, is obtained by using an elliptically polarized alignment pulse with the major axis along the static field axis and the minor axis vertical in the images. This equivalent to the 3D alignment and orientation of 2,6-difluoroiodobenzene described in Chapter 6. The total intensity, $7.7 \times 10^{11} \text{ W/cm}^2$, is the same as for the linearly polarized pulse and the intensity ratio between the major and minor axis is 3:1. The resulting electron images (Fig. 11.3 e and f) have essentially the same up-down asymmetry as in panel c and d (since the degree of 1D alignment and orientation is practically unchanged), but they exhibit striking new structures that are not seen in the PADs from 1D oriented molecules. In particular, electron emission in the polarization plane, coinciding with the nodal plane of the HOMO (and the HOMO-1), is suppressed. Such effects were predicted previously but never observed [170, 171].

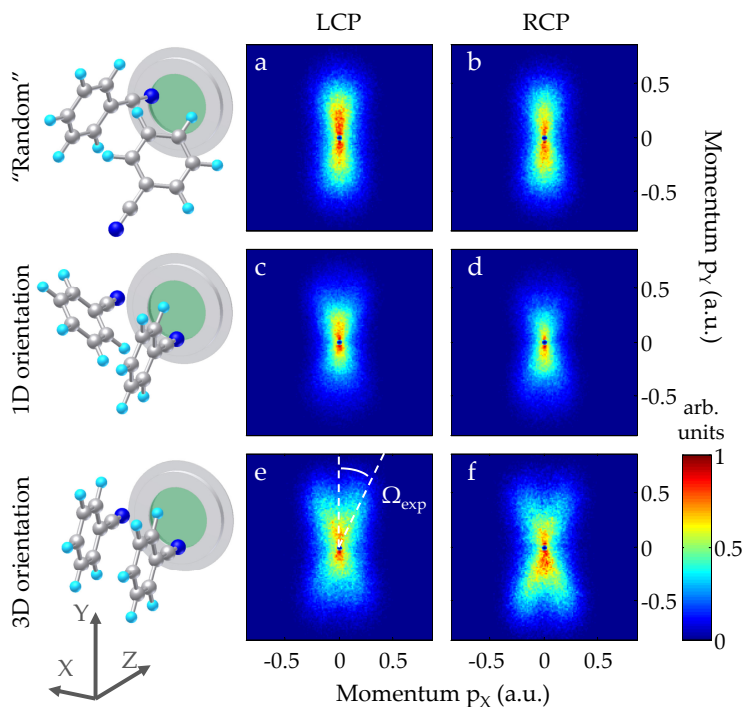


Figure 11.3: Experimental photoelectron images from C_7H_5N . Two-dimensional momentum image of electrons produced when C_7H_5N molecules are ionized by a LCP probe pulse (**a**, **c**, **e**) or RCP probe pulse (**b**, **d**, **f**). In **a** and **b** the molecules are essentially randomly oriented (no alignment pulse used). In **c** and **d** the molecules are 1D oriented (linearly polarized alignment pulse) and in **e** and **f** the molecules are 3D oriented (elliptically polarized alignment pulse). The intensity of the probe pulse is $1.2 \times 10^{14} \text{ W/cm}^2$. In **e** the experimental off-the-nodal-plane angle, $\Omega_{\text{exp}} \simeq 18^\circ \pm 1^\circ$ is shown. See equation (2) for our analytical expression.

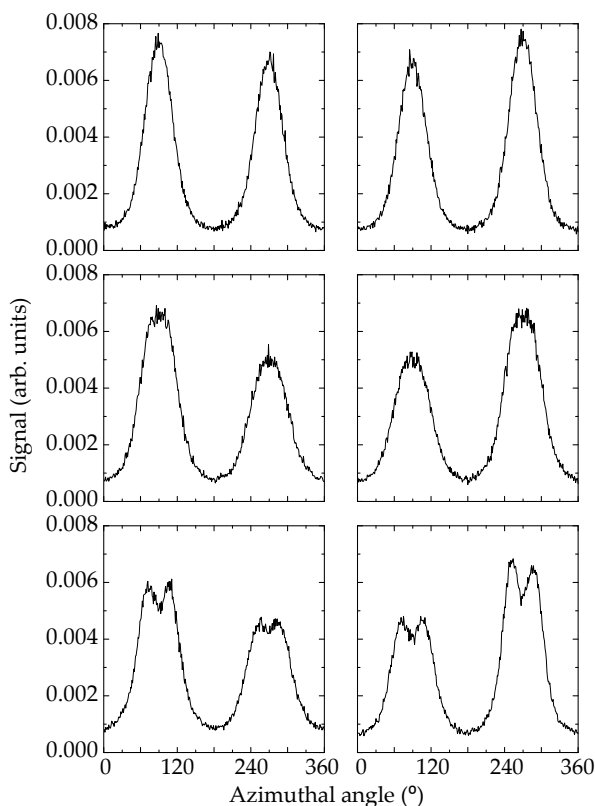


Figure 11.4: Angular distributions obtained from the corresponding photoelectron images displayed in Fig. 11.3.

11.1 Symmetry Considerations

Simple symmetry arguments can be applied to quantify the observed features of the PADs.

Benzonitrile is an asymmetric top molecule. It has a C_2 rotational axis along the principal axis of the molecule, a mirror plan in the molecular plane and perpendicular to the molecular plane along the principal axis placing the molecule in the symmetry group C_{2v} . Similar to the arguments used in Sec. 10.2.2 considering one single active electron initially occupying the highest molecular orbital (HOMO) and the final state being that of the free electron partial wave it was seen that in order for the transition to occur the following conditions should be satisfied

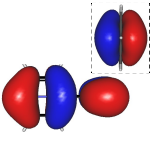
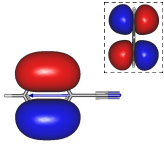
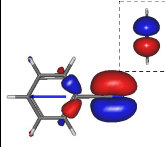
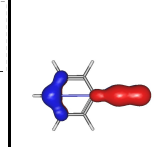
Orbital	HOMO	HOMO-1	HOMO-2	HOMO-3
I_p (eV)	9.79	10.06	12.78	13.33
Shape				

Figure 11.5: The four highest occupied molecular orbitals of C_7H_5N . The molecular plane coincides with the YZ plane.

$$\Gamma_{e^-} \otimes \Gamma_{\mu\mathbf{E}} \otimes \Gamma_{HOMO} \ni \Gamma_{TS} \quad (11.1)$$

Adapting the geometry shown in Fig. 11.2 where benzonitrile is 3D oriented with the principal axis aligned along the laboratory fixed Z -direction, the laboratory frame (X, Y, Z) coincides with the molecular frame (x, y, z). In the experimental setup the electric field can only have field components in the YZ -plane and E_X is zero, hence the transition can only occur through the y and z components of the electric dipole moment operator. The symmetry of the electric dipole moment operator is given by the symmetry of the corresponding components (x, y, z) specific for the point group.

$$\Gamma_{e^-} \otimes (\Gamma_y \oplus \Gamma_z) \otimes \Gamma_{HOMO} \ni \Gamma_{TS} \quad (11.2)$$

From a character table of the C_{2v} point group [173], Γ_y and Γ_z are found to have B_2 and A_1 symmetry, respectively. Applying symmetry arguments it can readily be seen that the HOMO shown in Fig. 11.5 has B_1 symmetry, hence

$$\Gamma_{e^-} \otimes B_2 \otimes B_1 \ni A_1 \quad \vee \quad \Gamma_{e^-} \otimes A_1 \otimes B_1 \ni A_1 \quad (11.3)$$

$$\Gamma_{e^-} = A_2 \quad \vee \quad \Gamma_{e^-} = B_1 \quad (11.4)$$

Similar arguments can be applied taking the initial state to be the HOMO-1 with symmetry A_2 resulting in exactly the same symmetries of the final outgoing electron. In conclusion assuming a single active electron initially occupying the HOMO with B_1 symmetry is promoted to the continuum through ionization with a probe beam of circular polarization in the YZ -plane will result in

an electron final state of either A_2 symmetry (through the field Y component) or B_1 symmetry (from the field Z component). In this case the photoelectron angular distribution should reflect the symmetry of the final electron state and indeed both symmetries are consistent with the experimental observations. The PADs of Fig. 11.3 corresponds to 2D projections of the final electron state onto the XY -plane. A pronounced dip is observed in the YZ -plane consistent with a suppression of the electron emission in the nodal plane of the HOMO. In addition, the A_2 symmetry should also give rise to a dip in the XZ -plane. A suppression of the electron emission in the XZ -plane may be weakly indicated in the images, however, since the electrons do not acquire drift momentum in this direction by the probe field, a clear effect is not observed experimentally.

11.2 Tunnel Model

For C_7H_5N , the molecular structure, population analysis, and orbital energies were obtained from Hartree-Fock calculations performed by the group of Lars B. Madsen. The four highest occupied molecular orbitals and corresponding orbital energies are shown in Fig. 11.5. Unlike OCS the HOMO and HOMO-1 orbitals of C_7H_5N are nearly degenerate in energy, hence contributions from orbitals other than the HOMO can not be neglected in the ionization step.

To provide a more qualitative explanation of the experimental findings for 3D oriented C_7H_5N calculations were performed. In case of C_7H_5N , the emission takes place slightly away from the tunnel regime (the Keldysh parameter is 1.16). In the case of 1D oriented molecules, the theoretical model developed for OCS still applies. However, in the case of the 3D-oriented molecule, the model has to be extended to include the emission off the molecular orbital nodal plane. The plane of the polarization of the laser field coincides with the nodal plane of both HOMO and HOMO-1 orbitals.

In the model perfect 3D orientation in the way shown in the lower panel of Fig. 11.3 is assumed. The initial state of a molecule is modelled by a simple $2p_x$ orbital with the angular node in the polarization (Y, Z) plane and the p-lobes parallel to the X -axis. The presence of the nodal plane prevents electron emission in the polarization plane. This is observed in the calculated electron momentum distribution displayed in Fig. 11.6 for LCP. Initial electron emission in the perpendicular direction is, however, possible and is incorporated by including a factor describing the momentum distribution in the X -direction in the initial orbital. The slight asymmetry of the up/total ratio (52 %) visible in Fig. 11.6 is still governed by laser-induced Stark shifts, as described for OCS, whereas the observed left-right splitting (along the X -axis) of the momentum distribution projected on the detector plane is due to the presence of the nodal

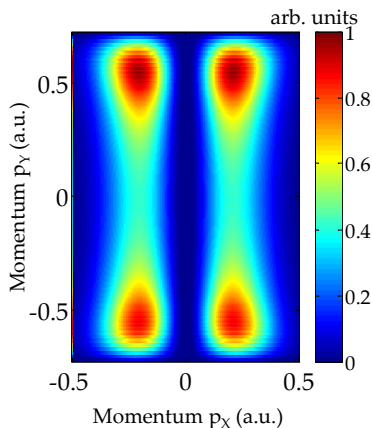


Figure 11.6: Calculated 2-dimensional electron momentum distribution for ionization from the HOMO and HOMO-1 of 3D aligned and oriented C_7H_5N employing a LCP probe pulse similar to the one used in the experiment (Fig. 4e).

plane. Lars B. Madsen and coworkers have obtained a new closed analytical expression for the off-the-nodal-plane angle, Ω_{theo} (Fig. 11.3e), and at the intensity $1.23 \times 10^{14} \text{ W/cm}^2$,

$$\Omega_{\text{theo}} = \arctan(2\omega/\sqrt{\pi E_0 \kappa}) \simeq 18.8^\circ, \quad (11.5)$$

with $\kappa = \sqrt{2I_{p0}}$. To obtain a corresponding experimental value of the off-the-nodal-plane angle angular distributions from the outermost electrons of Fig. 11.3 e and f are plotted. The electrons that reach furthest out on the detector correspond to the electrons that have required the highest momentum, and should thus come closest to the analytical expression.

The experimental value of the off-the-nodal-plane angle is found to be $\Omega_{\text{exp}} = 18^\circ \pm 1^\circ$ (Fig. 11.7) in good agreement with the theoretical predictions. The experimental observation of a nonzero electron signal in the polarization plane is partly due to non perfect alignment of the molecule and possibly also due to a contribution from the HOMO-2 whose nodal plane is perpendicular to the laser polarization plane.

One of the major concerns in connection with adiabatic alignment is if the presence of the YAG field can perturb the ionization step or the electron trajectory and thus the experimental outcome. One concern could be that the presence of the YAG field could lead to shifting of the energy levels of high lying Rydberg states of the molecule into resonance hereby creating a different ionization pathway. Such effects will depend strongly on the specific molecule. For

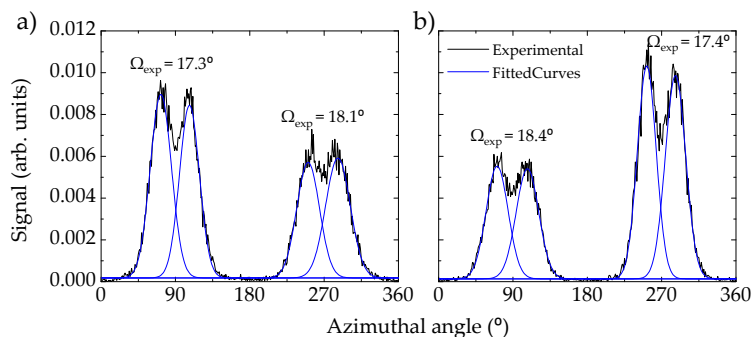


Figure 11.7: Angular distributions obtained from the corresponding photoelectron images displayed in Fig. 11.3e and f of the outermost electrons corresponding to the radial range $\sqrt{p_x^2 + p_y^2} = 0.59 - 0.99$ a.u. The angle Ω_{exp} is determined from the angular distributions by a four peak fit as shown.

benzotrinitrile it is observed in the time of flight (TOF) that the presence of both the YAG and probe in the above experiments leads to excessive fragmentation of the molecule. For comparison it should be noted that the presence of the YAG in connection with the experiments performed on OCS molecules did not induce changes in the TOF and left the parent molecular ion unchanged.

To investigate the mechanism responsible for the fragmentation we performed measurement at different time delays between the YAG and the probe. When only the probe is present only the parent molecular ion is observed in the TOF. Sending in the YAG pulse at a time delay much earlier than the probe, no change is observed in the TOF. Including the YAG pulse at the same time as, or much later than the probe pulse leads very similar fragmentation patterns. This suggests that the mechanism responsible for the fragmentation proceeds in two distinct steps. First, the molecules are singly ionized by the probe pulse and secondly the YAG pulse dissociates the unstable cation initially produced. Since the timescale for dissociation is much longer than the time for the electron to escape the vicinity of the core, the observed fragmentation should not effect the electron trajectory.

To confirm that the effects described above truly are results of strongly oriented molecules, experiments were performed under conditions where no orientation and only poor alignment of BN is expected. Running the Even-Lavie valve at low He backing pressure leads to poor cooling. Under these conditions hardly any change was observed in the electron images from the probe alone and the inclusion of the YAG pulse, suggesting that the effects observed are not field induced.

The results presented here show that molecular frame PADs can be obtained for a broad range of species independent of whether 1D or 3D orientation is needed to fully fix the molecule in space. Strong-field ionization by fs circularly polarized pulses is an ultrafast probe, sensitive to molecular properties such as nodal planes. The field drives the electrons monotonously away from the parent ion without rescattering effects blurring the ionization dynamics.

12

ANGLE DEPENDENT STRONG FIELD IONIZATION YIELDS

12.1 Introduction

As already mentioned strong field physics is emerging as a promising field for studying the structure and dynamics of molecular systems. However, interpretation of the underlying physics has been and still is an area of quite some debate. Single ionization from multiphoton or tunnel ionization is a fundamental process and a crucial first step to understanding most molecular strong field phenomena. Of particular importance is the understanding of the dependence of the initial ionizations step on the molecular orientation. Exact theoretical calculation of the alignment dependent ionization rates are obtained by solving the time dependent Schrödinger equation, however these full ab initio calculations are only available for H_2^+ [174, 175] and H_2 [176]. Commonly used theories to explain strong field phenomena extended to larger systems are the molecular tunneling theory [177] and the strong field approximation [178]. However recent experiments have shown to disagree with these theories [161]. Thus far experimental alignment dependent ionization rates have only been obtained on small molecular systems such as N_2 , O_2 , CO , CO_2 and C_2H_2 [161, 179–181]. In some of the previous measurement extracting the angle dependent ionization

rates from the measurement have involved several steps, complicating the interpretation. The first direct measurement of the angular dependence of ionization was reported in 2007 by Pavičić *et al*[161] where the molecules were aligned non-adiabatically, demonstrating the essential need for creation of an ensemble of highly aligned molecules.

Recently, a different theoretical approach has been proposed by Abu-samha and Madsen [182]. They use *ab initio* theory within the single electron approximation, demonstrating the importance of including the dynamics of the excited state manifold. Their theory explained the breakdown of the molecular tunneling theory and strong-field approximation, that neglects excited electronic structure. The calculations are in unprecedented agreement with the experiments by Pavičić *et al* [161].

To fully test existing theories, experiments extended to larger and more complex molecular systems are needed. For that reason we performed measurements on the angular dependence of the ionization yield on carbonylsulfide (OCS) and benzonitrile (C_7H_5N) molecules. The results presented here are preliminary and have not yet been compared to theory.

12.2 Results and Discussion

First, the ionization yield of single ionization of OCS molecules is measured as a function of the angle between the polarization of the alignment and probe laser pulse, $\Delta\beta$. In order to measure the angular dependence a high degree of alignment is required. For that reason, OCS molecules are selected in the lowest rotational quantum states and alignment is induced in the adiabatic regime. Under experimental conditions equal to that of Chapter 5 and Chapter 10 with the intensity of the YAG laser pulse corresponding to $I_{\text{align, YAG}} = 8.4 \times 10^{11} \text{ W/cm}^2$ a degree of alignment of $\langle \cos^2 \theta_{2D} \rangle = 0.90$ is obtained. Figure 12.1 shows the ionization yield as a function of the angle between the polarization axis of the alignment and probe pulse, $\Delta\beta$. Ionization yield is measured from the total OCS^+ signal at two different intensities of the probe beam, where high and low intensity correspond to $I_{\text{probe, high}} = 1.77 \times 10^{14} \text{ W/cm}^2$ and $I_{\text{probe, low}} = 1.48 \times 10^{14} \text{ W/cm}^2$, respectively. The data has been normalized to the total ionization yield from unaligned molecules. A clear suppression of the signal is observed when $\Delta\beta = 0^\circ$, i.e. when the polarization vector of the probe coincides with the internuclear axis of the OCS molecules. At $\Delta\beta = 90^\circ$ a clear increase in the ionization yield is observed. There is hardly any difference between the angular dependence obtained for $I_{\text{probe, high}} = 1.77 \times 10^{14} \text{ W/cm}^2$ and $I_{\text{probe, low}} = 1.48 \times 10^{14} \text{ W/cm}^2$.

The observations can to some extent be explained with molecular symmetry

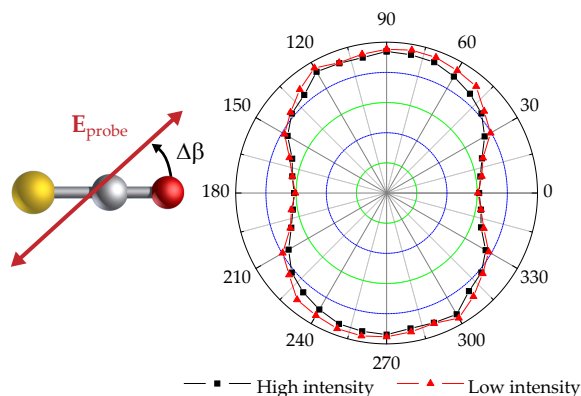


Figure 12.1: Measured ionization yield as a function of the angle between the polarization axis of the aligning and ionizing (probe) beam. Ionization yield is measured at two different intensities of the probe beam, where high and low intensity correspond to $I_{\text{probe, high}} = 1.77 \times 10^{14} \text{ W/cm}^2$ and $I_{\text{probe, low}} = 1.48 \times 10^{14} \text{ W/cm}^2$ respectively. The ionization yield has been normalized to the total ionization yield obtained when only the ionizing laser is included. Alignment is induced in the adiabatic regime from 10 ns long YAG pulse with the intensity $I_{\text{align, YAG}} = 8.4 \times 10^{11} \text{ W/cm}^2$.

arguments. In Sec. 10.2.2 it was seen that the linear polarization axis of the probe field coincides with the principal axis of the OCS molecule, i. e. with the nodal planes of both degenerate HOMO orbitals, suppression of the electron emission in this direction is expected. Emission along this axis is symmetry forbidden. An overall decrease in the ionization yield is likewise expected and also consistent with the observations.

As previously described one concern is if the presence of the YAG laser field can in some way perturb the ionization pathway and thus the experimental outcome. For that reason the angular dependence of the ionization yield is measured from field-free aligned molecules, Fig. 12.2. The experimental conditions for obtaining field-free alignment are equal to the ones described in Chapter 7 and Chapter 10. At a time delay between the probe and alignment pulse of 40.5 ps corresponding to the peak of the half J revival of OCS an alignment degree of $\langle \cos^2 \theta_{2D} \rangle = 0.84$ is obtained. Ionization yield is extracted from the total electron signal measured at an intensities of the probe beam corresponding $I_{\text{probe, low}} = 1.50 \times 10^{14} \text{ W/cm}^2$. Figure 12.2 provides a comparison of the angle dependent ionization yield of single ionization of OCS molecules as a function of the angle between the polarization of the alignment and probe laser pulse,

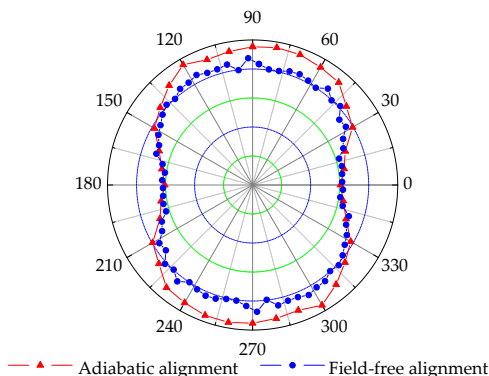


Figure 12.2: Measured ionization yield as a function of the angle between the polarization axis of the aligning and ionizing (probe) beam. The angle dependent ionization yield from field-free aligned molecules is compared to adiabatically aligned molecules with the YAG field present. The intensity of the nonadiabatic laser pulse used to induce nonadiabatic alignment is $I_{\text{align}, 800 \text{ nm}} = 8.3 \times 10^{12} \text{ W/cm}^2$, whereas the intensity of the adiabatic (YAG) laser field is $I_{\text{align}, \text{YAG}} = 8.4 \times 10^{11} \text{ W/cm}^2$. The intensity of the probe beam in the measurement is $I_{\text{probe}} = 1.50 \times 10^{14} \text{ W/cm}^2$. The ionization yield has been normalized to the total ionization yield obtained when only the ionizing laser is included.

between field-free aligned and adiabatically aligned molecules. The ionization signal from field-free aligned OCS molecules exhibits similar angular dependence as seen for adiabatically aligned molecules with a clear suppression of the ion yield when the polarization of the probe pulse is along the internuclear axis and a clear enhancement at 90° . The only discrepancy lies in the contrast between $\Delta\beta = 0^\circ$ and 90° , with the biggest difference observed for adiabatic alignment. This minor difference can be explained by the slightly worse confinement of the field-free aligned molecules with a $\langle \cos^2 \theta_{2D} \rangle = 0.84$ compared to $\langle \cos^2 \theta_{2D} \rangle = 0.90$ obtained from adiabatic alignment. The overall agreement between the measurements, however, provide a good indication that the presence of the YAG field does not perturb the ionization.

Next, the angular dependence of single ionization of benzonitrile (BN, $\text{C}_7\text{H}_5\text{N}$) molecules is investigated. Alignment is induced in the adiabatic regime from a 10 ns long YAG laser pulse under conditions equal to the ones described in Chapter 11. The intensity of the probe pulse in these experiment is $1.2 \times 10^{14} \text{ W/cm}^2$ and the ionization yield is extracted from the total electron signal resulting from single ionization. First the angular dependence of 1D aligned molecules is measured (Fig. 12.3 a). As opposed to OCS, a clear enhancement of

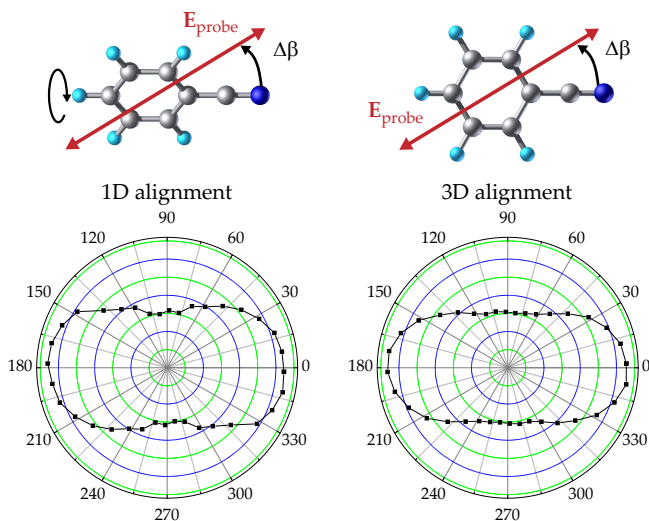


Figure 12.3: Measured ionization yield as a function of the angle between the major polarization axis of the aligning and ionizing (probe) beam. In **a** benzonitrile is 1D aligned and in **b** benzonitrile is 3D aligned. Alignment is created in the adiabatic regime from a 10 ns long YAG pulse. The total intensity of the YAG pulse, $7.7 \times 10^{11} \text{ W/cm}^2$, is the same for the linearly polarized pulse used to induce 1D alignment as for the elliptically polarized pulse with an intensity ratio between the major and minor axis of 3:1, used to induce 3D alignment. The intensity of the probe beam in the measurements is $I_{\text{probe}} = 1.23 \times 10^{14} \text{ W/cm}^2$. The ionization yield has been normalized to the total ionization yield obtained when only the ionizing laser is included.

the signal is observed when the polarization of the alignment and probe pulse are parallel, and a clear suppression is observed in a perpendicular geometry. As previously described $\text{C}_7\text{H}_5\text{N}$ is an asymmetric top molecule and the linearly polarized alignment pulse only confines the C-CN symmetry axis of the molecule, while the benzene ring remains free to rotate around this axis. Additional confinement of the molecular plane, and thus 3D alignment and orientation, is obtained by using an elliptically polarized alignment pulse with the major axis along the static field axis and the minor axis vertical in the images. The total intensity, $7.7 \times 10^{11} \text{ W/cm}^2$, is the same as for the linearly polarized pulse and the intensity ratio between the major and minor axis is 3:1. The angular dependence of the ion yield from 3D aligned molecules is shown in Fig. 12.3 b. The total ionization yield has been normalized to that obtained from unaligned molecules.

As for 1D aligned molecules a clear enhancement of the signal is observed at $\Delta\beta = 0^\circ$, where $\Delta\beta$ now is the angle between the major axis of the elliptically polarized YAG pulse and the polarization axis of the probe pulse.

In summary we have seen that the ionization yield depends strongly on the molecular alignment with respect to the polarization of the ionizing pulse. The interpretation of the data is not straightforward and represents new challenges for theory in the description of even the first ionization step.

It should be noted that these types of alignment dependent ionization yield do not hold any information of the orientation of the dipole moment of a polar molecule, even though the molecules were oriented in the present studies.

A different approach to molecular frame angle dependent ionization yields has been proposed by Corkum and coworkers [134]. In their experiments the MFPADs are linked to the angle dependent ionization probability from ionization by a circular probe pulse. These experiments are in close resemblance with the experiment shown in the Chapter 10 and Chapter 11. However, due to the lack of 3D resolution in our experimental setup, similar information cannot be extracted from our measurements at present.

13

CONCLUSIONS AND OUTLOOK

In conclusion, it has been shown that deflection of cold molecular beams with an inhomogeneous static electric field enables the selection and the spatial separation of the most polar quantum states, i. e. the lowest-lying rotational states. The method demonstrated here is complementary to state-selection for small molecules using a hexapole focuser, which has been suggested to be applied for improved alignment and orientation experiments [31] and recently been experimentally demonstrated [32]. While a hexapole focuser only works for small molecules in low-field seeking quantum states, beam deflection will apply broadly to a wide range of molecules, from diatomics to large biomolecules. The deflection is strongest for molecules with a large permanent dipole moment to mass ratio. For a given molecule the deflection is optimized by employing stronger deflection fields, increasing the length of the deflector, or lowering the speed of the molecule, for instance, by using neon rather than helium as a carrier gas. For small molecules, the preparation of an ensemble of molecules all in a single quantum state should be feasible.

As an application of the quantum-state-selected molecules it was shown that selection of carbonylsulfide and iodobenzene in low lying rotational states allows to achieve unprecedented degrees of laser-induced 1-dimensional (1D) adiabatic alignment and mixed laser- and static-field 1D orientation. The method was also extended to include laser-induced adiabatic 3-dimensional (3D) align-

ment and mixed field 3D orientation as demonstrated on 2,6-difluoroiodobenzene. In particular, we demonstrated that strong alignment and orientation can be maintained even when the intensity of the alignment pulse is lowered to the $10^{10} - 10^{11}$ W/cm² range. This can reduce unwanted disturbance from the laser field in future applications of adiabatically aligned or oriented molecules. We note that it should be possible to improve the degree of orientation obtained here simply by increasing the static electric field. Due to experimental constraints it was not implemented in the present work.

As an application of strongly aligned and oriented molecules photoelectron angular distributions (PADs) were measured from 1D aligned carbondisulfide, 1D oriented carbonylsulfide and 3D oriented benzonitrile.

I believe our method will prove useful in a number of areas in molecular science, a few of which are highlighted below.

13.1 Cleaning the Molecular Sample

13.1.1 Conformer Selection

For large (bio-)molecules, typically multiple structural isomers (conformers) [183] are present even at the low temperatures in a supersonic jet [184]. Just as random orientation of a molecular ensemble can lead to blurring of molecular properties measurements, the presence of different stereoisomers within a sample can give rise to misinterpretation in the studies of molecular dynamics as the measurements become an average over the properties of all the stereoisomers. Conformers of a specific biomolecule have the same mass, but differ by the relative orientation of their functional groups. Typically these functional groups have large local dipole moments associated with them and therefore the individual conformers often exhibit large, and largely different dipole moments. As described in Chapter 4, passing polar molecules through a strong inhomogeneous electric field will spatially disperse them according to their effective dipole moment and can thus be exploited to spatially separate conformers. Such separation has been demonstrated in an alternating gradient focusing selector for the *cis*- and *trans*-conformers of 3-aminophenol [87].

Recently we have demonstrated that the static field of the deflector can also be used to spatially isolate individual conformers of polar molecules [185].

To demonstrate the separation of stereoisomers of complex molecules using the electrostatic beam deflector experiments were performed on the *cis*- and *trans*-conformers of 3-aminophenol. The dipole moment of *cis*-3-aminophenol ($\mu_0 = 2.33$ D) is considerably larger than that of *trans*-3-aminophenol ($\mu_0 = 0.77$ D), hence a strong spatial separation of the states of the two conformers is expected as illustrated in Fig. 13.1 a). Applying the experimental setup de-

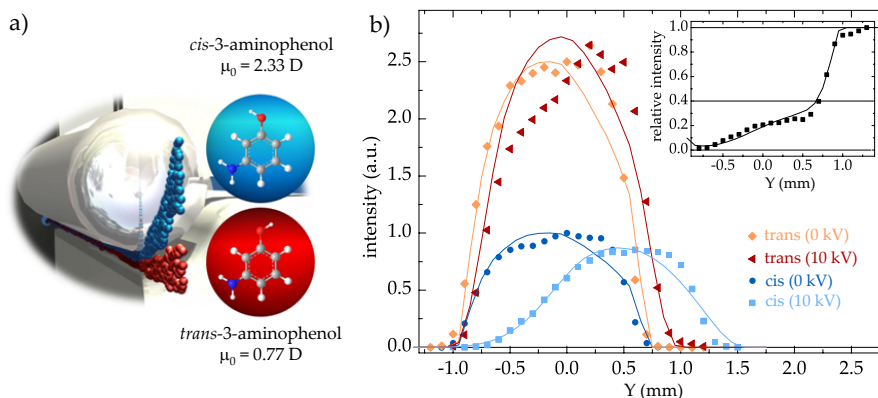


Figure 13.1: a) Illustration of the spatial separation of conformers in the electrostatic beam deflector. b) Molecular beam intensity as a function of the vertical position Y of the detection laser for *cis*- and *trans*-3-aminophenol. Experimental data are given by symbols, and simulations by solid lines. The vertical profiles of the undeflected beams of *cis*- and *trans*-3-aminophenol are shown as circles (dark blue) and diamonds (orange), respectively. Squares (light blue) and triangles (red): corresponding deflection profiles with high voltage (10 kV) applied to the deflector. Inset: the fractional population of the *cis* conformer, which is obtained by dividing the *cis* intensity by the sum of the intensities of *cis* and *trans* at the respective height Y ; the horizontal line indicates the value in the original beam.

scribed in Chapter 3 a few mbar of 3-aminophenol seeded in ~ 90 bar of He is expanded into vacuum from our Even-Lavie valve and passed through the electrostatic beam deflector.

Figure 13.1 b) shows the conformer-selective deflection profiles. The density of a specific conformer is measured by resonance enhanced multiphoton ionization (REMPI) by a pulsed dye laser (Lambda Physik, ScanMate2) as a function of the laser focus, Y . The two conformers of 3-aminophenol are measured individually at resonant excitation wave numbers corresponding to 34109 cm^{-1} for the *cis*- and 34467 cm^{-1} for the *trans*-conformer. When 10 kV is applied to the deflector both conformers are deflected upwards. However, the shift is considerably larger for the more polar *cis* conformer and above $Y = 1.0$ mm a pure sample of the *cis* conformer exist. Additionally, due to the effective cooling (~ 1 K) of the initial molecular beam the population of *cis*-3-aminophenol is almost depleted for heights smaller than $Y = -0.75$ mm and a pure sample of *trans*-3-aminophenol is obtained. The clean separation of the two conformers is also confirmed by the vibrationally resolved REMPI spectrum shown in Fig. 13.2. The spectrum measured in the deflected part of the molecular beam

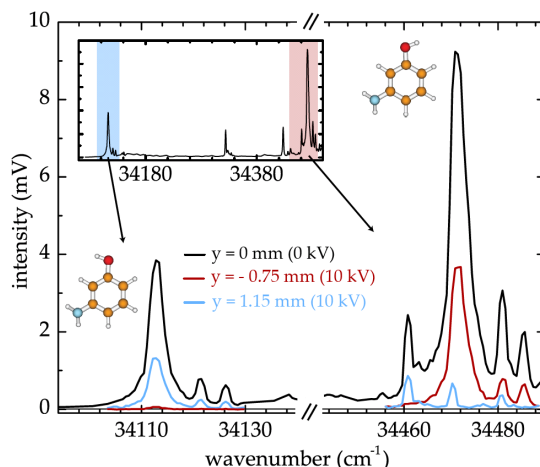


Figure 13.2: UV spectra of 3-aminophenol for the original beam (black), the deflected ensemble (blue), and the depleted beam (red). The spectral signatures and the complete discrimination of the individual conformers are thus demonstrated.

($Y = 1.15$ mm) only contains bands arising from *cis*-3-aminophenol. In contrast, the spectrum measured in the depleted beam ($Y = -0.75$ mm) exhibits features only assigned to the *trans* conformer. As a further consequence of the beam deflection, the lowest rotational states of the *cis* conformer are deflected the most, hence, a clean sample of *cis*-3-aminophenol can be selected in the lowest rotational states. Furthermore increasing the deflection for instance as described in Chapter 4 by lowering the speed of the molecules by changing the carrier gas from He to Ne, it should be possible to completely deflect the *cis* conformer away and instead select the *trans* conformer in the lowest rotational states.

The unprecedented control over the molecular ensemble may prove extremely important in stereospecific experiments on conformer- and state-selected samples.

13.1.2 Isolating Molecules from the Carrier Gas

Getting access to cold molecules in the gas phase typically involves using a molecular beam from a supersonic expansion. Consequently, the target usually consists of more than 99% carrier gas and less than 1% of the specific molecules. In several types of experiments the carrier gas can contribute to the particular signal measured, in fact so much that the molecular signal can be completely overshadowed by the signal from the atomic carrier gas. A polar molecule

can be separated from the unpolar carrier gas and thus completely remove the carrier gas background. This could be highly relevant in photoelectron spectroscopy with vacuum-ultraviolet (VUV), extreme-ultraviolet (EUV) [186], or X-ray light sources, including attosecond pulses, or in high harmonic generation experiments with femtosecond laser pulses [187].

13.2 Alingment and Orientation

It was shown experimentally that 1D and 3D alignment and orientation (Chapter 5 and Chapter 6) is significantly improved when a subset of molecules reside in the lowest rotational states are selected as targets. Alignment was induced in the adiabatic regime, where the turn-on and turn-off time of the linearly- (1D alignment) or elliptically- (3D alignment) polarized laser field occur slowly compared to the inherent rotational periods of the molecules. In addition, orientation was induced by the combined action of the laser field and a weak static electric field.

3D alignment and orientation was demonstrated for 2,6-difluoriodobenzene. For this specific molecule the major polarizability axis is parallel to the direction of the permanent dipole moment. Consequently, 3D orientation was achieved by positioning the major polarization axis of the elliptically-polarized laser pulse along the direction of the static electric field. For molecules having their permanent dipole moment coinciding with the major polarizability axis the method described in this thesis will be generally applicable. For a large number of molecules this, however, is not the case. Achieving 3D alignment for the molecules with the permanent dipole moment off-axis with respect to the major polarizability axis attracts special interest, since examples include important biomolecules such as amino acids and nucleic acids. I believe 3D orientation can also be achieved for a large fraction of these molecules by turning the 3D aligned molecule, i. e. rotating the axes of the elliptically polarized laser pulse, such that the permanent dipole moment coincides with the static field direction. It is important to remember, however, that the dipole interaction can only confine one axis, hence the "head versus tail" order can only be established along the permanent dipole moment axes. Depending on the molecule this may or may not be enough to completely confine all axis of the molecule.

13.2.1 Nonadiabatic Alignment and Orientation

It was seen in Chapter 7 that nonadiabatic alignment induced by laser pulses that are turned on and/or off rapidly compared to the molecular rotational periods benefit significantly from selection of the lowest rotational quantum

states. Nonadiabatic alignment was only briefly discussed. Selection of rotational states is, however, highly advantageous for nonadiabatic laser-induced schemes to control the spatial orientation of molecules, as recently demonstrated for NO molecules [32, 33].

For some applications a high degree of field-free alignment and orientation is required. The main strategy applied in this thesis has been to prepare as cold a sample of molecules as possible in order to optimize the degree of alignment. A different approach is to design the optimal laser pulse for nonadiabatic alignment [188].

Obtaining field-free 3D alignment and orientation may be possible by, for instance, using timed perpendicularly-polarized short pulses [125] or by truncating an adiabatic pulse to produce switched wave packets. In the case of 1D alignment and orientation, it has been shown that such a conversion from adiabatic alignment (orientation) to field-free alignment (orientation) is possible by femtosecond truncation of the adiabatic pulse [30, 54, 55]. One consequence of the rapid turn-off method, or nonadiabatic alignment or orientation [32] in general, is that the alignment/orientation becomes transient, which could reduce the utility for several important applications.

13.2.2 Brute-Force Orientation

Brute-force orientation [5, 122], that is, the spatial orientation of polar molecules using strong dc electric fields will benefit from the state selected samples similar to what was demonstrated here. In fact, as the separation of quantum states in the deflector is based on the interaction strength of the molecules with the electric field, the states that are deflected most, are also oriented the most inside the fields. To illustrate the achievable orientation, Frank Filsinger has calculated the ensemble averaged orientation in a homogeneous electric field of 250 kV/cm for iodobenzene for a thermal ensemble of 1 K. For this ensemble $\langle \cos^2 \theta_{2D} \rangle = 0.757$ is obtained. For a deflected, quantum-state-selected sample of iodobenzene molecules at 1 % of the undeflected peak intensity (see Table 4.1, Chapter 4), an increased ensemble averaged orientation of $\langle \cos^2 \theta_{2D} \rangle = 0.905$ is predicted.

13.3 Applications of Strongly Aligned or Oriented Molecules

The results presented here show that molecular frame PADs can be obtained for a broad range of species independent of whether 1D or 3D orientation is needed

to fully fix the molecule in space. Strong-field ionization by femtosecond circularly polarized pulses is an ultrafast probe, sensitive to molecular properties such as nodal planes. The field drives the electrons monotonously away from the parent ion without rescattering effects blurring the ionization dynamics. A particularly interesting extension is time-dependent phenomena where a pump pulse initiates a molecular transformation or reaction. The strong-field ionization probe used here is sensitive to the charge distribution of the valence electrons and could provide an efficient and ultrafast probe of, for instance, charge migration processes in molecules [189]. More generally, molecular frame PADs using laser oriented molecules will also be highly relevant for X-ray probing of molecular dynamics where detection of high energy electrons can provide a direct structural diagnostics of the changing molecular species [190].

In general, the ability to achieve very high degrees of alignment and orientation is of great interest for a number of applications. In addition to PADs from fixed in space molecules, state-selected and even conformer-selected molecules could be very beneficial for areas such (ultrafast) diffraction with electron or X-ray sources [47, 48] and time-resolved studies of light-induced stereochemistry [183].

Furthermore, Janssen and coworkers have shown that the ability to select a single rotational state with a hexapole focuser enables new possibilities for studying directional dynamics of fragments in photodissociation of small molecules [102]. The deflection method can strongly broaden the number of molecules to which single rotational state selection, and subsequent orientation, is possible. In particular, it will offer access to studies of photoinitiated processes in oriented targets of larger asymmetric tops.

13.3.1 Manipulating the Torsion of Molecules

So far manipulation of the external degrees of freedom of gas phase molecules has been described. However, manipulation by induced dipole forces can also be applied to the internal degrees of freedom such as vibrational motion [191]. Modification of energy potential barriers with pulsed laser fields have been applied to photoinduced bond breaking of small molecules to yield a desired final product [55, 192]. In collaboration with the group of Lars B. Madsen we have demonstrated that the laser-induced nonresonant polarizability interaction, not only can induce molecular alignment, but can also be used to influence the internal rotation of an axially chiral molecule around the stereogenic C-C bond axis [193, 194]. In the experiments the C-C bond axis of a substituted biphenyl molecules (3,5-difluoro-3',5'-dibromobiphenyl) is fixed in space by adiabatic alignment with a 10 ns long laser pulse. A short femtosecond (kick) pulse linearly polarized perpendicular to the fixed axis, initiated torsional motion of the two

phenyl rings and sets the molecule into rotation around the stereogenic axis. By recording F^+ and Br^+ ion fragments by time-resolved Coulomb explosion it is possible to follow the internal as well as the external rotational motion. 3,5-difluoro-3',5'-dibromobiphenyl has two conformations that are mirror images of each other, the R_a and S_a enantiomers illustrated in Fig. 13.3.

The dihedral angle between the two phenyl rings, i. e. the twisting angle between the two phenyl rings, is controlled by transiently modification of the field-free potential curve by a femtosecond kick pulse as illustrated in Fig. 13.3. Oscillations in the dihedral angle have been observed experimentally as well as theoretically [193, 194].

A perspective of the demonstrated laser control of the torsional motion is time-resolved study of deracemization, hence following the dynamics involved when one enantiomer is steered into its mirror form. Calculations predict that by increasing the field-strength of the kick pulse and applying the right geometry of the laser pulse polarizations can lead to a selective conversion from a racemate to yield a pure enantiomer. Discrimination between the two enantiomer-forms experimentally requires that the inversion symmetry of the C-C bond axis is broken. The ability to strongly 3-dimensionally orient molecules selected in the lowest rotational states by the electrostatic beam deflection as described in this thesis will enable us experimentally to discriminate between the two enantiomers, thus facilitate time-resolved studies of deracemization and selective conversion to a pure enantiomer, predicted by theory, but thus far not observed experimentally.

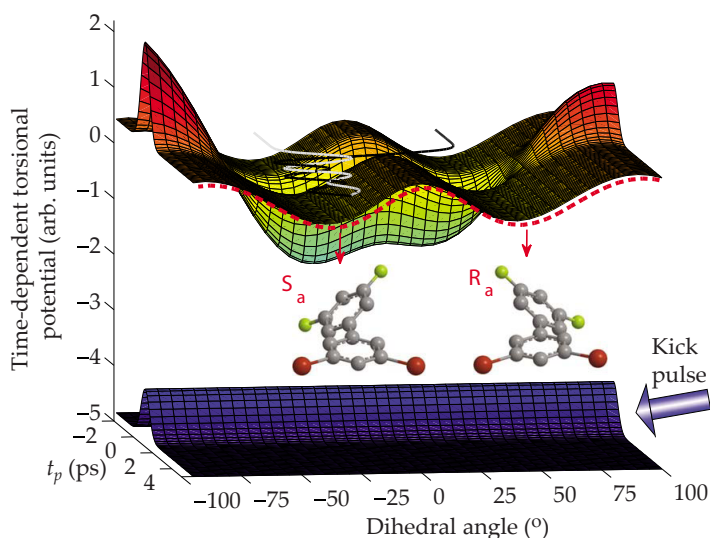


Figure 13.3: Calculated kick pulse induced time-dependent torsional potential as a function of t_p measured with respect to the center of the pulse and dihedral angle between the Br and F-phenyl planes. The asymmetry in the potential is obtained by orienting the molecules (here with the Br-phenyl plane out of the paper), 3-dimensionally aligning them, and by polarizing the kick pulse at an angle of 13° with respect to the second most polarizable axis. The red dashed curve illustrates the field-free torsional potential. The black and the grey curves illustrate torsional paths of motion. For the S_a enantiomer the time varying potential induces an oscillatory motion (gray curve) corresponding to torsion confined within the initial well. By contrast, due to the induced asymmetry between the two wells, the initial R_a enantiomer is traversing the central torsional barrier, and ends up as an S_a enantiomer undergoing internal rotation (black curve). The kick pulse has a peak intensity of 1.2×10^{13} W/cm² and a duration of 1.0 ps (FWHM). The simulations have been performed in the group of Lars B. Madsen.

14

SUMMARY

Molecular properties and dynamics depend strongly on the direction from where they are "viewed" or probed and the spatial orientation of a molecule is of crucial importance in its interaction with other molecules, atoms or electromagnetic radiation. In normal gas-phase experiments molecules are randomly oriented and averaging over molecular orientations can lead to blurring and potential loss of information. Historically the drive for seeking control over the spatial orientation of a molecule came from the possibility to control or enhance molecular reactivity and interactions. Since then it has found wide spread interest in many areas of physics and chemistry. Large efforts have been devoted to the development of new methods to enable control over the alignment and orientation of gas phase molecules.

In this thesis molecular alignment is induced by the electric field from non-resonant, non-ionizing moderately intense laser pulses and additional orientation of polar molecules is achieved by the combined action of the laser and a weak static electric field. Here alignment refers to confinement of molecule fixed axes along laboratory fixed axes, and orientation refers to the molecular dipole moment pointing in a particular direction. Laser induced alignment is a very versatile approach to orientational control, generally applicable to any molecule with an anisotropic polarizability. Any application of aligned or oriented molecules will benefit significantly or simply require a strong degree of

molecular confinement. An efficient method to optimize the degree of alignment or orientation is to ensure that the molecular sample initially resides in the lowest lying rotational states. Strong internal cooling to sub Kelvin temperatures can be provided from a supersonic expansion of the molecules in an inert carrier gas and very strong degrees of alignment have been demonstrated using such molecular beams. However, orientation in the mixed laser and static field method imposes an even stronger requirement on the initial rotational state distribution. For that purpose additional selection of the lowest lying rotational quantum states by deflection of a cold beam of polar molecules in an inhomogeneous static electric field was demonstrated. The underlying ideas can be dated back to the 1920s, where it was proposed that electrostatic deflection should be able to spatially disperse the rotational quantum states of the molecule, enabling quantum-state selectivity. In particular the ground state experiences the largest Stark shift and molecules residing in this state are deflected the most. The goal of our experiment is to isolate and use rotational ground-state molecules, or at least samples of molecules in the lowest-lying rotational states as targets for further experiments. So far selection of carbonylsulfide and iodobenzene in the low lying rotational states has demonstrated unprecedented degrees of laser-induced adiabatic 1-dimensional alignment and mixed laser- and static-field 1-dimensional orientation. The method was extended to include laser-induced adiabatic 3-dimensional alignment and mixed field 3-dimensional orientation as demonstrated on 2,6-difluoriodobenzene. In particular, strong alignment and orientation can be maintained even when the intensity of the alignment pulse is lowered to the $10^{10} - 10^{11}$ W/cm² range. This can reduce unwanted disturbance from the laser field in future applications of adiabatically aligned or oriented molecules.

The main focus of this thesis is on adiabatic alignment and orientation, however also field-free alignment induced by laser pulses with durations that are sufficiently short compared to the rotational timescale for the molecule, can be achieved and benefits greatly from quantum-state-selected molecules as targets.

The prospect of confining an ensemble of molecules to the laboratory frame opens the door to various experimental studies from the molecules "*point of view*". As an application of strongly aligned and oriented molecules molecular frame photoelectron angular distributions (MFPADs) from strong field ionization in the multiphoton and tunneling regimes are measured. For 1-dimensionally aligned CS₂ the angular distributions of photoelectrons from multiphoton ionization with intense linearly polarized 25 fs laser pulses, show a significant dependence on the angle between the polarizations of the aligning and ionizing laser fields. For 1-dimensionally oriented OCS the MFPADs from tunnel ionization with intense, circularly polarized, 30 femtosecond laser pulses, exhibit pronounced anisotropies, perpendicular to the fixed permanent dipole

moment, that are absent in PADs from randomly oriented molecules. For 3-dimensionally oriented benzonitrile additional striking structures appear due to suppression of electron emission in nodal planes of the fixed electronic orbitals. In a theoretical analysis, relying on tunneling ionization theory, it is shown that the PADs reflect nodal planes, permanent dipole moments and polarizabilities of both the neutral molecule and its cation. The calculated results are exponentially sensitive to changes in these molecular properties thereby pointing to exciting opportunities for time-resolved probing of valence electrons dynamics by intense circularly polarized pulses.

At present, tremendous efforts are applied to developments of novel approaches for studying ultrafast molecular dynamics, sparked by emerging free-electron lasers. In that context samples of strongly aligned and oriented molecules as targets in electron or X-ray diffraction experiments, as well as MFPADs from ionization of localized inner shell electrons by XUV or X-ray pulses, will prove important.

Appendix



THE INFLUENCE OF THE CAPACITOR PLATES

As mentioned in Chapter 3 the "new" vacuum chamber system was modified after the initial experiments. The first 1 mm skimmer in the source chamber was replaced by a 3 mm skimmer of conical shape to ensure better cooling of the molecular beam. Furthermore, a set of capacitor plates were placed between the electrostatic beam deflector and the interaction region.

The idea of the capacitor plates is to preserve the M quantum number from the exit for the deflector to the interaction region. In the deflector the the field splits every field-free rotor state into $J + 1$ M -sub-levels. Every M -sub-level has a distinct effective dipole moment associated with it and will, thus, experience a different force in the field. However, if the molecules enter a field-free region between the deflector and the detection region, the M -sub-levels become exactly degenerate and the M quantum number no longer defined. When entering the extraction field of the velocity map imaging spectrometer, the angular momentum, J , is re-projected onto the field axis, and the molecule may end up in a different M sub-level. The molecule "looses" its memory concerning the M -quantum number that it had during the deflection. In principle, a very small

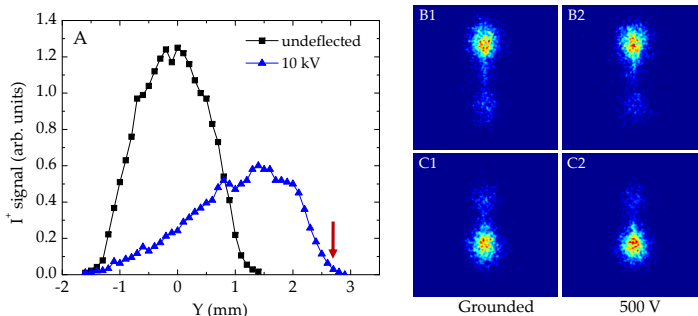


Figure A.1: A: Experimentally measured vertical spatial profile of the molecular beam of iodobenzene for different deflection voltages applied, measured by recording the I^+ signal. To the right I^+ images of deflected iodobenzene molecules recorded with the YAG laser polarized at 150° (B1 and B2) and 30° (C1 and C2) are shown for the capacitor plates grounded and at 500 V, respectively. The intensities of the YAG and probe pulse are 8×10^{11} W/cm² and 5×10^{14} W/cm², respectively. $E_{\text{stat}} = 595$ V/cm.

electric stray field is enough to preserve the projection of J onto the field-axis, i. e. the M quantum number. However, if the M -splitting becomes very small the probability to have transitions between different M -sub-levels increases.

To test the effect of the capacitor 1D alignment and mixed field orientation experiments were conducted on iodobenzene molecules seeded in Ne. Figure A.1 A shows the deflection profiles obtained for iodobenzene for undeflected molecules and with the deflector turned on at 10 kV. Due to the increased aperture of the first skimmer the deflection profile for the undeflected molecules is slightly broadened.

Several measurement of alignment and orientation were performed with barely any effect of the capacitor field observed. However, pushing the experimental conditions, i. e. going to the absolute edge of the most deflected molecules (indicated by an arrow in Fig. A.1 A) an effect was observed. Figure A.1 image B1 and C1, show the I^+ images of iodobenzene recorded with the YAG laser polarized at 150° and 30° , respectively, for the capacitor plates grounded. The number of I^+ ions detected in the upper half compared to the total number of ions in images B1 and C1 is 0.79 and 0.21, respectively. When the capacitor plates were turned on the asymmetry increased (Fig. A.1 image B2 and C2), and optimum orientation was found for the capacitor plates at a potential of 500V, with the number of I^+ ions detected in the upper half compared to the total num-

ber of ions increasing to 0.82 (image B2) and 0.19 (image C2).

The effect of the capacitor plates seems to be visible only when a subset of the lowest lying rotational states is selected, consistent with the increasing importance of preservation of the M -states for increasing state selectivity.

REFERENCES

- [1] A. Stolow, *Chemical physics: Molecular conformations fielded*, *Nature* **461**, 1063 (2009).
- [2] A. Rodger and B. Nordén, *Circular Dichroism and Linear Dichroism* (Oxford University Press, Oxford 1997).
- [3] D. H. Parker and R. B. Bernstein, *Oriented Molecule Beams via the Electrostatic Hexapole: Preparation, Characterization, and Reactive Scattering*, *Ann. Rev. Phys. Chem.* **40**, 561 (1989).
- [4] P. R. Brooks, *Reactions of Oriented Molecules*, *Science* **193**, 11 (1976).
- [5] H. J. Loesch and A. Remscheid, *Brute force in molecular reaction dynamics: A novel technique for measuring steric effects*, *J. Chem. Phys.* **93**, 4779 (1990).
- [6] B. Friedrich and D. R. Herschbach, *On the possibility of orienting rotationally cooled polar molecules in an electric field*, *Z. Phys. D* **18**, 153 (1991).
- [7] B. Friedrich and D. Herschbach, *Alignment and Trapping of Molecules in Intense Laser Fields*, *Phys. Rev. Lett.* **74**, 4623 (1995).
- [8] T. Seideman, *Rotational excitation and molecular alignment in intense laser fields*, *J. Chem. Phys.* **103**, 7887 (1995).
- [9] B. A. Zon and B. G. Katsnel'son, *Nonresonant scattering of intense light by a molecule*, *Sov. Phys.-JETP* **42**, 595 (1976).
- [10] D. Normand, L. A. Lompre, and C. Cornaggia, *Laser-induced molecular alignment probed by a double-pulse experiment*, *J. Phys. B* **25**, L497 (1992).

- [11] D. T. Strickland, Y. Beaudoin, P. Dietrich, and P. B. Corkum, *Optical studies of inertially confined molecular iodine ions*, Phys. Rev. Lett. **68**, 2755 (1992).
- [12] E. Constant, H. Stapelfeldt, and P. B. Corkum, *Observation of Enhanced Ionization of Molecular Ions in Intense Laser Fields*, Phys. Rev. Lett. **76**, 4140 (1996).
- [13] T. Seideman, M. Y. Ivanov, and P. B. Corkum, *Role of Electron Localization in Intense-Field Molecular Ionization*, Phys. Rev. Lett. **75**, 2819 (1995).
- [14] W. Kim and P. M. Felker, *Spectroscopy of pendular states in optical-field-aligned species*, J. Chem. Phys. **104**, 1147 (1996).
- [15] H. Sakai, C. P. Safvan, J. J. Larsen, K. M. Hilligsøe, K. Hald, and H. Stapelfeldt, *Controlling the alignment of neutral molecules by a strong laser field*, J. Chem. Phys. **110**, 10235 (1999).
- [16] J. J. Larsen, H. Sakai, C. P. Safvan, I. Wendt-Larsen, and H. Stapelfeldt, *Aligning molecules with intense nonresonant laser fields*, J. Chem. Phys. **111**, 7774 (1999).
- [17] F. Rosca-Pruna and M. J. J. Vrakking, *Experimental Observation of Revival Structures in Picosecond Laser-Induced Alignment of I_2* , Phys. Rev. Lett. **87**, 153902 (2001).
- [18] J. J. Larsen, K. Hald, N. Bjerre, H. Stapelfeldt, and T. Seideman, *Three Dimensional Alignment of Molecules Using Elliptically Polarized Laser Fields*, Phys. Rev. Lett. **85**, 2470 (2000).
- [19] J. G. Underwood, B. J. Sussman, and A. Stolow, *Field-Free Three Dimensional Molecular Axis Alignment*, Phys. Rev. Lett. **94**, 143002 (2005).
- [20] K. F. Lee, D. M. Villeneuve, P. B. Corkum, A. Stolow, and J. G. Underwood, *Field-Free Three-Dimensional Alignment of Polyatomic Molecules*, Phys. Rev. Lett. **97**, 173001 (2006).
- [21] A. Rouzée, S. Guérin, O. Faucher, and B. Lavorel, *Field-free molecular alignment of asymmetric top molecules using elliptically polarized laser pulses*, Phys. Rev. A **77**, 043412 (2008).
- [22] S. S. Viftrup, V. Kumarappan, S. Trippel, H. Stapelfeldt, E. Hamilton, and T. Seideman, *Holding and Spinning Molecules in Space*, Phys. Rev. Lett. **99**, 143602 (2007).

- [23] S. S. Viftrup, V. Kumarappan, L. Holmegaard, C. Z. Bisgaard, H. Stapelfeldt, M. Artamonov, E. Hamilton, and T. Seideman, *Controlling the rotation of asymmetric top molecules by the combination of a long and a short laser pulse*, Phys. Rev. A **79**, 023404 (2009).
- [24] B. Friedrich and D. Herschbach, *Enhanced orientation of polar molecules by combined electrostatic and nonresonant induced dipole forces*, J. Chem. Phys. **111**, 6157 (1999).
- [25] B. Friedrich and D. Herschbach, *Manipulating Molecules via Combined Static and Laser Fields*, J. Phys. Chem. A **103**, 10280 (1999).
- [26] H. Sakai, S. Minemoto, H. Nanjo, H. Tanji, and T. Suzuki, *Controlling the Orientation of Polar Molecules with Combined Electrostatic and Pulsed, Nonresonant Laser Fields*, Phys. Rev. Lett. **90**, 083001 (2003).
- [27] H. Tanji, S. Minemoto, and H. Sakai, *Three-dimensional molecular orientation with combined electrostatic and elliptically polarized laser fields*, Phys. Rev. A **72**, 063401 (2005).
- [28] U. Buck and M. Fárnik, *Oriented xenon hydride molecules in the gas phase*, Int. Rev. Phys. Chem. **25**, 583 (2006).
- [29] L. Cai, J. Marango, and B. Friedrich, *Time-Dependent Alignment and Orientation of Molecules in Combined Electrostatic and Pulsed Nonresonant Laser Fields*, Phys. Rev. Lett. **86**, 775 (2001).
- [30] A. Goban, S. Minemoto, and H. Sakai, *Laser-Field-Free Molecular Orientation*, Phys. Rev. Lett. **101**, 013001 (2008).
- [31] A. Gijsbertsen, W. Siu, M. F. Kling, P. Johnsson, P. Jansen, S. Stolte, and M. J. J. Vrakking, *Direct Determination of the Sign of the NO Dipole Moment*, Phys. Rev. Lett. **99**, 213003 (2007).
- [32] O. Ghafur, A. Rouzee, A. Gijsbertsen, W. K. Siu, S. Stolte, and M. J. J. Vrakking, *Impulsive orientation and alignment of quantum-state-selected NO molecules*, Nature Phys. **5**, 289 (2009).
- [33] A. Rouzée, A. Gijsbertsen, O. Ghafur, O. M. Shir, T. Bäck, S. Stolte, and M. J. J. Vrakking, *Optimization of laser field-free orientation of a state-selected NO molecular sample*, New J. Phys. **11**, 105040 (2009).
- [34] T. Kanai and H. Sakai, *Numerical simulations of molecular orientation using strong, nonresonant, two-color laser fields*, J. Chem. Phys. **115**, 5492 (2001).

- [35] M. Muramatsu, M. Hita, S. Minemoto, and H. Sakai, *Field-free molecular orientation by an intense nonresonant two-color laser field with a slow turn on and rapid turn off*, Phys. Rev. A **79**, 011403 (2009).
- [36] S. De, I. Znakovskaya, D. Ray, F. Anis, N. G. Johnson, I. A. Bocharova, M. Magrakvelidze, B. D. Esry, C. L. Cocke, I. V. Litvinyuk, and M. F. Kling, *Field-Free Orientation of CO Molecules by Femtosecond Two-Color Laser Fields*, Phys. Rev. Lett. **103**, 153002 (2009).
- [37] R. A. Bartels, T. C. Weinacht, N. Wagner, M. Baertschy, C. H. Greene, M. M. Murnane, and H. C. Kapteyn, *Phase Modulation of Ultrashort Light Pulses using Molecular Rotational Wave Packets*, Phys. Rev. Lett. **88**, 013903 (2002).
- [38] J. Itatani, J. Levesque, D. Zeidler, H. Niikura, H. Pépin, J. C. Kieffer, P. B. Corkum, and D. M. Villeneuve, *Tomographic imaging of molecular orbitals*, Nature **432**, 867 (2004).
- [39] V. Kumarappan, L. Holmegaard, C. Martiny, C. B. Madsen, T. K. Kjeldsen, S. S. Viftrup, L. B. Madsen, and H. Stapelfeldt, *Multiphoton Electron Angular Distributions from Laser-Aligned CS₂ Molecules*, Phys. Rev. Lett. **100**, 093006 (2008).
- [40] M. Meckel, D. Comtois, D. Zeidler, A. Staudte, D. Pavicic, H. C. Bandulet, H. Pepin, J. C. Kieffer, R. Dorner, D. M. Villeneuve, and P. B. Corkum, *Laser-Induced Electron Tunneling and Diffraction*, Science **320**, 1478 (2008).
- [41] C. Z. Bisgaard, O. J. Clarkin, G. Wu, A. M. D. Lee, O. Gessner, C. C. Hayden, and A. Stolow, *Time-Resolved Molecular Frame Dynamics of Fixed-in-Space CS₂ Molecules*, Science **323**, 1464 (2009).
- [42] T. Kanai, S. Minemoto, and H. Sakai, *Quantum interference during high-order harmonic generation from aligned molecules*, Nature (London) **435**, 470 (2005).
- [43] C. Vozzi, F. Calegari, E. Benedetti, J.-P. Caumes, G. Sansone, S. Stagira, M. Nisoli, R. Torres, E. Heesel, N. Kajumba, J. P. Marangos, C. Altucci, and R. Velotta, *Controlling Two-Center Interference in Molecular High Harmonic Generation*, Phys. Rev. Lett. **95**, 153902 (2005).
- [44] C. B. Madsen, A. S. Mouritzen, T. K. Kjeldsen, and L. B. Madsen, *Effects of orientation and alignment in high-order harmonic generation and above-threshold ionization*, Phys. Rev. A **76**, 035401 (2007).
- [45] Y. Mairesse, S. Haessler, B. Fabre, J. Higuier, W. Boutu, P. Breger, E. Constant, D. Descamps, E. Mävel, S. Petit, and P. Salières, *Polarization-resolved pompe-probe spectroscopy with high harmonics*, New J. Phys. **10**, 025028 (2008).

- [46] S. Ramakrishna and T. Seideman, *Torsional Control by Intense Pulses*, Phys. Rev. Lett. **99**, 103001 (2007).
- [47] J. C. H. Spence and R. B. Doak, *Single Molecule Diffraction*, Phys. Rev. Lett. **92**, 198102 (2004).
- [48] E. R. Peterson, C. Buth, D. A. Arms, R. W. Dunford, E. P. Kanter, B. Krässig, E. C. Landahl, S. T. Pratt, R. Santra, S. H. Southworth, and L. Young, *An x-ray probe of laser-aligned molecules*, App. Phys. Lett. **92**, 094106 (2008).
- [49] P. Johnsson, A. Rouzée, W. Siu, Y. Huismans, F. Lépine, T. Marchenko, S. Düsterer, F. Tavella, N. Stojanovic, A. Azima, R. Treusch, M. F. Kling, and M. J. J. Vrakking, *Field-free molecular alignment probed by the free electron laser in Hamburg (FLASH)*, J. Phys. B **42**, 134017 (2009).
- [50] R. Neutze, R. Wouts, D. van der Spoel, E. Weckert, and J. Hajdu, *Potential for biomolecular imaging with femtosecond X-ray pulses*, Nature (London) **406**, 752 (2000).
- [51] H. N. Chapman, A. Barty, M. J. Bogan, S. Boutet, M. Frank, S. P. Hau-Riege, S. Marchesini, B. W. Woods, S. Bajt, W. H. Benner, R. A. London, E. Plonjes, M. Kuhlmann, R. Treusch, S. Dusterer, T. Tschentscher, J. R. Schneider, E. Spiller, T. Moller, C. Bostedt, M. Hoener, D. A. Shapiro, K. O. Hodgson, D. van der Spoel, F. Burmeister, M. Bergh, C. Caleman, G. Huldt, M. M. Seibert, F. R. N. C. Maia, R. W. Lee, A. Szoke, N. Timneanu, and J. Hajdu, *Femtosecond diffractive imaging with a soft-X-ray free-electron laser*, Nature Phys. **2**, 839 (2006).
- [52] H. Stapelfeldt and T. Seidemann, *Colloquium: Aligning molecules with strong laser pulses*, Rev. Mod. Phys. **75**, 543 (2003).
- [53] T. Seideman and E. Hamilton, *Nonadiabatic alignment by intense pulses. Concepts, theory, and directions*, Ad. At. Mol. Opt. Phys. **52**, 289 (2006).
- [54] J. G. Underwood, M. Spanner, M. Y. Ivanov, J. Mottershead, B. J. Sussman, and A. Stolow, *Switched Wave Packets: A Route to Nonperturbative Quantum Control*, Phys. Rev. Lett. **90**, 223001 (2003).
- [55] B. J. Sussman, J. G. Underwood, R. Lausten, M. Y. Ivanov, and A. Stolow, *Quantum control via the dynamic Stark effect: Application to switched rotational wave packets and molecular axis alignment*, Phys. Rev. A **73**, 053403 (2006).
- [56] B. Friedrich and D. Herschbach, *Polarization of Molecules Induced by Intense Nonresonant Laser Fields*, J. Phys. Chem. **99**, 15686 (1995).

- [57] D. J. Griffith, *Introduction to Quantum Mechanics* (Prentice Hall 1995).
- [58] J. Ortigoso, M. Rodriguez, M. Gupta, and B. Friedrich, *Time evolution of pendular states created by the interaction of molecular polarizability with a pulsed nonresonant laser field*, J. Chem. Phys. **110**, 3870 (1999).
- [59] R. Torres, R. de Nalda, and J. P. Marangos, *Dynamics of laser-induced molecular alignment in the impulsive and adiabatic regimes: A direct comparison*, Phys. Rev. A **72**, 023420 (2005).
- [60] V. Kumarappan, C. Z. Bisgaard, S. S. Viftrup, L. Holmegaard, and H. Stapelfeldt, *Role of rotational temperature in adiabatic molecular alignment*, J. Chem. Phys. **125**, 194309 (2006).
- [61] P. Felker, *Rotational coherence spectroscopy: studies of the geometries of large gas-phase species by picosecond time-domain methods*, J. Phys. Chem. **96**, 7844 (1992).
- [62] P. M. Felker and A. H. Zewail, *Molecular Structures from Ultrafast Coherence Spectroscopy*, in *Femtosecond Chemistry*, edited by J. Manz and L. Wöste (VCH (Weinheim) 1995), pp. 193–260.
- [63] C. H. Lin, J. P. Heritage, and T. K. Gustafson, *Susceptibility Echos in Linear Molecular Gases*, Apl. Phys. Lett. **19**, 397 (1971).
- [64] J. P. Heritage, T. K. Gustafson, and C. H. Lin, *Observation of Coherent Transient Birefringence in CS₂ Vapor*, Phys. Rev. Lett. **34**, 1299 (1975).
- [65] P. W. Joireman, L. L. Connell, S. M. Ohline, and P. M. Felker, *Characterization of asymmetry transients in rotational coherence spectroscopy*, J. Chem. Phys. **96**, 4118 (1992).
- [66] I. S. Averbukh and R. Arvieu, *Angular Focusing, Squeezing, and Rainbow Formation in a Strongly Driven Quantum Rotor*, Phys. Rev. Lett. **87**, 163601 (2001).
- [67] M. Leibscher, I. S. Averbukh, and H. Rabitz, *Molecular Alignment by Trains of Short Laser Pulses*, Phys. Rev. Lett. **90**, 213001 (2003).
- [68] M. Leibscher, I. S. Averbukh, and H. Rabitz, *Enhanced molecular alignment by short laser pulses*, Phys. Rev. A **69**, 013402 (2004).
- [69] V. Renard, M. Renard, S. Guérin, Y. T. Pashayan, B. Lavorel, O. Fraucher, and H. R. Jauslin, *Postpulse Molecular Alignment Measured by a Weak Field Polarization Technique*, Phys. Rev. Lett. **90**, 153601 (2003).

- [70] S. Zamith, Z. Ansari, F. Lepine, and M. J. J. Vrakking, *Single-shot measurement of revival structures in femtosecond laser-induced alignment of molecules*, *Opt. Lett.* **30**, 2326 (2005).
- [71] J. J. Larsen, I. Wendt-Larsen, and H. Stapelfeldt, *Controlling the Branching Ratio of Photodissociation Using Aligned Molecules*, *Phys. Rev. Lett.* **83**, 1123 (1999).
- [72] M. D. Poulsen, E. Skovsen, and H. Stapelfeldt, *Photodissociation of laser aligned iodobenzene: Towards selective photoexcitation*, *J. Chem. Phys.* **117**, 2097 (2002).
- [73] E. Péronne, M. D. Poulsen, C. Z. Bisgaard, H. Stapelfeldt, and T. Seideman, *Nonadiabatic Alignment of Asymmetric Top Molecules: Field-Free Alignment of Iodobenzene*, *Phys. Rev. Lett.* **91**, 043003 (2003).
- [74] S. Backus, C. G. Durfee III, M. M. Murnane, and H. C. Kapteyn, *High power ultrafast lasers*, *Rev. Sci. Instr.* **69**, 1207 (1998).
- [75] J. C. Diels and W. Rudolph, *Ultrashort laser pulse phenomena* (Academic Press 1996).
- [76] L. Holmegaard, *Control of Alignment Dynamics of Asymmetric Top Molecules*, Master's thesis, Department of Chemistry, Aarhus University (2006).
- [77] C. Rullière (editor), *Femtosecond Laser Pulses. Principles and Experiments* (Springer, Berlin 2003), second edition.
- [78] G. P. Agrawal, *Nonlinear Fiber Optics* (Academic Press 2001), third edition.
- [79] CVI. *Optical components and assemblies*, <http://www.cvilaser.com> (2010).
- [80] F. L. Pedrotti and L. S. Pedrotti, *Introduction to Optics* (Prentice Hall 1993), second edition.
- [81] M. Hillenkamp, S. Keinan, and U. Even, *Condensation limited cooling in supersonic expansions*, *J. Chem. Phys.* **118**, 8699 (2003).
- [82] U. Even, J. Jortner, D. Noy, N. Lavie, and C. Cossart-Magos, *Cooling of large molecules below 1 K and He clusters formation*, *J. Chem. Phys.* **112**, 8068 (2000).
- [83] D. H. Levy, *The Spectroscopy of Very Cold Gasses*, *Science* **214**, 263 (1981).

- [84] A. T. J. B. Eppink and D. H. Parker, *Velocity map imaging of ions and electrons using electrostatic lenses: Application in photoelectron and photofragment ion imaging of molecular oxygen*, Rev. Sci. Instr. **68**, 3477 (1997).
- [85] D. H. Parker and A. T. J. B. Eppink, *Photoelectron and photofragment velocity map imaging of state-selected molecular oxygen dissociation/ionization dynamics*, J. Chem. Phys. **107**, 2357 (1997).
- [86] B. Friedrich and D. R. Herschbach, *Spatial Orientation of Molecules in Strong Electric Fields and Evidence for Pendular States*, Nature (London) **353**, 412 (1991).
- [87] F. Filsinger, U. Erlekam, G. von Helden, J. Küpper, and G. Meijer, *Selector for Structural Isomers of Neutral Molecules*, Phys. Rev. Lett. **100**, 133003 (2008).
- [88] J. Levesque, Y. Mairesse, N. Dudovich, H. Pépin, J.-C. Kieffer, P. B. Corkum, and D. M. Villeneuve, *Polarization State of High-Order Harmonic Emission from Aligned Molecules*, Phys. Rev. Lett. **99**, 243001 (2007).
- [89] M. G. Tenner, E. W. Kuipers, W. Y. Langhout, A. W. Kleyn, G. Nicolaisen, and S. Stolte, *Molecular beam apparatus to study interactions of oriented NO and surfaces*, Surface Science **236**, 151 (1990).
- [90] H. Kallmann and F. Reiche, *Über den Durchgang bewegter Moleküle durch inhomogene Kraftfelder*, Z. Phys. **6**, 352 (1921).
- [91] E. Wrede, *Über die Ablenkung von Molekularstrahlen elektrischer Dipolmoleküle im inhomogenen elektrischen Feld*, Z. Phys. **44**, 261 (1927).
- [92] O. Stern, *Zur Methode der Molekularstrahlen. I*, Z. phys. **39**, 751 (1926).
- [93] I. I. Rabi, S. Millman, P. Kusch, and J. R. Zacharias, *The molecular beam resonance method for measuring nuclear magnetic - Moments the magnetic moments of Li-3(6) Li-3(7) and F-9(19)*, Phys. Rev. **55**, 526 (1939).
- [94] H. G. Bennewitz and W. Paul, *Eine Methode zur Bestimmung von Kernmomenten mit fokussiertem Atomstrahl*, Z. Phys. **139**, 489 (1954).
- [95] H. G. Bennewitz, W. Paul, and C. Schlier, *Fokussierung polarer Moleküle*, Z. Phys. **141**, 6 (1955).
- [96] J. P. Gordon, H. J. Zeiger, and C. H. Townes, *Molecular Microwave Oscillator and New Hyperfine Structure in the Microwave Spectrum of NH₃*, Phys. Rev. **95**, 282 (1954).

- [97] J. P. Gordon, H. J. Zeiger, and C. H. Townes, *The Maser-New Type of Microwave Amplifier, Frequency Standard, and Spectrometer*, Phys. Rev. **99**, 1264 (1955).
- [98] H. G. Bennewitz, K. H. Kramer, J. P. Toennies, and W. Paul, *Messung der Anisotropie des van der Waals-Potentials durch Streuung von Molekülen in definiertem Quantenzustand*, Z. Phys. **177**, 84 (1964).
- [99] P. R. Brooks and E. M. Jones, *Reactive Scattering of K Atoms from Oriented CH₃I Molecules*, J. Chem. Phys. **45**, 3449 (1966).
- [100] R. J. Beuhler, R. B. Bernstein, and K. H. Kramer, *Observation of the Reactive Asymmetry of Methyl Iodide. Crossed Beam Study of the Reaction of Rubidium with Oriented Methyl Iodide Molecules*, J. Am. Chem. Soc. **88**, 5331 (1966).
- [101] E. W. Kuipers, M. G. Tenner, A. Kleyn, and S. Stolte, *Observation of steric effects in gas-surface scattering*, Nature (London) **334**, 420 (1988).
- [102] T. P. Rakitzis, A. J. van den Brom, and M. H. M. Janssen, *Directional Dynamics in the Photodissociation of Oriented Molecules*, Science **303**, 1852 (2004).
- [103] H. L. Bethlem, G. Berden, and G. Meijer, *Decelerating Neutral Dipolar Molecules*, Phys. Rev. Lett. **83**, 1558 (1999).
- [104] R. Fulton, A. I. Bishop, and P. F. Barker, *Optical Stark Decelerator for Molecules*, Phys. Rev. Lett. **93**, 243004 (2004).
- [105] N. Vanhaecke, U. Meier, M. Andrist, B. H. Meier, and F. Merkt, *Multistage Zeeman deceleration of hydrogen atoms*, Phys. Rev. A **75**, 031402 (2007).
- [106] D. Auerbach, E. E. A. Bromberg, and L. Wharton, *Alternate-gradient focusing of molecular beams*, J. Chem. Phys. **45**, 2160 (1966).
- [107] H. L. Bethlem, M. R. Tarbutt, J. Küpper, D. Carty, K. Wohlfart, E. A. Hinds, and G. Meijer, *Alternating gradient focusing and deceleration of polar molecules*, J. Phys. B: At. Mol. Opt. Phys **39**, R263 (2006).
- [108] M. R. Tarbutt and E. A. Hinds, *Nonlinear dynamics in an alternating gradient guide for neutral particles*, New J. Phys. **10**, 073011 (2008).
- [109] K. Wohlfart, F. Grätz, F. Filsinger, H. Haak, G. Meijer, and J. Küpper, *Alternating-gradient focusing and deceleration of large molecules*, Phys. Rev. A **77**, 031404 (2008).
- [110] R. Moro, X. Xu, S. Yin, and W. A. de Heer, *Ferroelectricity in free niobium clusters*, Science **300**, 1265 (2003).

- [111] M. Broyer, R. Antoine, I. Compagnon, D. Rayane, and P. Dugourd, *From clusters to biomolecules: electric dipole, structure and dynamics*, Phys. Scr. **76**, C135 (2007).
- [112] K. Wohlfart, M. Schnell, J.-U. Grabow, and J. Küpper, *Precise dipole moment and quadrupole coupling constants of benzonitrile*, J. Mol. Spec. **247**, 119 (2008).
- [113] F. Filsinger, J. Küpper, G. Meijer, L. Holmegaard, J. H. Nielsen, I. Nevo, J. L. Hansen, and H. Stapelfeldt, *Quantum-state selection, alignment, and orientation of large molecules using static electric and laser fields*, J. Chem. Phys. **131**, 064309 (2009).
- [114] Y. R. Wu and D. H. Levy, *Determination of the geometry of deuterated tryptamine by rotationally resolved electronic spectroscopy*, J. Chem. Phys. **91**, 5278 (1989).
- [115] G. Berden, W. L. Meerts, and E. Jalviste, *High resolution electronic spectroscopy of 1-aminonaphthalene: S-0 and S-1 geometries and S-1 \leftarrow S-0 transition moment orientations*, J. Chem. Phys. **103**, 9596 (1995).
- [116] O. Dorosh, E. Bialkowska-Jaworska, Z. Kisiel, and L. Pszczólkowski, *New measurements and global analysis of rotational spectra of Cl-, Br-, and I-benzene: Spectroscopic constants and electric dipole moments*, J. Mol. Spec. **246**, 228 (2007).
- [117] K. Wohlfart, F. Filsinger, F. Grätz, J. Küpper, and G. Meijer, *Stark deceleration of OH radicals in low-field-seeking and high-field-seeking quantum states*, Phys. Rev. A **78**, 033421 (2008).
- [118] M. Kirste, B. G. Sartakov, M. Schnell, and G. Meijer, *Nonadiabatic transitions in electrostatically trapped ammonia molecules*, Phys. Rev. A **79**, 051401 (2009).
- [119] I. Nevo, L. Holmegaard, J. H. Nielsen, J. L. Hansen, H. Stapelfeldt, F. Filsinger, G. Meijer, and J. Küpper, *Laser-induced 3D alignment and orientation of quantum state-selected molecules*, Phys. Chem. Chem. Phys. **11**, 9912 (2009).
- [120] S. S. Viftrup, V. Kumarappan, S. Trippel, and H. Stapelfeldt, *Holding and Spinning Molecules in Space*, Phys. Rev. Lett. **99**, 143602 (2007).
- [121] P. Dietrich, D. T. Strickland, M. Laberge, and P. B. Corkum, *Molecular re-orientation during dissociative multiphoton ionization*, Phys. Rev. A **47**, 2305 (1993).
- [122] B. Friedrich, D. P. Pullman, and D. R. Herschbach, *Alignment and Orientation of Rotationally Cool Molecules*, J. Phys. Chem. **95**, 8118 (1991).

- [123] M. D. Poulsen, E. Péronne, H. Stapelfeldt, C. Z. Bisgaard, S. S. Viftrup, E. Hamilton, and T. Seideman, *Nonadiabatic alignment of asymmetric top molecules: Rotational revivals*, J. Chem. Phys. **121**, 783 (2004).
- [124] A. Rouzée, S. Guérin, V. Boudon, B. Lavorel, and O. Faucher, *Field-free one-dimensional alignment of ethylene molecule*, Phys. Rev. A **73**, 033418 (2006).
- [125] K. F. Lee, E. A. Shapiro, D. M. Villeneuve, and P. B. Corkum, *Coherent creation and annihilation of rotational wave packets in incoherent ensembles*, Phys. Rev. A **73**, 033403 (2006).
- [126] L. Holmegaard, S. S. Viftrup, V. Kumarappan, C. Z. Bisgaard, H. Stapelfeldt, E. Hamilton, and T. Seideman, *Control of rotational wave-packet dynamics in asymmetric top molecules*, Phys. Rev. A **75**, 051403(R) (2007).
- [127] P. W. Dooley, I. V. Litvinyuk, K. F. Lee, D. M. Rayner, M. Spanner, D. M. Villeneuve, and P. B. Corkum, *Direct imaging of rotational wave-packet dynamics of diatomic molecules*, Phys. Rev. A **68**, 023406 (2003).
- [128] C. Z. Bisgaard, M. D. Poulsen, E. Péronne, S. S. Viftrup, and H. Stapelfeldt, *Observation of Enhanced Field-Free Molecular Alignment by Two Laser Pulses*, Phys. Rev. Lett. **92**, 173004 (2004).
- [129] C. Z. Bisgaard, S. S. Viftrup, and H. Stapelfeldt, *Alignment enhancement of a symmetric top molecule by two short laser pulses*, Phys. Rev. A **73**, 053410 (2006).
- [130] O. Geßner, A. M. D. Lee, J. P. Shaffer, H. Reisler, S. V. Levchenko, A. I. Krylov, J. G. Underwood, H. Shi, A. L. L. East, D. M. Wardlaw, E. t. H. Chrysostom, C. C. Hayden, and A. Stolow, *Femtosecond Multidimensional Imaging of a Molecular Dissociation*, Science **311**, 219 (2006).
- [131] C. Bostedt, H. Thomas, M. Hoener, E. Eremina, T. Fennel, K.-H. Meiwes-Broer, H. Wabnitz, M. Kuhlmann, E. Plönjes, K. Tiedtke, R. Treusch, J. Feldhaus, A. R. B. de Castro, and T. Möller, *Multistep Ionization of Argon Clusters in Intense Femtosecond Extreme Ultraviolet Pulses*, Phys. Rev. Lett. **100**, 133401 (2008).
- [132] B. Noller, L. Poisson, R. Maksimenka, I. Fischer, and J.-M. Mestdagh, *Femtosecond Dynamics of Isolated Phenylcarbenes*, J. Am. Chem. Soc. **130**, 14908 (2008).
- [133] R. Santra, N. V. Kryzhevoi, and L. S. Cederbaum, *X-Ray Two-Photon Photoelectron Spectroscopy: A Theoretical Study of Inner-Shell Spectra of the Organic Para-Aminophenol Molecule*, Phys. Rev. Lett. **103**, 013002 (2009).

- [134] H. Akagi, T. Otohe, A. Staudte, A. Shiner, F. Turner, R. Dörner, D. M. Villeneuve, and P. B. Corkum, *Laser Tunnel Ionization from Multiple Orbitals in HCl*, *Science* **325**, 1364 (2009).
- [135] A. Staudte, S. Patchkovskii, D. Pavičić, H. Akagi, O. Smirnova, D. Zeidler, M. Meckel, D. M. Villeneuve, R. Dörner, M. Y. Ivanov, and P. B. Corkum, *Angular Tunneling Ionization Probability of Fixed-in-Space H_2 Molecules in Intense Laser Pulses*, *Phys. Rev. Lett.* **102**, 033004 (2009).
- [136] A. Landers, T. Weber, I. Ali, A. Cassimi, M. Hattass, O. Jagutzki, A. Nauert, T. Osipov, A. Staudte, M. H. Prior, H. Schmidt-Böcking, C. L. Cocke, and R. Dörner, *Photoelectron Diffraction Mapping: Molecules Illuminated from Within*, *Phys. Rev. Lett.* **87**, 013002 (2001).
- [137] A. V. Golovin, J. Adachi, S. Motoki, M. Takahashi, and A. Yagishita, *Inner-shell photoelectron angular distributions from fixed-in-space OCS molecules: comparison between experiment and theory*, *J. Phys. B: At. Mol. Opt. Phys.* **38**, 3755 (2005).
- [138] E. Shigemasa, J. Adachi, M. Oura, and A. Yagishita, *Angular Distributions of $1s\sigma$ Photoelectrons from Fixed-in-Space N_2 Molecules*, *Phys. Rev. Lett.* **74**, 359 (1995).
- [139] D. Rolles, G. Prümper, H. Fukuzawa, X.-J. Liu, Z. D. Pešić, R. F. Fink, A. N. Grum-Grzhimailo, I. Dumitriu, N. Berrah, and K. Ueda, *Molecular-Frame Angular Distributions of Resonant $CO : C(1s)$ Auger Electrons*, *Phys. Rev. Lett.* **101**, 263002 (2008).
- [140] B. Zimmermann, D. Rolles, B. Langer, R. Hentges, M. Braune, S. Cvejanovic, O. Geßner, F. Heiser, S. Korica, T. Lischke, A. Reinköster, J. Viehhaus, R. Dörner, V. McKoy, and U. Becker, *Localization and loss of coherence in molecular double-slit experiments*, *Nature Phys.* **4**, 649 (2008).
- [141] M. Yamazaki, J. ichi Adachi, T. Teramoto, A. Yagishita, M. Stener, and P. Decleva, *3D mapping of photoemission from a single oriented H_2O molecule*, *J. Phys. B: At. Mol. Opt. Phys.* **42**, 051001 (2009).
- [142] P. B. Corkum, *Plasma perspective on Strong Field Multiphoton Ionization*, *Phys. Rev. Lett.* **71**, 1994 (1993).
- [143] M. Lein, *Molecular imaging using recolliding electrons*, *J. Phys. B* **40**, R135 (2007).
- [144] S. Baker, J. S. Robinson, C. A. Haworth, H. Teng, R. A. Smith, C. C. Chirila, M. Lein, J. W. G. Tisch, and J. P. Marangos, *Probing Proton Dynamics in Molecules on an Attosecond Time Scale*, *Science* **312**, 424 (2006).

- [145] A. Stolow, A. E. Bragg, and D. M. Neumark, *Femtosecond Time-Resolved Photoelectron Spectroscopy*, Chem. Rev. **104**, 1719 (2004).
- [146] V. Blanchet, M. Z. Zgierski, T. Seideman, and A. Stolow, *Discerning vibronic molecular dynamics using time-resolved photoelectron spectroscopy*, Nature (London) **401**, 52 (1999).
- [147] K. L. Reid, *Photoelectron Angular Distributions*, Annu. Rev. Phys. Chem. **54**, 397 (2003).
- [148] D. Dill, *Fixed-molecule photoelectron angular distributions*, J. Chem. Phys. **65**, 1130 (1976).
- [149] M. Tsubouchi, B. J. Whitaker, L. Wang, H. Kohguchi, and T. Suzuki, *Photoelectron Imaging on Time-Dependent Molecular Alignment Created by a Femtosecond Laser Pulse*, Phys. Rev. Lett. **86**, 4500 (2001).
- [150] K. L. Reid and J. G. Underwood, *Extracting molecular axis alignment from photoelectron angular distributions*, J. Chem. Phys. **112**, 3643 (2000).
- [151] J. G. Underwood and K. L. Reid, *Time-resolved photoelectron angular distributions as a probe of intramolecular dynamics: Connecting the molecular frame and the laboratory frame*, J. Chem. Phys. **113**, 1067 (2000).
- [152] Y. Suzuki and T. Seideman, *Mapping rotational coherences onto time-resolved photoelectron imaging observables*, J. Chem. Phys. **122**, 234302 (2005).
- [153] J. L. Krause, K. J. Schafer, and K. C. Kulander, *High-order harmonic generation from atoms and ions in the high intensity regime*, Phys. Rev. Lett. **68**, 3535 (1992).
- [154] L. V. Keldysh, *Ionization in the field of a strong electromagnetic wave*, Sov. Phys. JETP **20**, 1307 (1965).
- [155] G. L. Yudin and M. Y. Ivanov, *Physics of correlated double ionization of atoms in intense laser fields: Quasistatic tunneling limit*, Phys. Rev. A **63**, 033404 (2001).
- [156] P. Eckle, A. N. Pfeiffer, C. Cirelli, A. Staudte, R. Dorner, H. G. Muller, M. Büttiker, and U. Keller, *Attosecond Ionization and Tunneling Delay Time Measurements in Helium*, Science **322**, 1525 (2008).
- [157] M. Büttiker and R. Landauer, *Traversal Time for Tunneling*, Phys. Rev. Lett. **49**, 1739 (1982).

- [158] P. B. Corkum, N. H. Burnett, and F. Brunel, *Above-Threshold Ionization in the Long-Wavelength Limit*, Phys. Rev. Lett. **62**, 1259 (1989).
- [159] P. Agostini, F. Fabre, G. Mainfray, G. Petite, and N. K. Rahman, *Free-Free Transitions Following Six-Photon Ionization of Xenon Atoms*, Phys. Rev. Lett. **42**, 1127 (1979).
- [160] P. H. Bucksbaum, R. R. Freeman, M. Bashkensky, and T. McIlrath, *Role of the ponderomotive potential in above-threshold ionization*, J. Opt. Soc. Am. B **4**, 760 (1987).
- [161] D. Pavicic, K. F. Lee, D. M. Rayner, P. B. Corkum, and D. M. Villeneuve, *Direct Measurement of the Angular Dependence of Ionization for N_2 , O_2 and CO_2 in Intense Laser Fields*, Phys. Rev. Lett. **98**, 243001 (2007).
- [162] J. Delwiche, M. J. Hubin-Franskin, G. Caprace, P. Natalis, and D. Roy, *On the He(I) and Ne(I) photoelectron spectra of OCS*, J. Elec. Spec. Rel. Phenom. **21**, 205 (1980).
- [163] M. V. Ammosov, N. B. Delone, and V. P. Krainov, *Tunnel ionization of complex atoms and of atomic ions in an alternating electromagnetic field*, Sov. Phys. JETP **64**, 1191 (1986).
- [164] A. M. Perelomov, V. S. Popov, and M. V. Terent'ev, *Ionization of atoms in an alternating electric field*, Sov. Phys. JETP **23**, 924 (1966).
- [165] X. M. Tong and C. D. Lin, *Empirical formula for static field ionization rates of atoms and molecules by lasers in the barrier-suppression regime*, J. Phys. B: At. Mol. Opt. Phys. **38**, 2593 (2005).
- [166] P. Wang, A. M. Sayler, K. D. Carnes, B. D. Esry, and I. Ben-Itzhak, *Disentangling the volume effect through intensity-difference spectra: application to laser-induced dissociation of H_2^+* , Opt. Lett. **30**, 664 (2005).
- [167] F. Lindner, M. G. Schätzel, H. Walther, A. Baltuška, E. Goulielmakis, F. Krausz, D. B. Milošević, D. Bauer, W. Becker, and G. G. Paulus, *Attosecond Double-Slit Experiment*, Phys. Rev. Lett. **95**, 040401 (2005).
- [168] D. B. Milošević, G. G. Paulus, D. Bauer, and W. Becker, *Above-threshold ionization by few-cycle pulses*, J. Phys. B: At. Mol. Opt. Phys. **39**, R203 (2006).
- [169] M. F. Kling, J. Rauschenberger, A. J. Verhoef, E. Hasović, T. Uphues, D. B. Milošević, H. G. Muller, and M. J. J. Vrakking, *Imaging of carrier-envelope phase effects in above-threshold ionization with intense few-cycle laser fields*, New J. Phys. **10**, 025024 (2008).

- [170] T. K. Kjeldsen, C. Z. Bisgaard, L. B. Madsen, and H. Stapelfeldt, *Role of symmetry in strong-field ionization of molecules*, Phys. Rev. A **68**, 063407 (2003).
- [171] T. K. Kjeldsen, C. Z. Bisgaard, L. B. Madsen, and H. Stapelfeldt, *Influence of molecular symmetry on strong-field ionization: Studies on ethylene, benzene, fluorobenzene, and chlorofluorobenzene*, Phys. Rev. A **71**, 013418 (2005).
- [172] B. H. Brandsen and C. J. Joachain, *Physics of Atoms and Molecules* (Prentice Hall 2003), 2 edition.
- [173] P. Atkins and R. Friedman, *Molecular Quantum Mechanics* (Oxford University Press 2005), 4 edition.
- [174] J. Fernández and L. B. Madsen, *Above-threshold ionization, energy-resolved photoelectron angular distributions, and momentum distributions of H_2^+ in intense femtosecond laser pulses*, Phys. Rev. A **79**, 063406 (2009).
- [175] T. K. Kjeldsen, L. B. Madsen, and J. P. Hansen, *Ab initio studies of strong-field ionization of arbitrarily oriented H_2^+ molecules*, Phys. Rev. A **74**, 035402 (2006).
- [176] L. A. A. Nikolopoulos, T. K. Kjeldsen, and L. B. Madsen, *Three-dimensional time-dependent Hartree-Fock approach for arbitrarily oriented molecular hydrogen in strong electromagnetic fields*, Phys. Rev. A **76**, 033402 (2007).
- [177] X. M. Tong, Z. X. Zhao, and C. D. Lin, *Theory of molecular tunneling ionization*, Phys. Rev. A **66**, 33402 (2002).
- [178] T. K. Kjeldsen and L. B. Madsen, *Strong-field ionization of N_2 : length and velocity gauge strong-field approximation and tunneling theory*, J. Phys. B **37**, 2033 (2004).
- [179] I. V. Litvinyuk, K. F. Lee, P. W. Dooley, D. M. Rayner, D. M. Villeneuve, and P. B. Corkum, *Alignment-Dependent Strong Field Ionization of Molecules*, Phys. Rev. Lett. **90**, 233003 (2003).
- [180] A. S. Alnaser, S. Voss, X.-M. Tong, C. M. Maharjan, P. Ranitovic, B. Ulrich, T. Osipov, B. Shan, Z. Chang, and C. L. Cocke, *Effects of molecular structure on ion disintegration patterns in ionization of O_2 and N_2 by short laser pulses*, Phys. Rev. Lett. **93**, 113003 (2004).
- [181] A. S. Alnaser, C. M. Maharjan, X. M. Tong, B. Ulrich, P. Ranitovic, B. Shan, Z. Chang, C. D. Lin, C. L. Cocke, and I. V. Litvinyuk, *Effects of orbital symmetries in dissociative ionization of molecules by few-cycle laser pulses*, Phys. Rev. A **71**, 031403(R) (2005).

- [182] M. Abu-samha and L. B. Madsen, *Theory of strong-field ionization of aligned CO₂*, Phys. Rev. A **80**, 023401 (2009).
- [183] R. D. Suenram and F. J. Lovas, *Millimeter wave spectrum of glycine - a new conformer*, J. Am. Chem. Soc. **102**, 7180 (1980).
- [184] T. R. Rizzo, Y. D. Park, L. Peteanu, and D. H. Levy, *Electronic-spectrum of the amino-acid tryptophan cooled in a supersonic molecular-beam*, J. Chem. Phys. **83**, 4819 (1985).
- [185] F. Filsinger, J. Küpper, G. Meijer, J. Hansen, J. Maurer, J. Nielsen, L. Holmegaard, and H. Stapelfeldt, *Pure Samples of Individual Conformers: The Separation of Stereoisomers of Complex Molecules Using Electric Fields*, Angew Chem. Int. Ed. **48**, 6900 (2009).
- [186] C. Ng, *Vacuum ultraviolet spectroscopy and chemistry by photoionization and photoelectron methods*, Annu. Rev. Phys. Chem. **53**, 101 (2002).
- [187] W. Li, X. Zhou, R. Lock, S. Patchkovskii, A. Stolow, H. C. Kapteyn, and M. M. Murnane, *Time-Resolved Dynamics in N₂O₄ Probed Using High Harmonic Generation*, Science **322**, 1207 (2008).
- [188] S. Guérin, A. Rouzée, and E. Hertz, *Ultimate field-free molecular alignment by combined adiabatic-impulsive field design*, Phys. Rev. A **77**, 041404 (2008).
- [189] A. I. Kuleff and L. S. Cederbaum, *Charge migration in different conformers of glycine: The role of nuclear geometry*, Chemical Physics **338**, 320 (2007), molecular Wave Packet Dynamics - (in honour of Jörn Manz).
- [190] F. Krasniqi, B. Najjari, L. Strüder, D. Rolles, A. Voitkiv, and J. Ullrich, *Imaging Molecules from Within: Ultra-fast, Ångström Scale Structure Determination of Molecules via Photoelectron Holography using Free Electron Lasers*, <http://arxiv.org/abs/0910.3078> (2009).
- [191] H. Niikura, F. Légaré, R. Hasbani, M. Y. Ivanov, D. M. Villeneuve, and P. B. Corkum, *Probing molecular dynamics with attosecond resolution using correlated wave packet pairs*, Nature (London) **421**, 826 (2003).
- [192] B. J. Sussman, D. Townsend, M. Y. Ivanov, and A. Stolow, *Dynamic Stark Control of Photochemical Processes*, Science **314**, 278 (2006).
- [193] C. B. Madsen, L. B. Madsen, S. S. Viftrup, M. P. Johansson, T. B. Poulsen, L. Holmegaard, V. Kumarappan, K. A. Jørgensen, and H. Stapelfeldt, *Manipulating the Torsion of Molecules by Strong Laser Pulses*, Phys. Rev. Lett. **102**, 073007 (2009).

-
- [194] C. B. Madsen, L. B. Madsen, S. S. Viftrup, M. P. Johansson, T. B. Poulsen, L. Holmegaard, V. Kumarappan, K. A. J. rgensen, and H. Stapelfeldt, *A combined experimental and theoretical study on realizing and using laser controlled torsion of molecules*, J. Chem. Phys. **130**, 234310 (2009).